



**I
N
A
O
E**

**DYNAMIC HOLOGRAPHY RECORDING IN RUBIDIUM
VAPOR**

By

Olena Benavides

M.Sc., INAOE

A thesis submitted to the
Program in Optics Science, Optics Science Department in partial
fulfillment
of the requirements for the degree of
Doctor in Optic Science

At the

National Institute of Astrophysics, Optics and Electronics

September 2009, Tonantzintla, Puebla

Advisor:

Dr. Nikolai Korneev Zabello

Optics Department

INAOE

©INAOE, 2009

All rights reserved

The author hereby grants to INAOE permission to reproduce and
to distribute copies of this thesis
document in whole or in part



*For my beloved husband Lazaro and children
David, Katia and Ruslan*

Acknowledgements

I would like to give special thanks to my advisor Doctor Nikolai Korneev, for his guidance, encouragement and support. He spent a significant amount of time supervising this work and always had time for my questions.

I want to thank the faculty members of the Institute of Astronomy, Optics and Electronics who were my teachers during these three years of graduate studies.

I want to thank my family, especially for my mother and husband. Their love and support has always given me the energy to work.

I am so grateful to Ariel and Anna for their help and friendship.

Finally I want to thank all teachers and administration who help me, especially thanks for Ing. Jose Luis Orta Acuña, Dr. Victor Golikov and M. Sc. Olga Lebedeva.

THE GENEROUS FINANCIAL HELP OF THE PROMEP AND THE UNIVERSIDAD AUTONOMA DEL CARMEN IS GRATEFULLY ACKNOWLEDGED

ABSTRACT

We investigate the nonlinear refraction and absorption related to holographic writing in rubidium vapor at resonance with ^{87}Rb D2 transition. The numerical model based on time-dependent density matrix formalism is used. The theory adequately describes nonlinear optical rotation and absorption at light intensities in $0.1 - 30\text{mW/cm}^2$ range.

We discuss two principal mechanisms. The first is based on absorption grating writing and another grating formation mechanism based on Faraday rotation. It is promising for applications because it gives phase holograms with higher diffraction efficiency. The theory for both cases was developed.

The basic configurations for obtaining amplitude and phase gratings for nearly equal frequencies of writing beams are investigated experimentally, and the writing time is estimated.

We also proposed a rapid solution algorithm for the calculation of the full density matrix evolution for a multi-level atom. The calculation principle is similar to the split-step algorithm widely used for modeling the nonlinear propagation in media with Kerr-type nonlinearity. The spectrum of nonlinear Faraday rotation in the D2 natural rubidium line is calculated and compared with the experiment. Good agreement is obtained

RESUMEN

Investigamos la refracción y la absorción no lineales relacionadas con el tiempo de grabado de holograma en el vapor de rubidio en la resonancia con la transición de ^{87}Rb D2. Utilizamos el modelo numérico basado en el formalismo de la matriz de densidad dependiente del tiempo. La teoría describe adecuadamente la rotación no lineal y la absorción de la luz en el rango de intensidades de $0.1 - 30 \text{ mW} / \text{cm}^2$.

En este trabajo también discutimos los dos principales mecanismos de grabado de hologramas. El primero está basado en la escritura de rejilla de absorción y el otro en el mecanismo de formación de rejilla basado en la rotación del Faraday. Este mecanismo es útil para aplicaciones porque se obtienen hologramas de fase de alta eficiencia. Desarrollamos la teoría para ambos casos.

Investigamos experimentalmente las configuraciones básicas para la obtención de rejillas de amplitud y de fase para frecuencias iguales a las haces de grabado y estimamos el tiempo de grabado.

También proponemos un algoritmo de solución rápido para el cálculo de la evolución completa de la matriz de la densidad para un átomo de niveles múltiples. El principio de cálculo es similar al algoritmo de división por paso (ver el capítulo 5) extensamente usado para modelar la propagación no lineal en medios con la no linealidad de Kerr.

Calculamos el espectro no lineal de la rotación de Faraday en la línea D2 del rubidio y comparamos con el experimento. Obtenemos el buen acuerdo de la teoría con el experimento.

Introduction

Rubidium vapor close to resonance is an important optical material. Because of relatively simple atomic structure (one valence electron), and transitions in near infrared, which correspond to tunable diode laser wavelengths, there is a lot of experimental and theoretical activity in the area. Recent studies with rubidium include laser cooling, slow light, nonlinear spectroscopy [1, 2] among others. Though the amount of literature on rubidium is very big, the nonlinear propagation of light in this material was not a topic of much activity. After the initial work in 70-80's, the research in this area was quite fragmentary [3-5], and the theoretical description is practically limited to the simplest two-level model, which is not valid at resonance. On the other hand, estimations and existing experimental work [6-9] suggest, that it is exactly close to resonance, where one can expect the strongest nonlinear properties.

In this thesis we systematically study both from theoretical and experimental viewpoint of nonlinear optical properties of the rubidium inside the absorption line. The study is complicated, because the hyperfine structure of rubidium includes 24 or 36 levels for different isotopes, and magnetic fields, light polarization state and light intensity strongly affect the nonlinear behavior. The complete experimental study without the developed theory is not practical because of a big volume of necessary data. In the thesis, we develop theoretical approaches which permit direct calculations of nonlinear behavior of rubidium vapor from the first principles. For this, the new approaches and necessary software were developed, and comparison with experiment was made for controlled conditions.

The density matrix formalism is an established theoretical tool for study of the phenomena of light interaction with multilevel atom. Nevertheless, the direct calculations with time-dependent multi-level density matrix are prohibitively long for rubidium. We developed an algorithm, similar to the split-step propagation method, which permits to perform the necessary calculations in acceptable time

[10]. The efficiency of this algorithm was confirmed by comparison with the experiment on nonlinear Faraday rotation.

The ultimate goal of our study is to find the conditions of efficient hologram recording and strong beam self-action. The dynamic holography in rubidium has unique properties of sensitivity – the energy necessary for hologram writing in this material is close to that one for traditional photographic materials and it is four orders of magnitude better, than in most sensitive photorefractive materials. We have identified experimentally some simple ways of recording amplitude and phase holograms, and estimated for them recording time and diffraction efficiency. It was shown, that the amplitude hologram formation is well explained by the developed theory. Though the optimal conditions were not completely identified, we have found, that highly efficient holograms can be written in rubidium by low-power semiconductor lasers with writing time in 100ns range, or faster. These writing times are well adapted to the non-contact adaptive detection of ultrasound, which is a promising application of dynamic holography.

The new results of the thesis are:

- development of split-step type algorithm for calculation of density matrix evolution, and experimental confirmation of its effectiveness for predicting the nonlinear behavior of Faraday rotation in rubidium vapor close to resonance
- calculations of nonlinear absorption and refraction for some typical geometries of hologram writing, and their comparison with the experiment.
- clarifying the writing mechanisms for absorption gratings
- experimental determination of diffraction efficiencies and writing times for amplitude and phase gratings in some particular cases

In particular, it was shown that:

- the proposed split-step solution algorithm permits to calculate with good accuracy the observed nonlinear spectra

- the holographic writing in rubidium is fast and efficient, and can be successfully used for adaptive optical detection of ultrasound.

The results were published in 2 peer-reviewed international journals and presented at national and international conferences [[10-13](#)]

Contents

Abstract

Acknowledgements

Introduction

| | |
|---|----|
| 1 The rubidium vapor spectroscopy..... | 1 |
| 1.1 Rubidium properties..... | 1 |
| 1.2 Light interactions with two-level atom..... | 2 |
| 1.3 Basic laser absorption spectroscopy | 5 |
| 1.3.1 Laser absorption..... | 6 |
| 1.3.2 Doppler shifts | 7 |
| 1.3.3 Populations..... | 9 |
| 1.3.4 Laser absorption through a cell..... | 9 |
| 1.4 Multilevel effects..... | 11 |
| 1.5 Energy levels in rubidium..... | 13 |
| 1.5.1 Fine structure levels..... | 14 |
| 1.5.2 Hyperfine levels..... | 16 |
| 1.5.3 Transitions..... | 20 |
| 1.6 Zeeman Effect..... | 20 |

| | |
|--|----|
| 2 Nonlinear properties of Rb..... | 22 |
| 2.1 Introduction..... | 22 |
| 2.2. Material-Based Classification of Nonlinear Optical Effects..... | 22 |
| 2.3 Absorption, Induced, and Spontaneous Emission..... | 23 |
| 2.4 Self-interaction of the light with atoms..... | 24 |
| 2.5 Nonlinear Faraday rotation..... | 25 |
| 2.6 Mechanisms of the linear magneto-optical effects..... | 26 |
| 2.7 Self rotation..... | 29 |
| 2.8 Self-phase modulation..... | 30 |
| 2.9 Resonant Absorption and Refractive Index in Rubidium..... | 31 |
| | |
| 3. Photorefractive Effect..... | 34 |
| 3.1 Introduction..... | 34 |
| 3.2 Photorefractive materials and their properties..... | 34 |
| 3.3 Photorefractive Effect..... | 34 |
| 3.3.1 Kukhtarev-Vinetskii's model..... | 35 |
| 3.4 Two-Wave Mixing..... | 37 |
| 3.4.1 Theory of Two-Wave Mixing..... | 37 |
| 3.4.2 Speed of photorefractive effect..... | 40 |
| 3.4.3 Diffraction efficiency..... | 41 |
| 3.5 FWM..... | 42 |

| | |
|---|----|
| 4 Principles of holography..... | 44 |
| 4.1 Recording of Holograms and Wavefront Reconstruction..... | 44 |
| 4.2 Classification Scheme..... | 46 |
| 4.3 Dynamic holography..... | 47 |
| 4.4 Amplitude and Phase Holograms..... | 48 |
| 5 Density Matrix Formalism..... | 51 |
| 5.1. Density Matrix Calculations for two-level system..... | 51 |
| 5.2. “Split-step” method..... | 54 |
| 5.2.1. Split-step Fourier method (SSFM)..... | 55 |
| 5.3 Density Matrix Calculation of Nonlinear Response Functions..... | 58 |
| 6 Mechanisms of holography recording in rubidium vapor close to resonance..... | 60 |
| 6.1 Introduction..... | 60 |
| 6.2 Experiments set-up..... | 60 |
| 6.2.1 Tunable semiconductor laser..... | 60 |
| 6.2.2 General Theory..... | 62 |
| 6.2.3 Acusto-optical modulator..... | 64 |
| 6.2.4 Lock-in..... | 65 |

| | |
|--|-----|
| 6.3 Scheme of the Experiment 1..... | 66 |
| 6.4 Scheme of the Experiment 2..... | 68 |
| 6.5 The computer model for ^{87}Rb , description..... | 69 |
| 6.6 The computer model, comparison of the experimental results with theory for ^{87}Rb | 75 |
| 6.7 Direct multi-level density matrix calculation of nonlinear optical rotation spectra for up to 36 levels, in ^{85}Rb | 81 |
| 6.8 Experiment, absorption and rotation measurements | 86 |
| 6.9 Experiment, hologram writing | 90 |
| 6.10 Experiment 2. Result..... | 96 |
| 6.11 Discussion and Conclusion..... | 97 |
| List of Table..... | 100 |
| List of Figures..... | 101 |
| Reference..... | 107 |
| Resumen en Extenso | |

Chapter 1 The Rubidium Vapor Spectroscopy

Introduction

The goal of this part of thesis is to describe the most relevant for our area of research, properties of alkali metals, particularly rubidium.

In this chapter we give only general treatment, for mathematical solution of the resonance interaction of light with two-level atom see Chapter 2

1.1 Rubidium properties

Rubidium was discovered in 1861 by German chemists Robert Bunsen (1811-99) and Gustav Kirchhoff (1824-87). Rubidium is one of four elements discovered by spectroscopy. Rubidium is a soft, silvery metal. It is one of the most active chemical elements. Rubidium is a member of the alkali family. It has a melting point of 39°C and a boiling point of 688°C . Its density is 1.532 grams per cubic centimeter.

Natural rubidium is a mixture of two isotopes ^{87}Rb and ^{85}Rb

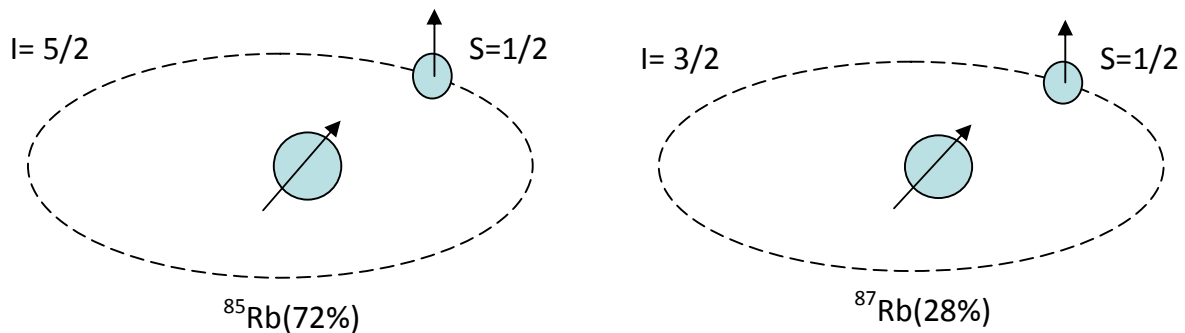


Figure 1.1 There are two commonly-occurring isotopes of Rubidium found in nature, ^{85}Rb and ^{87}Rb . Both have only one valence electron and can be approximated as one-electron atoms. The major difference between the isotopes is in the nuclear spin I .

Table 1.1 Atomic data for ^{87}Rb and ^{85}Rb [14]

| Property | Symbol | Value ^{87}Rb | Value ^{85}Rb |
|-------------------------------------|------------------------|------------------------|------------------------|
| Atomic mass | m | 86.909 u | 84.991 u |
| Nuclear spin | I | $3/2$ | $5/2$ |
| Wavelength of the D2 line in vacuum | λ | 780.241 nm | 780.241 nm |
| Wavelength of the D2 line in air | λ_{air} | 780.032 nm | 780.032 nm |
| Natural line width | Γ | $2\pi \cdot 6.065$ MHz | $2\pi \cdot 6.065$ MHz |
| Saturation intensity | I_0 | 1.6 mW/cm ² | 1.6 mW/cm ² |
| Landé factor, ground state D2 | g_a | $1/2$ | $1/3$ |
| Landé factor, excited state D2 | g_b | $2/3$ | $1/2$ |

1.2 Light interactions with two-level atom

We begin with the interactions between a laser field and a sample of stationary atoms having only two possible energy levels.

The difference $\Delta E = E_1 - E_0$ between the excited state energy E_1 and the ground state energy E_0 is used with Planck's law to determine the photon frequency ν associated with transitions between the two states:

$$\Delta E = h\nu_0 \quad (1.1)$$

There are three transition processes involving atoms and laser fields:

Stimulated absorption in which the atom starts in the ground state, absorbs a photon from the laser field, and then ends up in the excited state.

Stimulated emission in which the atom starts in the excited state, emits a photon with the same direction, frequency, and polarization as those in the laser field, and then ends up in the ground state.

Spontaneous emission in which the atom starts in the excited state, emits a photon in an arbitrary direction unrelated to the laser photons, and then ends up in the ground state.

Stimulated emission and absorption are associated with external electromagnetic fields such as from a laser or thermal (blackbody) radiation. We consider spontaneous emission first - a process characterized by a transition rate or probability per unit time for an atom in the excited state to decay to the ground state. This transition rate will be denoted γ and is about $3.8 \times 10^7/\text{s}$ (or 38 MHz) for the rubidium levels.

In the absence of an external field, any initial population of excited state atoms would decay exponentially to the ground state with a mean lifetime $\Delta t = 1/\gamma \approx 26\text{ns}$. In the rest frame of the atom, spontaneous photons are emitted in all directions with an energy spectrum having a mean $E = h\nu_0$ and a full width at half maximum (FWHM) ΔE given by the Heisenberg uncertainty principle $\Delta E\Delta t = \hbar$ or $\Delta E = \hbar/\Delta t$.

Expressed in frequency units, the FWHM is called the natural linewidth and given the symbol Γ . Thus

$$\Gamma = \frac{\gamma}{2\pi} \quad (1.2)$$

For our rubidium levels, $\Delta E \approx 2.5 \times 10^{-8} \text{ eV}$ or $\Gamma \approx 6 \text{ MHz}$.¹

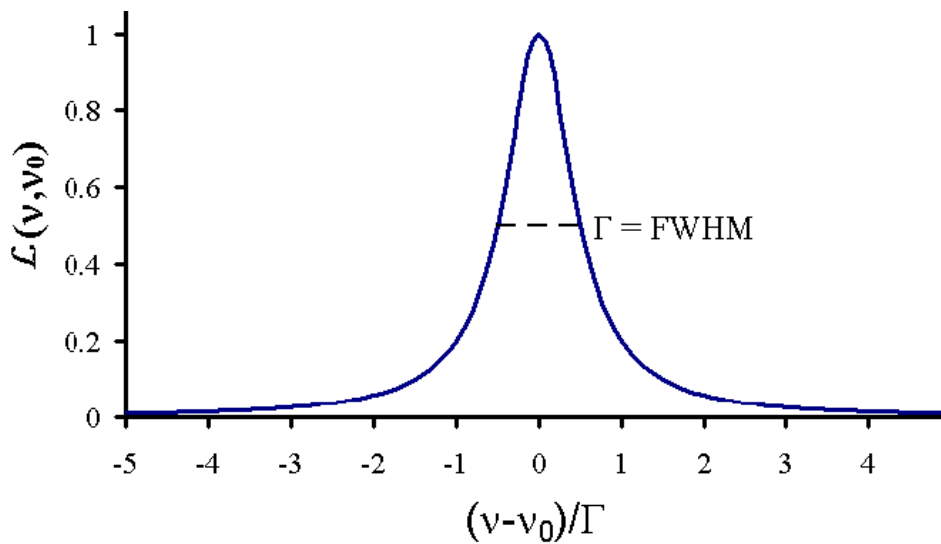


Figure 1.2 The Lorentzian line shape profile for resonance absorption

¹The natural linewidth Γ normally represents the sharpest observable energy distributions, but most attempts to measure it in gases are confounded by Doppler shifts associated with the random thermal motion of the atoms, which broaden the emission or absorption spectrum by an order of magnitude or more. Saturated absorption spectroscopy specifically overcomes the Doppler-broadening limit by providing for a two-photon interaction which only occurs for atoms with a lab frame velocity very near zero.

The stimulated emission and absorption processes are also described by a transition rate - a single rate giving the probability per unit time for a ground state atom to absorb a laser photon or for an excited state atom to emit a laser photon. The stimulated transition rate is proportional to the laser intensity I (SI units W/m^2) and is only significantly different from zero when the laser frequency ν is near the resonance frequency ν_0 .

This transition rate will be denoted αI , where

$$\alpha = \alpha_0 L(\nu, \nu_0) \quad (1.3)$$

and

$$L(\nu, \nu_0) = \frac{1}{1 + 4(\nu - \nu_0)^2 / \Gamma^2} \quad (1.4)$$

gives the Lorentzian (or natural resonance) frequency dependence as shown in Fig.1.2

$L(\nu, \nu_0)$ describes the spectrum of radiation from spontaneous emission and the width Γ is the same for both cases. The maximum transition rate αI occurs right on resonance ($\nu = \nu_0$) and for the rubidium transitions used

here $\alpha_0 \approx 20 \text{ MHz} / (mW / cm^2)$.

The value of γ / α_0 defines a parameter of the of the atoms called the saturation intensity I_{sat}

$$I_{sat} = \frac{\gamma}{\alpha_0} \quad (1.5)$$

and is about $1.6mW/cm^2$ for our rubidium transitions.²

Its significance is that when the laser intensity is equal to the saturation intensity, excited state atoms are equally likely to decay by stimulated emission or by spontaneous emission.

1.3 Basic laser absorption spectroscopy

The basic arrangement for ordinary laser absorption (not saturated absorption) spectroscopy through a gaseous sample is shown in Fig. 1.3. A laser beam passes through the vapor cell and its intensity is measured by a photodiode detector as the laser frequency ν is scanned through the natural resonance frequency.

When a laser beam propagates through a gaseous sample, the two stimulated transition processes change the intensity of the laser beam and affect the density of atoms (number per unit volume) in the ground and excited states.

² γ , Γ , α_0 , I_{sat} vary somewhat among the various rubidium D2 transitions. The values given are only representative

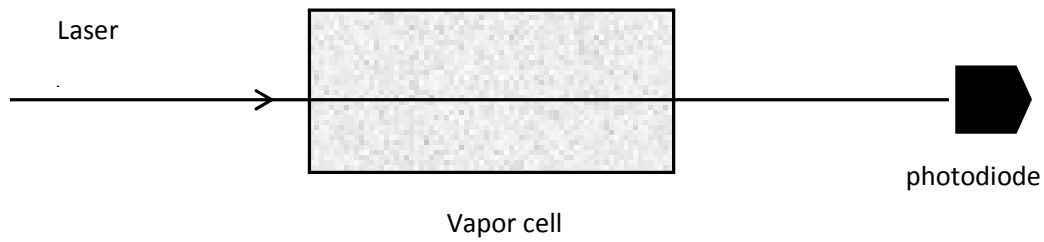


Figure 1.3 Basic arrangements for ordinary laser absorption spectroscopy.

Moreover, Doppler shifts associated with the random thermal motion of the absorbing atoms must also be taken into account. We begin with the basic equation describing how the laser intensity changes as it propagates through the sample and then continue with the effects of Doppler shifts and population changes.

1.3.1 Laser absorption

Because of stimulated emission and absorption, the laser intensity $I(x)$ varies as it propagates from x to $x + dx$ in the medium. So

$$\frac{dI}{dx} = -\kappa I \quad (1.6)$$

where the absorption coefficient (fractional absorption per unit length)

$$\kappa = h\nu_0\alpha(P_0 - P_1) \quad (1.7)$$

n_0 representing the overall density of atoms (number per unit volume) in the vapor cell, P_0 and P_1 represent the probabilities that the atoms are in the ground and excited states, respectively, or the fraction of atoms in each state.

1.3.2 Doppler shifts

Atoms in a vapor cell move randomly in all directions with each component of velocity having a distribution of values. Only the component of velocity parallel to the laser beam direction will be important when taking into account Doppler shifts and it is this component we refer to with the symbol v . The density of atoms dn in the velocity group between v and $v + dv$ is given by the Boltzmann velocity distribution:

$$dn = n_0 \sqrt{\frac{m}{2\pi kT}} e^{-mv^2/2kT} dv \quad (1.8)$$

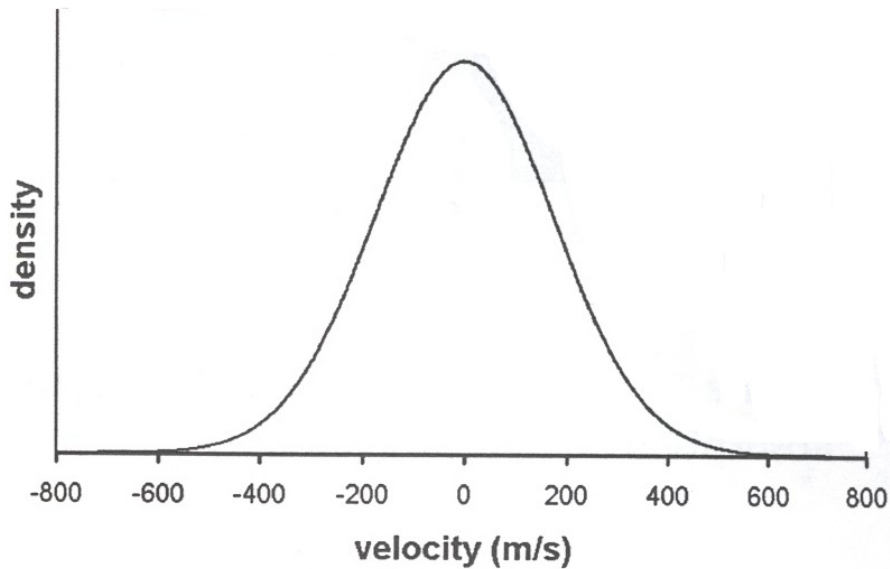


Figure 1.4 Maxwell-Boltzmann velocity distributions. The density of atoms vs. their velocity component in one direction for room temperature rubidium atoms.

With a standard deviation (proportional to the width of the distribution) given by:

$$\sigma_v = \sqrt{kT/m} \quad (1.9)$$

this is just a standard Gaussian distribution

$$dn = n_0 \frac{1}{\sqrt{2\pi}\sigma_v} e^{-v^2/2\sigma_v^2} dv \quad (1.10)$$

with a mean of zero -indicating the atoms are equally likely to be going in either direction .

It is properly normalized so that the integral over all velocities ($-\infty \rightarrow \infty$) is n_0 , the over-all atom density. Note that the distribution's variance σ_v^2 increases linearly with temperature and decreases inversely with atomic mass.

Atoms moving with a velocity v see the laser beam Doppler shifted by the amount v (v/c). Alternate view that atoms moving with a velocity v have a Doppler shifted resonance frequency

$$v'_0 = v_0 \left(1 + \frac{v}{c} \right) \quad (1.11)$$

The sign has been chosen to be correct for a laser beam propagating in the positive direction so that the resonance frequency is blue shifted to higher frequencies if v is positive and red shifted if v is negative.

The absorption coefficient $d\kappa$ from a velocity group dn at a laser frequency ν is then obtained from Eq. 1.7 by substituting dn for n_0 keeping in mind its dependence on v through Eq. 1.8 and by adjusting the Lorentzian dependence of α so that it is centered on the Doppler shifted resonance frequency ν'_0 (keeping in mind its dependence on v through Eq. 1.11).

$$d\kappa = hv\alpha_0(P_0 - P_1) L(v, v_0) dn \quad (1.12)$$

The absorption coefficient from all atoms is then found by integrating over all velocity groups. Setting $P_0 - P_1 = 1$ so that

$$d\kappa = n_0 hv\alpha_0 \sqrt{\frac{m}{2\pi kT}} L(v, v_0) e^{-mv^2/2kT} dv \quad (1.13)$$

1.3.3 Populations

Now we would like to take into account the changes to the ground and excited state populations arising from a laser beam propagating through the cell. The rate equations for the ground and excited state probabilities or fractions become:

$$\begin{aligned} \frac{dP_0}{dt} &= \gamma P_1 - \alpha I (P_0 - P_1) \\ \frac{dP_1}{dt} &= -\gamma P_1 + \alpha I (P_0 - P_1) \end{aligned} \quad (1.14)$$

where the first term on the right in each equation arises from spontaneous emission and the second term arises from stimulated absorption and emission.

1.3.4 Laser absorption through a cell

In the weak-field case κ at any frequency is given by

$$\kappa = \kappa_0 e^{-(v-v_0)^2/2\sigma_v^2} \quad (1.15)$$

with the width parameter given by

$$\sigma_v = v_0 \sqrt{\frac{kT}{mc^2}} \quad (1.16)$$

and

$$\kappa_0 = n_0 h \nu \alpha_0 \sqrt{\frac{m}{2\pi k T} \frac{c}{\nu_0} \frac{\pi \Gamma}{2}} \quad (1.17)$$

And it is independent of the laser intensity. In this case, Eq.1.6 is satisfied by Beer's law which says that the intensity decays exponentially with distance traveled through the sample.

$$I(x) = I_0 e^{-\kappa x} \quad (1.18)$$

In the general case, κ is given by

$$\kappa = \kappa_0' e^{-(\nu - \nu_0)^2 / 2\sigma_\nu^2} \quad (1.19)$$

Where the width parameter, σ_ν is the same as before Eq.1.16, but compared to the weak-field absorption coefficient Eq. 1.17, the strong-field coefficient decrease to

$$\kappa_0' = \frac{\kappa_0}{\sqrt{1 + 2I / I_{sat}}} \quad (1.20)$$

and at any frequency is proportional to $1 / \sqrt{1 + 2I / I_{sat}}$. The general solution to Eq. 1.6 for how the laser intensity varies with the distance x into the cell is then rather more complicated than Beer's law and is given in reference [15]. However, the strong-field $I \gg I_{sat}$ behavior is easily determined by neglecting the 1 compared to I / I_{sat} so that Eq.1.6 becomes

$$\frac{dI}{dx} = -\kappa \sqrt{I} \quad (1.21)$$

where

$$\kappa = \kappa_0 \sqrt{I_{sat} / 2} e^{-(\nu - \nu_0)^2 / 2\sigma_\nu^2} \quad (1.22)$$

with solution

$$I(x) = \left(\sqrt{I_0} - \frac{\kappa x}{2} \right)^2 \quad (1.23)$$

1.4 Multilevel effects

Real atoms have multiple upper and lower energy levels which add complexities to the simple two-level model presented so far. Transitions between two lower levels and four upper levels add features called crossover resonances and a process called optical pumping. Crossover resonance is additional narrow absorption dips arising because several upper or lower levels are close enough in energy that their Doppler-broadened profiles overlap. Optical pumping occurs when the excited level can spontaneously decay to more than one lower level. It can significantly deplete certain ground state populations.

Optical pumping in rubidium can be modeled in terms of the Λ -type three-level atom, where the two lower levels are separated in energy by much more than a Doppler width (Fig. 1.5)

Assume the laser beam is resonant with atoms in only one of the lower levels, but atoms in the excited level spontaneously decay to either lower level more or less equally. Then, each time an atom in the “resonant” lower level is promoted by the laser to the excited level, some fraction of the time it will decay to the “non-resonant” lower level.

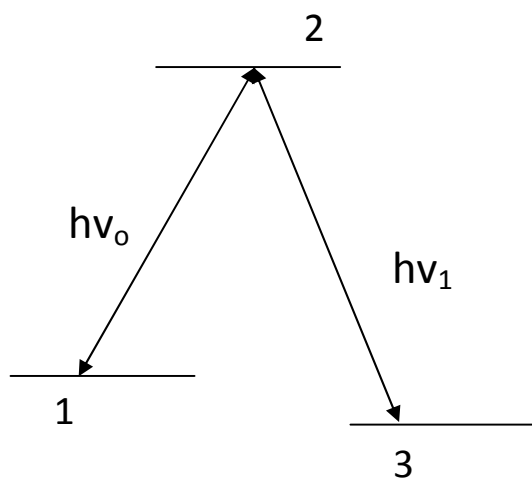


Figure 1.5 Idealized three-level Λ system.

Once in the non-resonant lower level, the atom no longer interacts with the laser field. It becomes “shelved” and unable to contribute to the absorption. Analysis of the level populations then requires a model where atoms outside the laser beam interaction volume randomly diffuse back into it thereby replenishing the resonant lower level populations. Depending on the laser intensity and beam geometry, the lower level populations can be significantly altered by optical pumping.

As with the population variations arising from stimulated emission and absorption, optical pumping also depends on the laser frequency and atom velocities. Optical pumping due to the pump beam can drastically deplete resonant ground state atoms.

1.5 Energy levels in rubidium

Hyperfine splitting of atomic spectral lines is so small that Doppler broadening *normally makes it impossible to resolve the lines*. In principle, quantum mechanical

calculations can accurately predict the energy levels and electronic wavefunctions of multielectron atoms.

The crudest treatment of the energy levels in multielectron atoms is called the central field approximation (CFA). In this approximation the nuclear and electron magnetic moments are ignored and the atomic electrons are assumed to interact, not with each other, but with an effective radial electric field arising from the average charge distribution from the nucleus and all the other electrons in the atom.

Solving for the energy levels in the CFA leads to an atomic configuration in which each electron is described by the following quantum numbers:

1. The principal quantum number n (allowed integer values greater than zero) characterizes the radial dependence of the wavefunction.
2. The orbital angular momentum quantum number ℓ (allowed values from 0 to $n - 1$) characterizes the angular dependence of the wavefunction and the magnitude of the orbital angular momentum ℓ of an individual electron.³
3. The magnetic quantum number m_ℓ (allowed values from $-\ell$ to ℓ) further characterizes the angular dependence of the wavefunction and the projection of ℓ on a chosen quantization axis.⁴
4. The electron spin quantum number s (only allowed value equal to $1/2$) characterizes the magnitude of the intrinsic or spin angular momentum s of an individual electron.

³ Angular momentum operators such as ℓ^2 satisfy an eigenvalue equation of the form $\ell^2 \psi = \ell(\ell+1)\hbar \psi$

⁴ Angular momentum projection operators such as ℓ_z satisfy an eigenvalue equation of the form $\ell_z \psi = m_\ell \hbar \psi$

5. The spin projection quantum number m_s (allowed values $\pm 1/2$) characterizes the projection of s on a chosen quantization axis.

The rubidium atom (Rb) has atomic number 37. In its lowest (ground state) configuration it has one electron outside an inert gas (argon) core and is described with the notation $1s^2 2s^2 2p^6 3s^2 3p^6 3d^{10} 4s^2 4p^6 5s$. The integers 1 through 5 above specify principal quantum numbers n . The letters s, p, and d specify orbital angular momentum quantum numbers ℓ as 0, 1, and 2, respectively. The superscripts indicate the number of electrons with those values of n and ℓ .

The Rb ground state configuration is said to have filled shells to the 4p orbital and a single valence (or optical) electron in a 5s orbital. The next higher energy configuration has the 5s valence electron promoted to a 5p orbital with no change to the description of the remaining 36 electrons.

The Rb ground state configuration is said to have filled shells to the 4p orbital and a single valence (or optical) electron in a 5s orbital. The next higher energy configuration has the 5s valence electron promoted to a 5p orbital with no change to the description of the remaining 36 electrons.

1.5.1 Fine structure levels

Within a configuration, there can be several fine structure energy levels differing in the energy associated with the coulomb and spin-orbit interactions. The coulomb interaction is associated with the normal electrostatic potential energy kq_1q_2/r_{12} between each pair of electrons and between each electron and the nucleus. (Most, but not all of the coulomb interaction energy is included in the configuration energy.) The spin-orbit interaction is associated with the orientation energy $-\boldsymbol{\mu} \cdot \mathbf{B}$ of the magnetic dipole moment $\boldsymbol{\mu}$ of each electron in the internal magnetic field \mathbf{B} of the atom. The form and strength of these two interactions in rubidium are such that the energy levels are most accurately described in the L-S or Russell-

Saunders coupling scheme. L-S coupling introduces new angular momentum quantum numbers L , S , and J as described next.

1. L is the quantum number describing the magnitude of the total orbital angular momentum \mathbf{L} , which is the sum of the orbital angular momentum of each electron:

$$\mathbf{L} = \sum \ell_i \quad (1.24)$$

2. S is the quantum number describing the magnitude of the total electronic spin angular momentum \mathbf{S} , which is the sum of the spin angular momentum of each electron:

$$\mathbf{S} = \sum s_i \quad (1.25)$$

3. J is the quantum number describing the magnitude of the total electronic angular momentum \mathbf{J} , which is the sum of the total orbital and total spin angular momentum:

$$\mathbf{J} = \mathbf{L} + \mathbf{S} \quad (1.26)$$

The values for L and S and J are specified in a notation $^{(2S+1)}L_J$ invented by early spectroscopists. The letters S, P, and D (as with the letters s, p, and d for individual electrons) are used for L and correspond to $L = 0, 1, \text{ and } 2$, respectively. The value of $(2S + 1)$ is called the *multiplicity* and is thus 1 for $S = 0$ and called a singlet, 2 for $S = 1/2$ (doublet), 3 for $S = 1$ (triplet), etc. The value of J (with allowed values from $|L - S|$ to $|L + S|$) is annotated as a subscript to the value of L .⁵

⁵ The terms singlet, doublet, triplet etc. are associated with the number of allowed values of J typically possible with a given L and S (if $L \geq S$). Historically, the terms arose from the number of closely-spaced spectral lines typically (but not always) observed in the decay of these levels. For example, the sodium doublet at 589.0 and 589.6 nm occurs in the decay of the $^2P_{1/2}$ and $^2P_{3/2}$ fine structure levels to the $^2S_{1/2}$ ground state. While the $^2P_{1/2}$ and $^2P_{3/2}$ are truly a doublet of closely-spaced energy levels, the $^2S_{1/2}$ state has only one allowed value of J .

The sum of ℓ_i or s_i over all electrons in any filled orbital is always zero. Thus for Rb configurations with only one valence electron, there is only one allowed value for L and S : just the value of ℓ_i and s_i for that electron. In its ground state (5s) configuration, Rb is described by $L = 0$ and $S = 1/2$. The only possible value for J is then $1/2$ and the fine structure state would be labeled $^2S_{1/2}$. Its next higher (5p) configuration is described by $L = 1$ and $S = 1/2$. In this configuration there are two allowed values of J : $1/2$ and $3/2$ and these two fine structure states are labeled $^2P_{1/2}$ and $^2P_{3/2}$ (Fig.1.6).

1.5.2 Hyperfine levels

Within each fine structure level there can be an even finer set of hyperfine levels differing in the orientation energy (again, a $-\boldsymbol{\mu} \cdot \mathbf{B}$ type energy) associated with the nuclear magnetic moment in the magnetic field of the atom. The nuclear magnetic moment is much smaller than the electron magnetic moment and this is why the hyperfine splittings are so small

The nuclear magnetic moment is proportional to the spin angular momentum \mathbf{I} of the nucleus, whose magnitude is described by the quantum number I . Allowed values for I depend on nuclear structure and vary with the isotope.

The hyperfine energy levels depend on the total angular momentum \mathbf{F} of the atom: the sum of the total electron angular momentum \mathbf{J} and the nuclear spin angular momentum \mathbf{I} :

$$\mathbf{F} = \mathbf{J} + \mathbf{I} \quad (1.27)$$

The magnitude of \mathbf{F} is characterized by the quantum number F with allowed values from $|J - I|$ to $J + I$. Each state with a different value of F will have a slightly different energy due to the interaction of the nuclear magnetic moment and the internal field of the atom. There is no special notation for the labeling of hyperfine states and F is usually labeled explicitly in energy level diagrams.

There are two naturally occurring isotopes of Rb: 72% abundant ^{87}Rb with $I = 3/2$ and 28% abundant ^{85}Rb with $I = 5/2$. (Fig.1.1) For both isotopes, this leads to two hyperfine levels within the $^2\text{S}_{1/2}$ and $^2\text{P}_{1/2}$ fine structure levels ($F = I - 1/2$ and $F = I + 1/2$) and four hyperfine levels within the $^2\text{P}_{3/2}$ fine structure level ($F = I - 3/2, I - 1/2, I + 1/2, I + 3/2$) (Fig.1.6).

The energies of the hyperfine levels can be expressed (relative to a “mean” energy E_J for the fine structure state) in terms of two hyperfine constants A and B by the Casimir formula

$$E_F = E_J + A \frac{\kappa}{2} + B \frac{3\kappa(\kappa+1)/4 - I(I+1)J(J+1)}{2I(2I-1)J(2J-1)} \quad (1.28)$$

where $\kappa = F(F+1) - J(J+1) - I(I+1)$ (If either $I=1/2$ or $J=1/2$, the term containing B must be omitted.)

Table 1.2: Hyperfine constants A and B (in MHz) for the lowest three fine structure states in the two naturally-occurring Rb isotopes

| Iso | fss | A | B |
|------------------|--------------------|---------|-------|
| ^{85}Rb | $^2\text{S}_{1/2}$ | 1011.91 | — |
| | $^2\text{P}_{1/2}$ | 120.72 | — |
| | $^2\text{P}_{3/2}$ | 25.01 | 25.88 |
| ^{87}Rb | $^2\text{S}_{1/2}$ | 3417.34 | — |
| | $^2\text{P}_{1/2}$ | 406.2 | — |
| | $^2\text{P}_{3/2}$ | 84.8 | 12.52 |

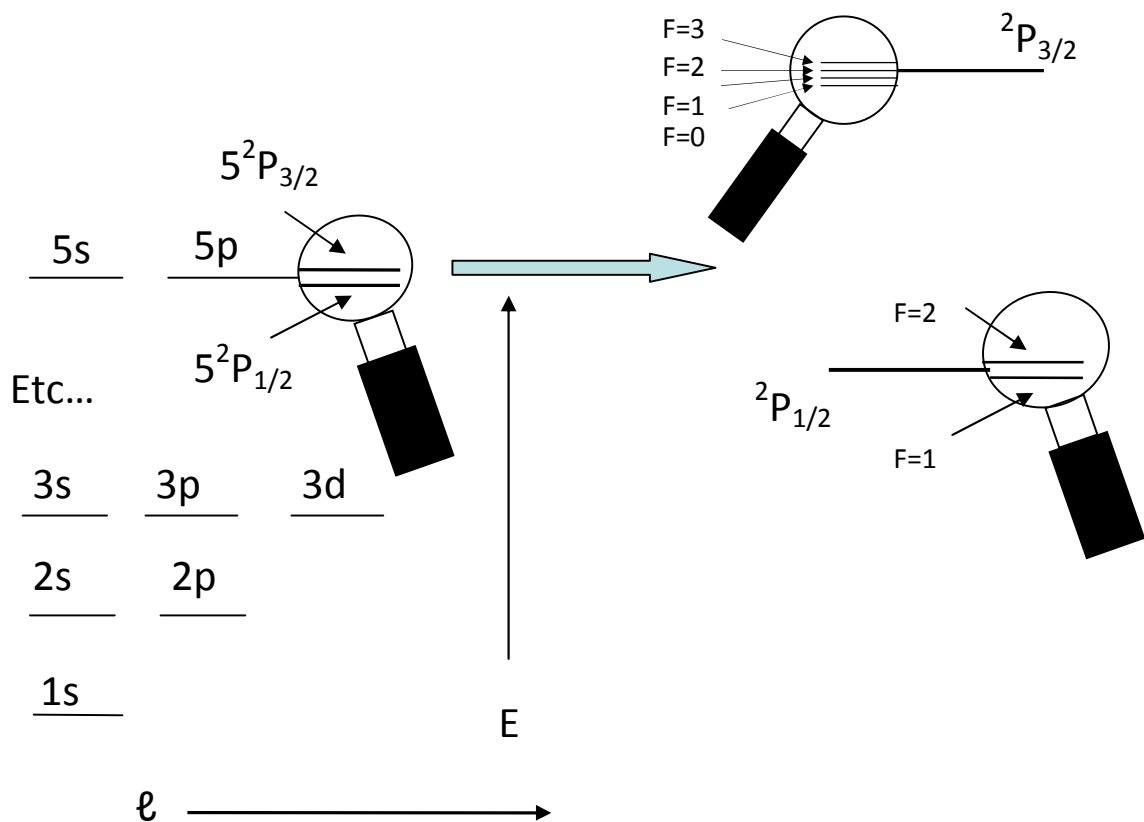


Figure 1.6 The basic energy-level structure of a one electron atom(at the left). Bound states have negative energy and are quantized, with different allowed amounts of angular momentum for each energy level. To first approximation, all of the different angular momentum states have the same energy for a given energy number n. Fine structure (at the left en zoom) Taking the spin of the electron into account leads to a small splitting of the levels with orbital angular momentum. There are two angular momentum to consider, orbital and spin. The new notation is $^{2S+1}L_J$, where S is the electron spin (1/2 for one electron), L is the orbital angular momentum (S, P, D, etc.), and $J = L + S$ is the total angular momentum.

Hyperfine structure (at the right zoom)– Adding the spin of the nucleus further splits the levels. Here we have a close up of the 2p levels, split into $^2P_{1/2}$ and $^2P_{3/2}$ by the fine-structure correction. These fine-structure levels are split according to the total angular momentum $F = I + J$. This example illustrates the splitting for ^{87}Rb , which has $I = 3/2$. The $^2S_{1/2}$ level also gets split, in the same way as $^2P_{1/2}$. (Fig.1.7)

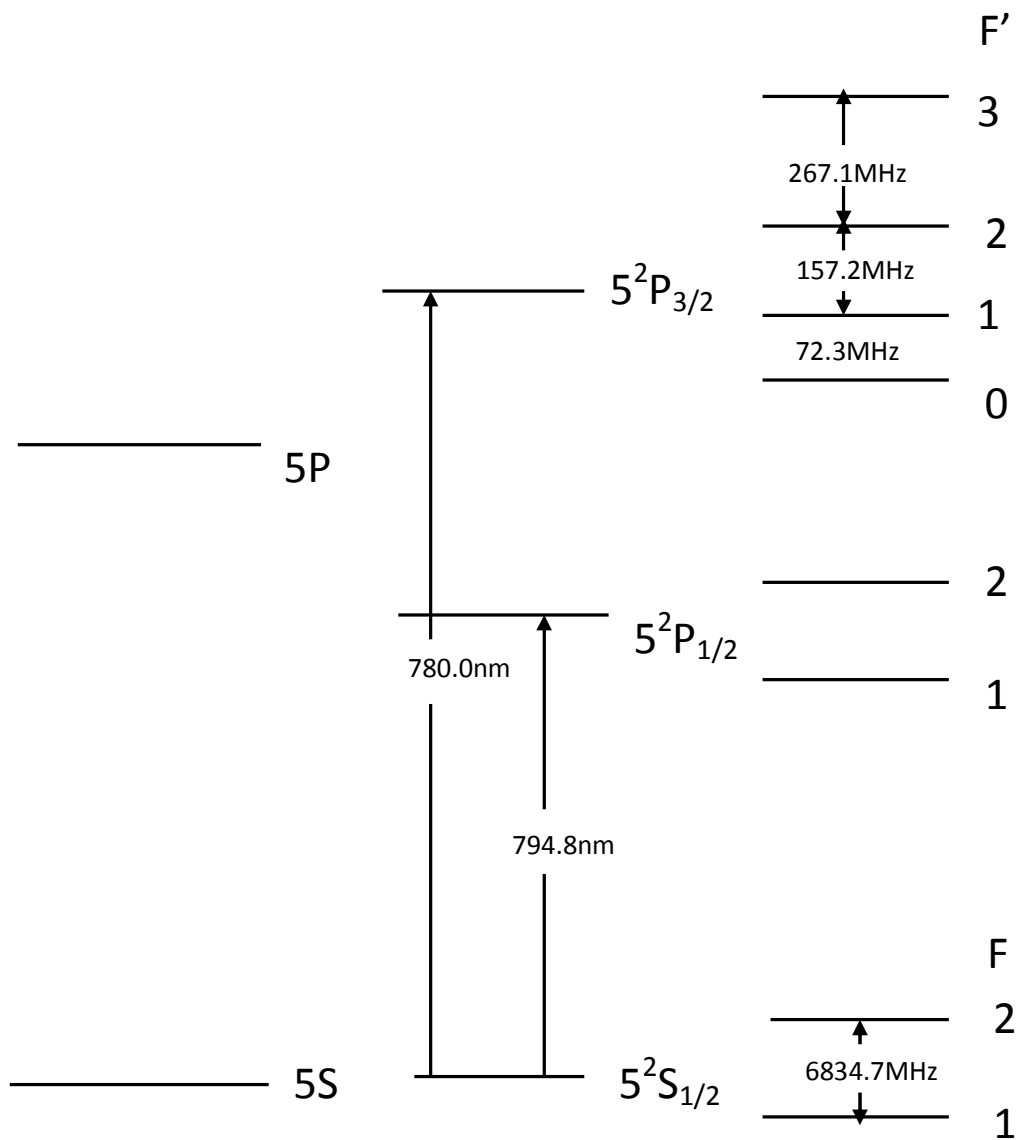


Figure 1.7 Hyperfine structure– Adding the spin of the nucleus further splits the levels. Here we have a close up of the 2p levels, split into $^2P_{1/2}$ and $^2P_{3/2}$ by the fine-structure correction. These fine-structure levels are split according to the total angular momentum $F = I + J$. This example illustrates the splitting for ^{87}Rb , which has $I = 3/2$. The $^2S_{1/2}$ level also gets split, in the same way as $^2P_{1/2}$.

1.5.3 Transitions

The $^2S_{1/2}$ to $^2P_{1/2}$ transitions are all around 795 nm while the $^2S_{1/2}$ to $^2P_{3/2}$ transitions are all around 780 nm. We will only discuss the 780 nm transitions that can be reached with the laser used in our experiment. Dipole transitions follow the selection rule $\Delta F = 0, \pm 1$.

Thus, in each isotope, the allowed transitions from the $^2S_{1/2}$ to $^2P_{3/2}$ fall into two groups of three, with each group labeled by the F of the $^2S_{1/2}$ state. Because the hyperfine splitting between the two $^2S_{1/2}$ levels is large compared to the hyperfine splittings among the four $^2P_{3/2}$ levels, the groups will be well separated from each other. Within each group, the three possible transitions can be labeled by the F' of the $^2P_{3/2}$ state. These three transitions will be more closely spaced in energy

1.6 Zeeman Effect

Applying an external magnetic field further splits each of the F levels according to their projection number m (See Figure 1.8) All this says is that the energy of the system (atom plus magnetic field) is different for different orientations of the atom, which is a perfectly reasonable assertion. This splitting is known as the Zeeman Effect. The fundamental physics of the Zeeman Effect is essentially the same as that of the fine and hyperfine splittings in that all three are due to coupling between magnetic fields and magnetic moments. The difference is that the Zeeman Effect is due to a magnetic field we apply in the lab, whereas the fine and hyperfine splittings are due to intrinsic magnetic fields that occur inside the atom itself.

If the magnetic field is relatively weak, the Zeeman splitting is given by a simple expression.

$$E_z = g_F \mu_B B m \quad (1.29)$$

Here, E_Z is the Zeeman energy, the difference in energy between the state with projection number m and the unperturbed hyperfine level. The magnetic field strength is B , μ_B is the Bohr magneton, and the coupling constant g_F is known as the Landé g -factor. This g -factor is not the same as the bare electron's g -factor, and it is different for each hyperfine level.

$$g_F = g_J \frac{F(F+1) + J(J+1) - I(I+1)}{2F(F+1)} \quad (1.30)$$

and

$$g_J = 1 + \frac{J(J+1) + F(F+1) - L(L+1)}{2J(J+1)} \quad (1.31)$$

The fine-structure splitting is very, very small compared with the spacing between the excitation levels 1s, 2s, etc., and the hyperfine splitting is much, much smaller still. The Zeeman splitting, however, can conceivably be as big as the hyperfine splitting, or even bigger, if a strong enough magnetic field is applied.

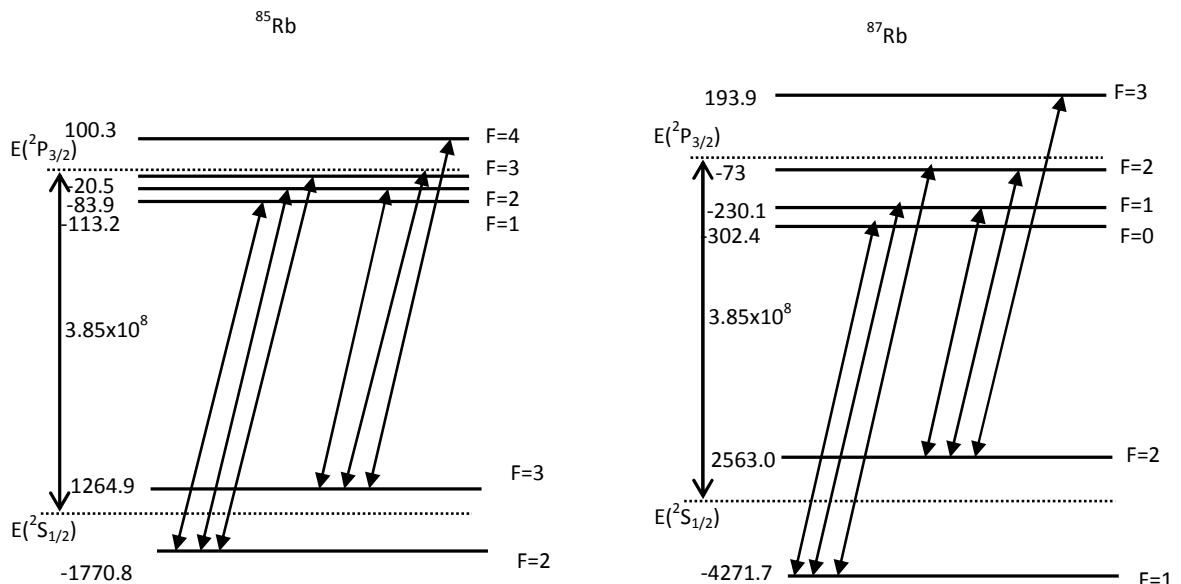


Figure 1.8. Energy levels for ^{85}Rb and ^{87}Rb (not to scale). Note that the hyperfine splittings are about an order of magnitude larger in the ground $^2S_{1/2}$ levels compared to the excited $^2P_{3/2}$ levels [16]

The density of the Rubidium gas as a function of temperature is given approximately in Table 1.3.

Table 1.3: Density of Rubidium gas as a function of temperature

| T(K) | $\rho(m^{-3})$ |
|------|----------------------|
| 290 | 3.3×10^{15} |
| 300 | 1.1×10^{16} |
| 310 | 2.9×10^{16} |
| 320 | 7.5×10^{16} |
| 330 | 1.8×10^{17} |
| 340 | 4.3×10^{17} |
| 350 | 8.3×10^{17} |
| 360 | 1.5×10^{18} |
| 370 | 3.7×10^{18} |
| 380 | 6.3×10^{18} |
| 390 | 1.2×10^{19} |
| 400 | 2.4×10^{19} |

Chapter 2 Nonlinear properties of Rb

Our main focus of this section is the nonlinear effects (i.e., effects in which optical properties of the medium are modified by interaction with light). We also discuss the nonlinear magneto-optics in atomic vapors, and the relation between nonlinear magneto-optics and a variety of other phenomena and techniques, such as Faraday rotation, electromagnetically induced transparency, nonlinear electro-optical effects, and self-rotation.

2.1 Introduction

Since the first observation of nonlinear (NL) effects, many materials have been investigated concerning their nonlinear optical properties [17, 18]. Nonlinear materials can be found among gases and vapors, polymers, liquid crystals, organic solvents, or crystals – in short, in nearly every material system.

A linear dielectric medium is characterized by a linear relation between the polarization density P and the electric field E , $P = \epsilon_0 \chi E$, where ϵ_0 is the vacuum permittivity and χ is the electric susceptibility of the medium. A nonlinear dielectric medium, on the other hand, is characterized by a nonlinear relation between P and E .

The nonlinearity may be of microscopic or macroscopic origin. The polarization density $P = Np$ is a product of the individual dipole moment p (which is induced by the applied electric field E) and the number density of dipole moments N . The nonlinear behavior may have its origin in either p or N .

2.2 Material-Based Classification of Nonlinear Optical Effects

When considering nonlinear effects [19], one must distinguish between resonant (where the optical frequency is resonant with an electronic transition in the material), non-resonant, and intrinsic and extrinsic effects [20, 21]

2.3 Absorption, Induced, and Spontaneous Emission

Assume that atoms with the energy levels E_1 and E_2 have been brought into the radiation field. If a molecule absorbs a photon of energy $h\nu = E_2 - E_1$, it is excited from the lower energy level E_1 into the higher level E_2 (Fig. 2.1). This process is called induced absorption. The probability per second that a molecule will absorb a photon, $\frac{d}{dt}P_{12}$, is proportional to the number of photons of energy $h\nu$ per unit volume and can be expressed in terms of the spectral energy density $\rho_\nu(\nu)$ of the radiation field as

$$\frac{d}{dt}P_{12} = B_{12}\rho(\nu) \quad (2.1)$$

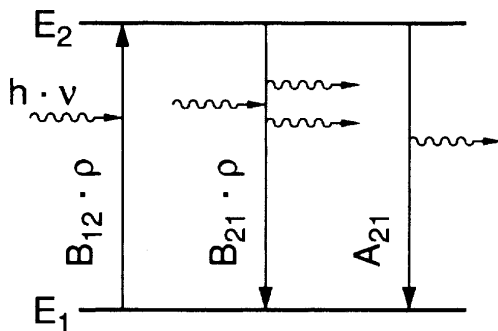


Figure 2.1 Schematic diagram of the interaction of a two-level system with a radiation field

The constant factor B_{12} is the Einstein coefficient of induced absorption. It depends on the electronic structure of the atom, i.e. on its electronic wave functions in the two levels $|1\rangle$ and $|2\rangle$. Each absorbed photon of energy $h\nu$ decreases the number of photons in one mode of the radiation field by one.

The radiation field can also induce molecules in the excited state E_2 to

make a transition to the lower state E_1 with simultaneous emission of a photon of energy $h\nu$. This process is called induced (or stimulated) emission. The induced photon of energy $h\nu$ is emitted into the same mode that caused the emission. This means that the number of photons in this mode is increased by one. The probability $\frac{d}{dt}P_{21}$, that one molecule emits one induced photon per second is in analogy to Eq.(2.1)

$$\frac{d}{dt}P_{21} = B_{21}\rho(\nu) \quad (2.2)$$

The constant factor B_{21} is the Einstein coefficient of induced emission. A_{21} is the Einstein coefficient of spontaneous emission and is often called the spontaneous transition probability. For relations between the three Einstein coefficients B_{12} , B_{21} , and A_{21} see [22].

2.4 Self-interaction of the light with atoms

Self-interaction of laser beams in a medium that is due to changes in its properties induced by incident radiation is among the most interesting phenomena in nonlinear optics. Self-focusing and self-defocusing of a light beam, self-rotation of the plane of polarization, self-phase modulation and so on, are examples [23, 24]. If the light used to study nonlinear magneto-optical rotation is elliptically polarized, additional optical rotation can occur due to nonlinear self rotation [25-29]. This effect is determined solely by the ellipticity of the electromagnetic field, and exists without any external magnetic fields. Self-rotation arises when the elliptically polarized light field causes the atomic medium to acquire circular birefringence and linear dichroism, causing optical rotation. There are several physical mechanisms that can lead to self-rotation in atomic media. This effect can be caused by Kerr nonlinearity in solids and liquids [30,31] optical pumping and ac-Stark shifts in atomic vapor [32-38], and other mechanisms.

2.5 Nonlinear Faraday rotation

The linear near-resonance Faraday effect is also known as the Macaluso-Corbino effect.

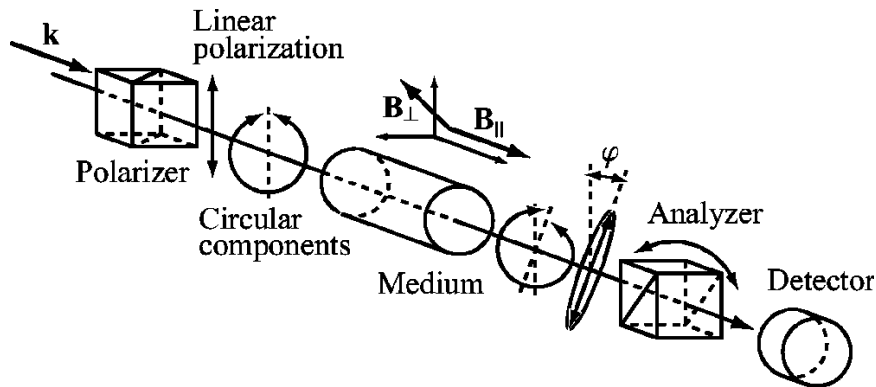


Figure 2.2 The Faraday and Voigt effects. In the Faraday effect light, after passing through a linear polarizer, enters a medium subjected to a longitudinal magnetic field $\mathbf{B}_{||}$ ($\mathbf{B}_{\perp} = 0$). Left- and right-circularly polarized components of the light (equal in amplitude for linearly polarized light) acquire different phase shifts, leading to optical rotation. A difference in absorption between the two components induces ellipticity in the output light. The intensity of the transmitted light with a particular polarization is detected depending on the orientation of the analyzer relative to the polarizer. Analyzer orientation varies with the type of experiment being performed. In forward scattering experiments, the analyzer is crossed with the input polarizer, so that only light of the orthogonal polarization is detected. In the “balanced polarimeter” arrangement, a polarizing beam splitter oriented at $\pi/4$ to the input polarizer is used as an analyzer. In this case, the normalized differential signal between the two channels of the analyzer depends on the rotation of light polarization while being insensitive to induced ellipticity. The Voigt effect is similar except that instead of a longitudinal magnetic field, a transverse field \mathbf{B}_{\perp} ($\mathbf{B}_{||} = 0$) is applied. Here optical rotation and induced ellipticity are due to differential absorption and phase shifts of orthogonal linearly polarized components of the input light

The magnitude of optical rotation per unit magnetic field and unit length is characterized by the *Verdet constant* V . For typical dense flint glasses that are used in commercial Faraday polarization rotators and optical isolators,

$V \cong 3 \times 10^{-5} \text{ rad G}^{-1} \text{ cm}^{-1}$. In resonant rubidium vapor (whose density, $\sim 3 \times 10^9 \text{ cm}^{-3}$, satisfies the definition of very high vacuum) nonlinear magneto-optical rotation corresponds to $V \cong 10^4 \text{ rad G}^{-1} \text{ cm}^{-1}$.

2.6 Mechanisms of the linear magneto-optical effects

The principal mechanism of the linear Macaluso-Corbino effect can be illustrated by the case of $F = 1 \rightarrow F' = 0$ transition (Fig. 2.3), where F, F' are the total angular momenta. Linearly polarized light incident on the sample can be decomposed into two counter-rotating circular components σ^\pm . In the absence of a magnetic field, the $M = \pm 1$ sublevels are degenerate and the optical resonance frequencies for σ^+ and σ^- coincide.

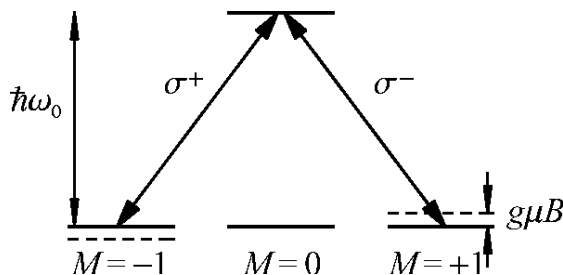


Figure 2.3 An $F = 1 \rightarrow F' = 0$ atomic transition. In the presence of a longitudinal magnetic field, the Zeeman sublevels of the ground state are shifted in energy by $g\mu_B M$. This leads to a difference in resonance frequencies for left- (σ^+) and right- (σ^-) circularly polarized light.

The real part of the refractive index n associated with the atomic medium is shown in Fig. 2.4 as a function of the light frequency detuning Δ (the solid dispersion curve). The refractive index is the same for the two circular components.

When a magnetic field is applied, however, the Zeeman shifts lead to a difference between the resonance frequencies for the two circular polarizations. This displaces the dispersion curves for the two polarizations as shown in Fig.2.3. A characteristic width of these dispersion curves, Γ corresponds to the spectral width (full width at half maximum, or FWHM) of an absorption line. Under typical experimental conditions in a vapor cell this width is dominated by the Doppler width and is on the order of 1 GHz for optical transitions. The difference between n_+ and n_- (Fig. 2.4) signifies a difference in phase velocities of the two circular components of light and, as a result, the plane of polarization rotates through an angle

$$\varphi = \pi(n_+ - n_-)\frac{l}{\lambda} \quad (2.3)$$

Here l is the length of the sample, and λ is the wavelength of light.

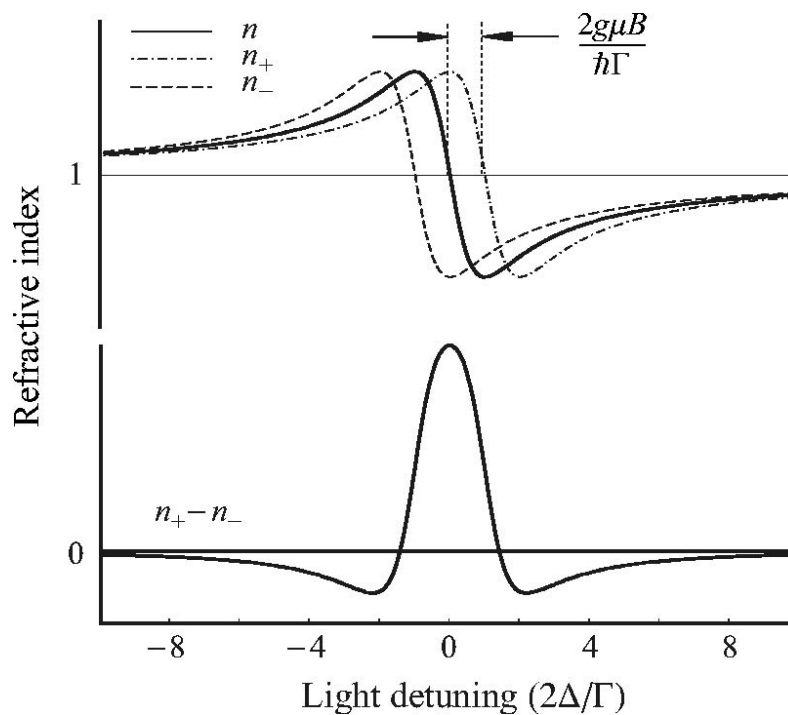


Figure 2.4 The dependence of the refractive index on light frequency detuning Δ in the absence (n) and in the presence (n_{\pm}) of a magnetic field. Shown is the case of $g\mu B = \hbar\Gamma$ and a Lorentzian model for line broadening (Fig.1.2) The lower curve shows the difference of refractive indices for the two circular polarization components. The spectral dependence of this difference gives the characteristic spectral shape of the linear magneto-optical rotation (the Macaluso-Corbino effect).

In addition to the difference in refraction for the two circular polarizations (circular birefringence), there also arises a difference in absorption (circular dichroism). Thus linear light polarization before the sample generally evolves into elliptical polarization after the sample. For nearly monochromatic light (i.e., light with spectral width much smaller than the transition width), and for zero frequency detuning from the resonance, the optical rotation in the sample as a function of magnetic field B can be estimated from Eq. (2.3) as [39]

$$\varphi \sim \left\{ (2g\mu_B / h\Gamma) / [1 + (2g\mu_B H / h\Gamma)^2] \right\} l / l_0 \quad (2.4)$$

Where the Zeeman splitting of levels is $\nu_z = g\mu_B H / h$, g is the Landé factor, μ_B is Bohr magneton, H is magnetic field strength, h is Planck's constant, Γ is the resonant transition linewidth, l is the medium length, l_0 is the absorption length. Rotation angle φ is linearly proportional to the applied magnetic field H for Zeeman shifts ν_z smaller than resonant linewidth Γ , has a peak at $2\nu_z \sim \Gamma$ and falls down in the limit of large fields. In typical vapor cell experiments with *weak* light fields Faraday rotation is to first order independent of light power (linear Faraday rotation). The spectral width of Faraday rotation features is dominated by Doppler broadening, which is of the order of 1GHz for optical transitions at room temperature. In nonlinear spectroscopy it is possible to achieve much narrower linewidth for optical transitions, than in linear optics [40]

For atoms with nonzero nuclear spin, mixing of different hyperfine components (states of the same M but different F) by a magnetic field also leads to linear magneto-optical effects [41-44]. The contribution of this mechanism is comparable to that of the level-shift effect discussed above in many practical situations, e.g., linear magneto-optical rotation in the vicinity of the alkali D lines [44]. For the Faraday geometry and when $g\mu_B \ll \hbar\Gamma \ll \Delta_{hfs}$, the amplitude of the rotation can be estimated as

$$\varphi \cong \frac{g\mu_B}{\Delta_{hfs}} \frac{l}{l_0} \quad (2.5)$$

where Δ_{hfs} is the separation between hyperfine levels. Since hyperfine mixing leads to a difference in the magnitude of n_+ and n_- (and not the difference in resonance frequencies as in the level-shift effect), the spectral profile of the rotation for the

hyperfine mixing effect corresponds to dispersion-shaped curves centered on the hyperfine components of the transition.

2.7 Self rotation (SR)

If the light used to study nonlinear magneto-optical rotation is elliptically polarized, additional optical rotation (present in the absence of a magnetic field) can occur due to nonlinear SR. SR arises when the elliptically polarized light field causes the atomic medium to acquire circular birefringence and linear dichroism, causing optical rotation. There are several physical mechanisms that can lead to SR in atomic media. These are discussed in detail in Ref. [45]. Optical rotation can be caused by circular birefringence, created by either a difference in the populations (due to optical pumping) or the energies (due to ac Stark shifts) of the Zeeman sublevels. At high power, orientation-to-alignment conversion can generate atomic alignment not along the axes of light polarization, leading to optical rotation due to linear dichroism.

SR can play an important role in the output polarization of gas lasers and in high-resolution polarization spectroscopy. SR in alkali vapors has been studied experimentally in [46-48]

2.8 Self-phase modulation

At high intensities the refractive index of a medium starts to show an intensity-dependence, according to:

$$n = n_0 + n_2 I \quad (2.6)$$

Due to the temporal variation of the intensity, the refractive index will also vary in time, which means that different parts of the pulse experience different responses from the medium [49]. The variation in refractive index causes a self-induced phase shift in the pulse that increases with propagated distance according to:

$$\begin{aligned}
\phi &= \beta z - \omega_0 t = \frac{\omega_0 n(t) z}{c} - \omega_0 t = \\
&= \frac{\omega_0 n_0 z}{c} + \frac{\omega_0 n_2 I(t) z}{c} - \omega_0 t
\end{aligned} \tag{2.7}$$

where the intensity-dependent nonlinear phase shift $\phi_{NL} = \frac{\omega_0 n_2 I(t) z}{c}$ is due to

nonlinear refraction. Since the instantaneous frequency of the pulse is given by the derivative of the temporal phase, the frequency will also show an intensity and time-dependence according to:

$$\omega = -\frac{\partial \phi}{\partial t} = \omega_0 - \frac{\omega_0 n_2}{c} \frac{\partial I}{\partial t} z \tag{2.8}$$

It is thus obvious that new frequency components will be generated as the pulse propagates in the medium. This phenomenon is referred to as self-phase modulation (SPM), the temporal counterpart to the optical Kerr-effect.

2.9 Resonant Absorption and Refractive Index in Rubidium

Consider a simple model for a rubidium atom, namely that of a single electron bound by a harmonic force, acted upon by the electric field of an incident laser [50].

Although crude, this model does allow us to write down the basic optical properties of a gas of atoms near an atomic resonance. The equation of motion for the electron around the atom is

$$m[x + \gamma \dot{x} + \omega_0^2 x] = -eE(x, t) \tag{2.9}$$

Where γ measures a phenomenological damping force. If the electric field varies in time as $Ee^{-i\omega t}$, then the dipole moment contributed by one atom is

$$p = -ex = \left(\frac{e^2}{m} \right) (\omega_0^2 - \omega^2 - i\omega\gamma)^{-1} E = \epsilon_0 \chi_e E \quad (2.10)$$

where χ_e is called the electric susceptibility. If there are N atoms per unit volume, then the (complex) dielectric constant of the gas is given by

$$\epsilon(\omega) / \epsilon_0 = 1 + 4\pi N \chi_e = 1 + \frac{4\pi N f e^2 / m}{(\omega_0^2 - \omega^2 - i\omega\gamma)} \quad (2.11)$$

where f is a standard fudge factor, called the “oscillator strength” of the transition. Adding the oscillator strength factor makes this simple classical calculation agree with a more realistic quantum mechanical calculation.

The oscillator strength is of order unity for strong transitions like the $S \rightarrow P$ rubidium lines, and is much smaller for forbidden atomic transitions. Both the oscillator strength and the damping factor γ are difficult to calculate for real atoms, since doing so requires quite a lot of detailed atomic physics.

Maxwell’s equations (MKS units) for a propagating electromagnetic wave give us

$$\nabla^2 E - \mu \epsilon \frac{\partial^2 E}{\partial t^2} = 0 \quad (2.12)$$

and we define an index of refraction $n = c/v = \sqrt{\epsilon\mu / \epsilon_0\mu_0}$ where v is the speed of wave propagation. Assuming $\mu / \mu_0 \cong 1$ and the above expression for the dielectric constant ϵ / ϵ_0 , we find ourselves with a complex index of refraction, which we write

$$n = \sqrt{\epsilon / \epsilon_0} = n(1 + i\kappa) \quad (2.13)$$

where n_0 and κ are real quantities. Evaluating Eq. 2.11 gives

$$\begin{aligned}
\operatorname{Re}(\sqrt{\varepsilon/\varepsilon_0}) &= n_0 \\
&\cong 1 - \frac{2\pi(\omega^2 - \omega_0^2)Nfe^2/m}{(\omega^2 - \omega_0^2)^2 + \gamma^2\omega^2} \\
&\cong 1 - \frac{\pi\Delta\omega Nfe^2/m\omega_0}{\Delta\omega^2 + \gamma^2/4}
\end{aligned} \tag{2.14}$$

$$\begin{aligned}
\operatorname{Im}(\sqrt{\varepsilon/\varepsilon_0}) &= n_0\kappa \\
&\cong \frac{2\pi Nf\omega\gamma e^2/m}{(\omega^2 - \omega_0^2)^2 + \gamma^2\omega^2} \\
&\cong \frac{\pi Nf\gamma e^2/2m\omega_0}{\Delta\omega^2 + \gamma^2/4}
\end{aligned} \tag{2.15}$$

where $\Delta\omega = \omega - \omega_0$. These are plotted in Figure 2.5. This is the index of refraction for a dilute atomic gas, which of course is proportional to the atom density.

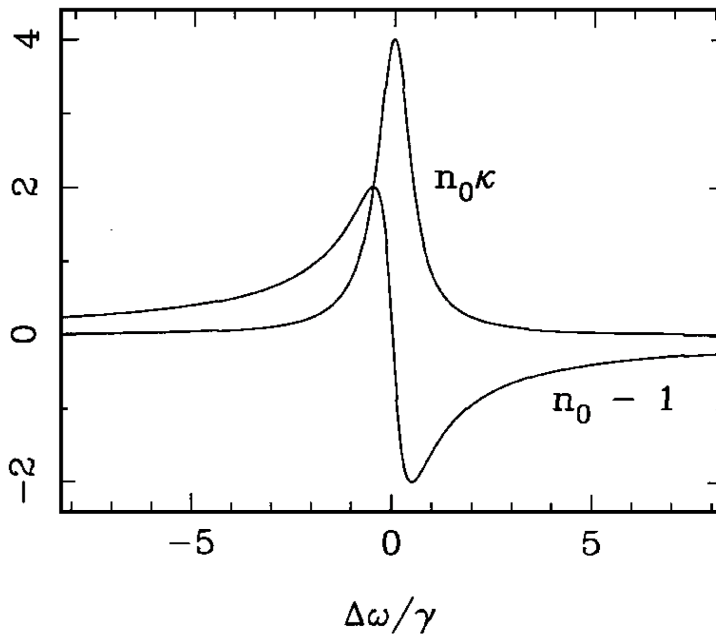


Figure 2.5 Plot of the absorption $n_0\kappa$ and refractive index change $n_0 - 1$ for a gas near an atomic resonance. Note the index change is proportional to the first derivative of the absorption.

An electromagnetic wave in the medium propagates according to

$$e^{-i(\omega t - nkz)} = e^{-kn_0 \kappa z} e^{-i[\omega t - kn_0 z]} \quad (2.16)$$

where $k = \omega / c$. From this it can be seen that n_0 is the usual index of refraction, equal to c / v , while κ describes the attenuation of the wave. Note that a relation $n_0 - 1 \cong -2\Delta\omega\kappa / \gamma$ exists between the index of refraction and the attenuation, which is independent of the oscillator strength of the atomic transition. This relation, showing that $n_0(\nu)$ and $\kappa(\nu)$ can be derived from one another, is an example of the more general Kramers-Kronig relations. A full quantum mechanical treatment also yields the same relation for the absorption and refractive index of a gas near an atomic resonance.

Chapter 3 Photorefractive Effect

3.1 Introduction

We are interested in rubidium application for dynamic holography. Because of this we make a short view of photorefractive materials which are well studied traditional media for this application and basic theory of photorefractive effect.

3.2 Photorefractive material

For holographic applications the magnitude and speed of the photorefractive effect are critical design parameters.

Attractive media for hologram recording are the photorefractive crystals.

These materials are photo-absorbing and electro-optic operates in visible range of light. Photorefractive materials can be used to store phase holograms through refractive- index modulation. They are self-developing and reusable. Their sensitivity varies as a function of the species and the experimental parameters, such as the wavelength, the charge-transport processes involved, and the writing angles.

The sillenite family (BSO),(BGO), and (BTO) is among the most sensitive photorefractive crystals, with a recording energy of $\sim 1mJ/cm^2$.

Photorefractive semiconductor crystals such as GaAs, CdTe, and InP are sensitive in the near infrared. Advantage of semiconductors is the short response time. For this reason rubidium vapor may be compared with them. The sensitivity parameter reported for fast photorefractive semiconductors is $S^{-1} \approx 10^{-5} J/cm^2$ [51], it is four orders the magnitude lower, than the estimation for rubidium, a $S^{-1} \approx 10^{-9} J/cm^2$.

3.3 Photorefractive effect

The photorefractive effect is a phenomenon in which the local index of refraction is changed by the spatial variation of the light intensity through the condition of light-induced electric fields and electro-optic effect.

Typically, the space-charge field is produced by a charge separation that results from the drift or diffusion of photo-generated charge carriers. Since the photorefractive effect follows from the electro-optic properties of the material, the induced index change depends on the symmetry of the crystal (through the electro-optic tensor) and the orientation of the space-charge field relative to the crystallographic axes. The photorefractive index change Δn can be expressed by the following equation:

$$\Delta n = \frac{1}{2} n_b^3 r_{ee} E_{sc} \quad (3.1)$$

Here n_b is the background index of refraction and r_{ee} is the effective linear electro-optic coefficient. The quantity E_{sc} is the space-charge field, and is related through Poisson's equation,

$$\nabla \cdot E_{sc} = \frac{e}{\epsilon_r} \sum_i n_i(x) \quad (3.2)$$

to the material dielectric constant, ϵ_r and the spatially varying densities of photo-generated charge carriers, $n(x)$.

3.3.1. Kukhtarev-Vinetskii's model

Although there are several models for the photorefractive effect [52, 53], the Kukhtarev-Vinetskii's model is the most widely accepted one. In this model, the photorefractive materials assumed to contain donor and acceptor traps. These traps which arise from the imperfections in the crystal create intermediate

electronic energy states in the bandgap of the insulators. When photons with sufficient energy are present, electronic transitions due to photo-excitations take place. As a result of the transitions, charge carriers are excited into the conduction band and the ionized donors become empty trap sites. The rate of carrier generation is $(sI + \beta)(N_D - N_D^+)$, whereas the rate of trap capture is $\gamma_R N_D N_D^+$. Here s is the cross section of photo-ionization, β is the rate of thermal generation, γ_R is the carrier-ionized trap recombination rate, and N_D and N_D^+ stand for the concentration of the carriers and ionized traps. N_D is the density of the donor traps.

The space-charge field produced by the migration of the charge carriers is determined by the following set of equations [54]:

$$\frac{\partial}{\partial t} N = \frac{\partial}{\partial t} N_D^+ - \frac{1}{e} \nabla \cdot \mathcal{J} \quad (3.3)$$

$$\frac{\partial}{\partial t} N_D^+ = (sI + \beta)(N_D - N_D^+) - \gamma_R N N_D^+ \quad (3.4)$$

$$\mathcal{J} = e\mu N \left(E - \frac{kT}{e} \nabla \log N \right) + pI\bar{c} \quad (3.5)$$

$$\nabla \cdot (\epsilon \bar{E}^{sc}) = e(N_A + N - N_D^+) \quad (3.6)$$

Where \bar{c} is the unit vector along the c axis of the crystal, I is the light intensity, N_A is the acceptor concentration, μ is the mobility, T is temperature, k is the Boltzmann constant, n is the index of refraction, ϵ is the dielectric tensor, pI is the photovoltaic current, and p is the photovoltaic constant. \bar{E}^{sc} stand for the space-

charge field. \vec{E} is the total field which includes \vec{E}^{sc} and any external or internal fields.

As a result of the presence of space-charge field, a change in the index of refraction is induced via the linear electro-optic effect [55] (Pockels effect):

$$\Delta\left(\frac{1}{n^2}\right)_{ij} = r_{ijk} \vec{E}_k^{sc} \quad (3.7)$$

where r_{ijk} is the electro-optic coefficient (with $i, j, k = x, y, z$)

3.4 Two-Wave Mixing

Interest in TWM (sometimes referred to as two-beam coupling) arise from the strong nonreciprocal energy exchange at relatively lower intensities between two coherent laser beams. We used process of the two-wave mixing (TWM) in our experiment for detecting dynamic hologram in the rubidium vapor, and in this section we briefly reproduce a theory of this physical process. Two type of TWM exist, they are degenerate two-wave mixing (DTWM) and non-degenerate (NTWM). In the case of DTWM, the two beams are of the same frequency, and a stationary interference pattern is formed. In the experimental part of this thesis we use two slightly different frequencies (quasi-degenerate state).

3.4.1 Theory of Two-Wave Mixing

When the frequencies of the two laser beams are different, the interference fringe pattern is no longer stationary. A volume grating can still be induced provided the fringe pattern does not move too fast. The amplitude of the index modulation decreases as the speed of the fringe pattern increases. This is related to the finite time needed for the formation of the index grating in the medium.

Let ω_1 and ω_2 be the frequencies of the two beams. The electric field of these two beams can be written as:

$$E_j = A_j e^{i(\omega_j t - \vec{k}_j \cdot \vec{r})} \quad j = 1, 2 \quad (3.8)$$

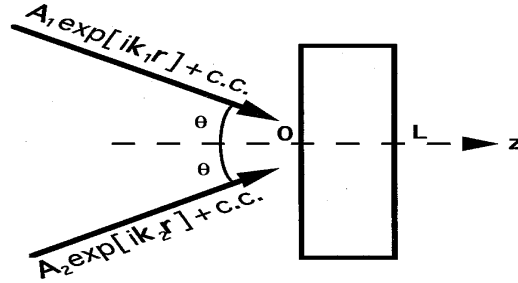


Figure 3.1. A schematic diagram of two-wave mixing in photorefractive materials

Where \vec{k}_1 and \vec{k}_2 are the wave vectors and A_1, A_2 are the wave amplitudes. The intensity of the electromagnetic radiation can be written as:

$$\begin{aligned} I &= |A_1|^2 + |A_2|^2 + A_1^* A_2 e^{i(\Omega t - \vec{K} \cdot r)} + A_1 A_2^* e^{-i(\Omega t - \vec{K} \cdot r)} \\ &= I_1 + I_2 + 2(I_1 I_2)^{1/2} \cos \Delta \varphi \end{aligned} \quad (3.9)$$

where

$$\begin{aligned} \Omega &= \omega_2 - \omega_1 \\ \vec{K} &= \vec{k}_2 - \vec{k}_1 \end{aligned} \quad (3.10)$$

and I_1, I_2 are the intensities due to the two waves acting separately, and $\Delta \varphi = \varphi_1 - \varphi_2$ is the phase difference between them

If the two waves are derived from a common source, so that they have the same phase at the origin, the phase difference $\Delta \varphi$ corresponds to an optical path difference

$$\Delta p = (\lambda / 2\pi) \Delta \varphi \quad (3.11)$$

Such intensity distribution represents a traveling fringe pattern at a speed of

$$v = \frac{\Omega}{K} = \frac{\Omega\Lambda}{2\pi} \quad (3.12)$$

where Λ is the period of the fringe pattern.

The index of refraction including the fundamental component of the intensity-induced grating can be written as:

$$n = n_0 + \frac{n_1}{2} \left\{ e^{i\phi} \frac{A_1^* A_2}{I_0} \exp[i(\Omega t - \vec{K} \cdot r)] + c.c \right\} \quad (3.13)$$

where

$$I_0 = I_1 + I_2 \equiv |A_1|^2 + |A_2|^2 \quad (3.14)$$

ϕ is real and n_1 is a real and positive number. For the sake of simplicity, we assume a scalar grating. The phase ϕ indicates the degree to which the index grating is shifted spatially with respect to the light interference pattern. According to [56], ϕ and n_1 can be written, respectively, as

$$\phi = \phi_0 - \tan^{-1}(\Omega\tau) \quad (3.15)$$

and

$$n_1 = \frac{2}{(1 + \Omega^2\tau^2)^{1/2}} \Delta n_s \quad (3.16)$$

Where τ is the decay time constant of the holograph grating, Δn_s is the saturation value of the photo-induced index change, and ϕ_0 is a constant phase shift related to the non-local response of the crystal under fringe illumination. Both parameters Δn_s and ϕ_0 depend on the grating spacing ($2\pi/K$) and its direction, as well as on the material properties of the crystal, e.g., the electro-optic coefficients.

The coupling constant, for crystals such as BaTiO₃, can be written as

$$\gamma = \gamma_0 / [1 + (\Omega \tau)^2] \quad (3.17)$$

where γ_0 is the coupling constant for the case of the degenerate two-wave mixing (i.e., $\Omega = \omega_1 - \omega_2 = 0$) and is given by

$$\gamma_0 = \frac{4\pi\Delta n_s}{\lambda \cos \theta} \quad (3.18)$$

Where θ is the angle between the beams inside the medium. In deriving (3.16), we have used $\pi/2$ for ϕ_0 in (3.14)

The two-wave mixing gain can be written as:

$$g = \frac{1+m}{1+me^{-\gamma L}} e^{-\alpha L} \quad (3.19)$$

Where m is the input beam ratio $m = I_1(0)/I_2(0)$ and L is the length of the interaction.

3.4.2 Speed of the photorefractive effect

The speed of the photorefractive effect is determined as the time required to form a refractive index grating from initial illumination of the medium. The formation of the volume index grating is a macroscopic effect that necessitates a large number of charge carriers to go through three fundamental processes: photo-excitation of charge carriers, charge transport, and recombination. Each process involves a time constant, which can be combined into a single term, referred to as the photorefractive response time τ , is defined as the time constant of the exponential build-up or decay of the refractive index grating. The process dominating the speed

of the build-up is photo-excitation of charge carriers, which is governed by the dielectric relaxation time τ_ϵ , given by [57,58]

$$\tau_\epsilon = \frac{\epsilon}{\sigma_d + \sigma_{ph}}, \quad \sigma_{ph} = \frac{4\pi e \alpha \eta \mu_e I}{\gamma_e N_A h\nu}, \quad (3.20)$$

where σ_d is the dark conductivity, σ_{ph} is the photoconductivity, α is the bulk absorption coefficient, $h\nu$ is the photon energy, μ_e is the electron mobility and η is the quantum efficiency for exciting a charge carrier. τ_ϵ determine the fundamental speed limit of the photorefractive effect, and scales inversely proportional with intensity provided $\sigma_{ph} \gg \sigma_d$. The photorefractive response time τ , is directly proportional to the dielectric time constant [57]

$$\tau = f(\Lambda, E_A) \tau_\epsilon$$

where Λ is the grating period determined by the crossing angle, θ_i , between the interacting beams. The function $f(\Lambda, E_A)$ accounts for the spatial modulation of the space charge field. For a fringe spacing that is large compared with the diffusion length and no applied field the photorefractive response time is approximately equal to the dielectric time constant, or $\tau \cong \tau_\epsilon$ [57].

3.4.3 Diffraction Efficiency

The main characteristic of the holograms is their diffraction efficiency η . In the general case it is determined by the relation of the power of the diffracted light beam (P_{diff}) to the incident power of the beam (P_{inc}):

$$\eta = P_{diff} / P_{inc} \quad (3.21)$$

The diffraction efficiency depends on the wavelength as well as on the thickness of the recording material, on whether the hologram is 3-D or 2-D, phase or amplitude and on the type of the grating profile. The diffraction efficiency can be used to determine the type of the hologram (amplitude/phase or thick/thin), as it is much higher for the phase and thick gratings. It is a function of the amplitude of the induced holographic grating and its intensity.

A list of ideal physical attributes for a holographic storage medium may include the following:

- *Recording mechanism* – a large dynamic range of optically induced, and preferably optically erasable, refractive-index change (e.g., $\Delta n \cong 10^{-3}$ to 10^{-2}), negligible absorption;
- *Sensitivity* – responsive to (widely and cheaply available) red wavelengths, an appreciable holographic writing sensitivity (e.g., on the order of $10^{-2} \text{ cm}^3 / \text{J}$) requiring low recording powers;
- *Optical quality* – suitable for casting in the form of thick slabs with large surface areas (i.e., a thick disk), high resolution (e.g., up to 5000 cycles/ mm), negligible scattering;
- *Stability* – retain recorded data indefinitely over a wide range of ambient (temperature, humidity, etc.) conditions, show low fatigue over many (e.g., millions of) write–read–erase cycles;
- *Volatility* – a (simple) physical means of “fixing” the recorded holograms so that they are not weakened (or erased) by subsequent recording and read-out beams;
- *Self-processing* – no need for processing or developing of any kind (e.g., chemical, thermal, magnetic, UV, IR, etc.) before or after recording; and last but not least,

- *Cost* – material readily and cheaply available or manufacturable.

According to Kogelnik's theory [59] on diffraction by thick gratings, the diffraction efficiency in the case of thick phase holograms with absorption is given by

$$\eta_0 = \exp(-\alpha l / \cos \theta) \sin^2 \left(\frac{\pi \Delta n l}{\lambda \cos \theta} \right) \quad (3.22)$$

where α is the absorption, l is the thickness, θ is the half-angle between reference and the object beams, Δn is the refractive-index variation, and λ is the wavelength.

3.5 Four-wave mixing

The concept of three electromagnetic fields interacting to produce a fourth field is central to the description of all four-wave mixing processes. Physically, we may understand this process by considering the individual interactions of the fields within a dielectric medium. The first input field causes an oscillating polarization in the dielectric which re-radiates with some phase shift determined by the damping of the individual dipoles; this is just traditional Rayleigh scattering described by linear optics. The application of a second field will also drive the polarization of the dielectric, and the interference of the two waves will cause harmonics in the polarization at the sum and difference frequencies. Now, application of a third field will also drive the polarization, and this will beat with both the other input fields as well as the sum and difference frequencies. This beating with the sum and difference frequencies is what gives rise to the fourth field in four-wave mixing. Since each of the beat frequencies produced can also act as new source fields, a bewildering number of interactions and fields may be produced from this basic process. The waves (1,2,3) can mix in any ways long as the mixing fulfills these criteria:

$$\mathbf{k}_4 = \pm \mathbf{k}_1 \pm \mathbf{k}_2 \pm \mathbf{k}_3$$

$$||\mathbf{k}_4|| = ||\pm \mathbf{k}_1 \pm \mathbf{k}_2 \pm \mathbf{k}_3||$$

$$\omega_4 = \pm \omega_1 \pm \omega_2 \pm \omega_3 ;$$

A mathematical model of a system's ability to support the various mixing processes is needed in order to explain the observed four-wave mixing phenomena. The third order nonlinear susceptibility $\chi^{(3)}$ is responsible for four-wave mixing processes.

For more information consult [\[60-62\]](#).

In our experiment we used low intensities and the higher order of nonlinearity didn't appear.

Chapter 4 Principles of holography

The formation of an index grating due to the presence of two coherent laser beams inside a rubidium cell is formally analogous to the recording process in conventional holography. In the following section of this introduction, we briefly review background material relevant to the rest of this thesis.

4.1 Recording of Holograms and Wavefront Reconstruction

The holographic principle makes use of the interference phenomenon, as interference allows the transfer of the phase information of a wavefront into an intensity pattern. Recording both the amplitude and phase of the wavefront of an object, i. e. recording a hologram, is performed by interference of a reference wave with complex amplitude O_0 and a coherent signal wave R_0 using a holographic plate. For the sake of simplicity we do not consider vectorial properties of the waves. The wavefront of the object is reconstructed by light diffraction if the hologram is exposed only to the reference wave.

The simplest hologram is formed by the interference of two plane waves with non-collinear propagation directions (see Fig. 4.1). In this case a pattern with sinusoidally modulated amplitude is recorded on the holographic plate, i. e., an elementary holographic grating. Exposure of this grating to the reference wave leads to diffraction along the former direction of the signal wave. Thus the wavefront of the plane signal wave is reconstructed.

More complex wavefronts are reconstructed in an analogous way. Let us consider the reference and signal waves with complex amplitudes O_0 and R_0 . Then the intensity I of the interference pattern can be expressed by

$$I \propto \left| O_0(x)e^{i\varphi_0(x)} + R_0e^{i\omega x} \right|^2 = O_x^2(x) + R_0^2 + 2O_0(x)R_0 \cos(x\omega - \varphi_0) \quad (4.1)$$

where $O_0(x)$ and R_0 , $\varphi_0(x)$ and ωx are the (real) amplitudes and phase of the object and reference waves, respectively. After exposing a photochromic film (such as a holographic plate) to the interference pattern, the absorption coefficient and hence the transmission T will become spatially modulated. In the case of a linear response of the film to intensity, i. e., $T = T_0 - \Delta T I$, the illumination of the holographic plate with the reference wave results in the reconstructed wave

$$OT = O \left[T_0 - \Delta T \left(|O|^2 + |R|^2 + O^*R + OR^* \right) \right] \quad (4.2)$$

Here, T_0 is the transmission prior to illumination and ΔT is a parameter that characterizes the photosensitivity of the film. The important term in (4.2) is $\Delta T O O^* R = \Delta T |O|^2 R$. The factor $\Delta T |O|^2$ is constant and phase independent, but the signal wave R is completely revealed with amplitude and phase. The other terms in (4.2) describe the transmitted reference wave and further diffracted waves. Separation of these particular waves from each other can be established by choosing a proper recording geometry [63-66]

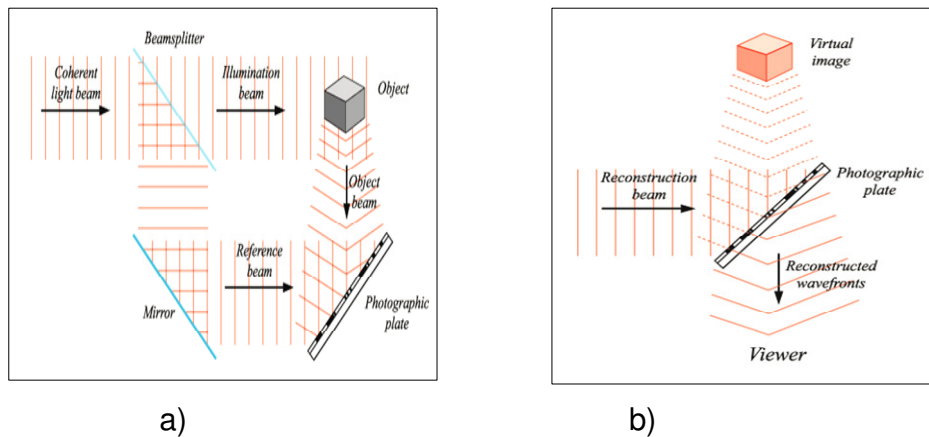


Figure 4.1 a) Recording of hologram; b) Reconstruction of hologram

The amplitude and phase information of the recorded object is stored in each singular point of the holographic plate, representing the particular viewpoint onto the object. Thus the lateral dimension of the holographic plate is the limit for the visual angle onto the recorded object. Reconstruction is even possible by exposure of only a small part of the hologram with the reference wave.

In summary, the holographic principle only requires a source of coherent waves, an object, and a photosensitive medium with sufficient spatial resolution.

4.2 Classification Scheme

The fundamental principle of recording and reconstructing an object wave can be realized in a great deal of variants, predetermined by the available recording materials, the optical setups (geometries) or techniques for recording and read out, etc. Therefore one could classify holograms, e.g., with respect to the recording scheme, the read-out configuration or the hologram properties [67].

The first step in hologram classification is to distinguish between phase or amplitude, thin or thick, transmission or reflection and static or dynamic holograms.

-Phase and Amplitude Holograms

The diffracted reference wave is then affected in its amplitude. Thus the hologram commonly is called an amplitude or absorption hologram. In other photosensitive media the refractive index or the thickness is changed upon illumination with light. In this case the phase of the reference wave is affected during diffraction, i. e., and reconstruction of the object wave. Therefore this type of hologram is called a phase hologram.

-Thin and Thick Holograms

Taking into account the effective hologram thickness and the amplitude of the absorption or phase modulation, holograms can be classified as thin or thick. Note, that effective thickness d_{eff} of the hologram has to be distinguished from the thickness of the medium d in which the hologram is recorded. They are related by $d_{eff} \leq d$. The case $d_{eff} = d$ is valid for non-absorbing media and diameters of reference and signal waves much larger than d . A rough rule of thumb defines holograms with a thickness of about the light wavelength or less as thin holograms.

- Transmission and Reflection Holograms

The classification into transmission and reflection holograms takes the direction of the wave vectors of the reference and reconstructed signal wave with respect to the holographic medium into account. A transmission hologram is characterized by the fact that both reference and signal wave are transmitted through the hologram, i. e., the signal wave is reconstructed by forward diffraction processes. For reflection holograms only the reference wave is transmitted. Reflection holograms require recording media with thicknesses much larger than the grating spacing.

- Static and Dynamic Holograms

Holograms that do not affect the reference and signal waves during recording, e.g., in holographic media that require further (chemical) processing, are called static holograms. In contrast an interaction between the recorded hologram and the recording beams leads to dynamic holograms: the recording beams themselves coherently diffract from the hologram and thus influence their own light modulation. Obviously, this feedback subsequently leads to changes of the hologram.

4.3 Dynamic holography

In static holography, recording, developing and reconstructing occur sequentially and a permanent hologram is produced.

There also exist holographic materials which do not need the developing process and can record a hologram in a very short time. This allows using holography to perform some simple operations in an all-optical way. Examples of applications of such real-time holograms include phase-conjugate mirrors ("time-reversal" of light), optical cache memories, image processing (pattern recognition of time-varying images), and optical computing.

The microscopic description of hologram formation starting from basic principles can be done for rubidium, but adequate theory is complex because of the big number of sublevels involved (Chapter I, Section 1.5). At resonance, complicated polarization behavior emerges, and geomagnetic field can radically change the observed polarization properties and diffraction efficiency.

A particularly promising application is optical phase conjugation. It allows the removal of the wavefront distortions a light beam receives when passing through an aberrating medium, by sending it back through the same aberrating medium with a conjugated phase. This is useful for example in free-space optical

communications to compensate for atmospheric turbulence (the phenomenon that gives rise to the twinkling of starlight).

4.4 Amplitude and Phase Holograms

For a pure phase, transmission hologram the absorption constant $\alpha_0 = 0$ and the solution of the coupled wave equation leads to diffraction efficiency, for the general case of slanted fringes and Bragg condition not satisfied, given by

$$\begin{aligned}
 \eta &= \sin^2(v^2 + \zeta^2)^{1/2} / (1 + \zeta^2 / v^2) \\
 v &= \pi_1 d / \lambda (c_R c_S)^{1/2} \\
 \zeta &= O d / 2c_S = \Delta \Theta K d \sin(\varphi - \Theta_0) / 2c_S \\
 &= -\Delta \lambda K^2 d / 8\pi c_S
 \end{aligned}
 \tag{4.3}$$

where c_R and c_S are the constant, O is a dephasing measure, Θ is a Bragg angle.

In the case for which there is no slant and Bragg condition is satisfied, the formula reduces to the equation

$$\eta = \sin^2(\pi_1 d / \lambda \cos \Theta_0)
 \tag{4.4}$$

A graph of this equation as a function of the optical path in units of the free space wavelength is shown in Fig.4.2. It is seen that diffraction efficiencies of 1.0 are possible for this type of hologram

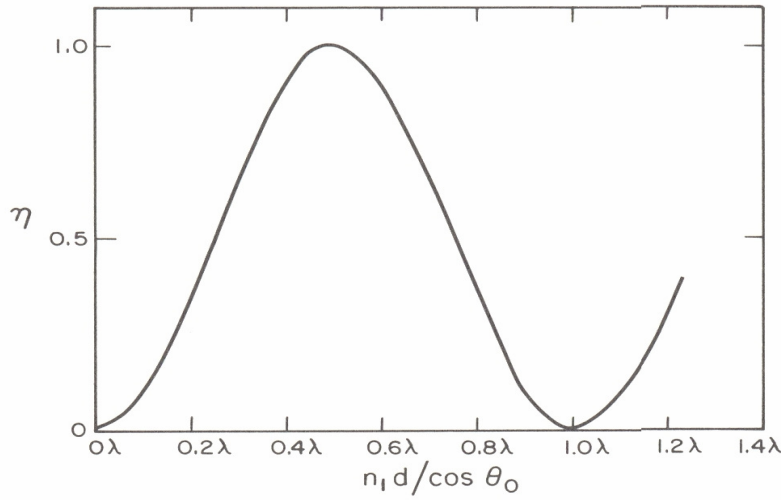


Figure 4.2 Diffraction efficiency as a function of the optical path variation in units of the wavelength for a thick phase hologram viewed in transmission.

In the case of some loss on a phase hologram in the form of some residual absorption, and the Bragg condition is not satisfied, the equation for the diffraction efficiency takes the form

$$\begin{aligned}
 \eta &= e^{-2\alpha d / \cos \Theta} \sin^2(v^2 + \zeta^2)^{1/2} / (1 + \zeta^2 / v^2) \\
 v &= \pi n_1 d / \lambda \cos \Theta \\
 \zeta &= \Delta n d / 2 \cos \Theta = \Delta \Theta \beta d \sin \Theta_0
 \end{aligned}
 \tag{4.5}$$

In the case where the Bragg condition is satisfied, the equation simplifies to

$$\eta = e^{-2\alpha d / \cos \Theta} \sin^2(\pi n_1 d / \lambda \cos \Theta_0)
 \tag{4.6}$$

For a pure amplitude hologram there is no modulation of the refractive index, so $n_1 = 0$. The solution of the coupled wave equation in this case is

$$\eta = \frac{c_R}{c_S} \exp \left[-\alpha d \left(\frac{1}{c_R} + \frac{1}{c_S} \right) \right] \sinh^2 (v^2 + \zeta^2)^{1/2} / (1 + \zeta^2 / v^2)$$

$$v = \alpha_1 d / 2(c_R c_S)^{1/2}$$

$$\zeta = \frac{1}{2} \alpha d \left(\frac{1}{c_R} - \frac{1}{c_S} \right)$$
(4.7)

In the case where the Bragg condition is satisfied, the equation simplifies to

$$\eta = e^{-2\alpha d / \cos \Theta} \sinh^2 (\alpha_1 d / \lambda \cos \Theta_0)$$
(4.8)

In the practical situation any real hologram are mixed. A mixed hologram is one for which there is a phase modulation in addition to the amplitude modulation.

In the table 4.1 summarized the principal result. The numbers shown are the maximum theoretical diffraction efficiency obtainable for each type of hologram.

With the exception of the thick, phase, reflection hologram, each of the theoretical maxima has been nearly archived experimentally. For a reason that is a yet unexplained no holographic material and process have yet come close to the theoretical 1.0 diffraction efficiency for this type of hologram.

Table 4.1 Table of maximum diffraction efficiency for various hologram types

| Hologram types | Thin Transmission | | Thick Transmission | | Thick Reflection | |
|----------------|-------------------|-------|--------------------|-------|------------------|-------|
| Modulation | Amplitude | Phase | Amplitude | Phase | Amplitude | Phase |
| Efficiency | 0.0625 | 0.339 | 0.037 | 1.000 | 0.072 | 1.000 |

Chapter 5 Density Matrix Formalism

Introduction

Nonlinear interaction of an electromagnetic field with a two-level quantum system was studied in detail in [68-70]. Particular emphasis for mathematical solution of these effects is placed in this Chapter

Resonance interaction of two-level particle with the field can be analyzed both by use the Schrodinger equation with added phenomenological relaxation terms and by use of density matrix equation, which is better suited for describing relaxation effects. Let us consider the last one.

5.1. Density Matrix Calculations for two-level system

In general, atoms can be described using the density matrix. For a two-level system, it is represented by

$$\rho = \begin{pmatrix} \rho_{aa} & \rho_{ab} \\ \rho_{ba} & \rho_{bb} \end{pmatrix} \quad (5.1)$$

where the quantities ρ_{aa} and ρ_{bb} are the population of the states a and b , and ρ_{ab} and ρ_{ba} are the coherences between them. The evolution of the atomic states is governed by the following Liouville equation,

$$i \frac{d\rho}{dt} = [H, \rho] - \frac{i}{2} \{\Gamma, \rho\} \quad (5.2)$$

where H is the Hamiltonian (See Eq. (5.3)) and Γ is the relaxation matrix.

The Hamiltonian which usually describes a light field interacting with a two-level atomic system, the ground state $|g\rangle$ and the excited state $|e\rangle$, is

$$H = \begin{pmatrix} 0 & dE \\ dE & \omega_0 \end{pmatrix} \quad (5.3)$$

where d is the transition dipole matrix element, E is the electric field of the light, and ω_0 is the energy separation between the two atomic states.

The square brackets denote the commutator of H and ρ , defined as $(H\rho - \rho H)$, and the curly brackets represent the anti-commutator of Γ and ρ , defined as $(\Gamma\rho + \rho\Gamma)$. Neglecting relaxation, Eq. (5.2) reduces to

$$i \frac{d\rho}{dt} = [H, \rho] \quad (5.4)$$

Using Eqs. (5.3 and 5.4), we solve for the time evolution of the components of ρ and obtain the following density matrix equations for a two-level atom

$$\frac{d}{dt} \rho_{aa} = -\frac{i}{2} dE (\rho_{ab} - \rho_{ba}) \quad (5.5)$$

$$\frac{d}{dt} \rho_{bb} = \frac{i}{2} dE (\rho_{ab} - \rho_{ba}) \quad (5.6)$$

$$\frac{d}{dt}\hat{\rho}_{ab} = -\frac{i}{2}dE(\hat{\rho}_{aa} - \hat{\rho}_{bb}) - i\Delta\hat{\rho}_{ab} \quad (5.7)$$

$$\frac{d}{dt}\hat{\rho}_{ba} = \frac{i}{2}dE(\hat{\rho}_{aa} - \hat{\rho}_{bb}) + i\Delta\hat{\rho}_{ba} \quad (5.8)$$

where $\Delta = \omega_L - \omega_0$ is the detuning of the light field, and the following variables have been introduced to suppress explicit time-dependence of the coefficients in Eqs. (5.5-5.8),

$$\hat{\rho}_{ab} = \rho_{ab}e^{-i\omega_L t} \quad (5.9)$$

$$\hat{\rho}_{ba} = \rho_{ba}e^{i\omega_L t} \quad (5.10)$$

$$\hat{\rho}_{aa} = \rho_{aa}, \quad \hat{\rho}_{bb} = \rho_{bb} \quad (5.11)$$

Using the density matrix formalism, we can make an analogy to a spin vector in a magnetic field. First, we create a “pseudospin” or Bloch vector $\mathbf{p} = (u, v, w)$, where \mathbf{p} is written such that u, v , and w are the components of \mathbf{p} in the \hat{e}_x , \hat{e}_y , and \hat{e}_z directions, respectively. The variables u, v , and w are related to the elements of the density matrix by

$$u = \frac{1}{2}(\rho_{ab} + \rho_{ba}) \quad (5.12)$$

$$v = \frac{1}{2i}(\rho_{ab} - \rho_{ba}) \quad (5.13)$$

$$w = \frac{1}{2}(\rho_{bb} - \rho_{aa}) \quad (5.14)$$

To determine the time evolution of the Bloch vector, and thereby the time evolution of the density matrix elements, we introduce the vector

$$\mathbf{\Omega} \equiv (-dE, 0, -\Delta) \quad (5.15)$$

Analogous to a magnetic field's effect on a spin vector, $\mathbf{\Omega}$ produces a torque on $\mathbf{\rho}$ such that $\mathbf{\rho}$ precesses about $\mathbf{\Omega}$. The equation of motion of the Bloch vector, is given by

$$\frac{d}{dt} \mathbf{\rho} = \mathbf{\Omega} \times \mathbf{\rho} \quad (5.16)$$

and the precession frequency is

$$\Omega = \sqrt{(dE)^2 + \Delta^2} \quad (5.17)$$

where dE is called the Rabi frequency on resonance and $\Delta = \omega_L - \omega_0$ is the detuning of the light field frequency.

Solving for the time evolution of the Bloch vector components, we obtain what are known as the optical Bloch equations:

$$\dot{u} = \Delta v, \quad (5.18)$$

$$\dot{v} = -\Delta u + dEw, \quad (5.19)$$

$$w = -dEv. \quad (5.20)$$

Eqs.(5.18-5.20) and the normalization condition $\hat{\rho}_{aa} + \hat{\rho}_{bb} = 1$, are equivalent to the density matrix equations, Eqs.(5.5-5.8).

It should be noted here that this calculation does not model our physical system exactly. It does not take into account the longitudinal or transverse atomic velocity distribution; nor does it include the finite line width of the lasers and all levels.

5.2. “Split-step” method

In this section we give brief description of this method which we apply for calculation of the density matrix for 36 levels ^{85}Rb

In numerical analysis, the split-step method is a pseudo-spectral numerical method used to solve nonlinear partial differential equations like the nonlinear Schrödinger equation. The method relies on computing the solution in small steps, and treating the linear and the nonlinear steps separately (see below). It is necessary to Fourier transform back and forth because the linear step is made in the frequency domain while the nonlinear step is made in the time domain.

An example of usage of this method is in the field of light pulse propagation in optical fibers, where the interaction of linear and nonlinear mechanisms makes it difficult to find general analytical solutions.

In general, pseudospectral methods are faster by up to an order of magnitude, still achieving the same accuracy [71]. The pseudospectral method most commonly used for solving propagation problems in nonlinear dispersive media is the split-step Fourier method [72, 73], which has been used in this Thesis. In the following section, the basic aspects of the method will be covered.

5.2.1. Split-step Fourier method (SSFM)

Nonlinear Schrödinger Equation (NLSE) is written as:

$$\partial_z \Psi = -i \frac{\beta_2}{2} \partial_t^2 \Psi + i \gamma |\Psi|^2 \Psi$$

for the complex field Ψ which represent a wave and the nonlinear Schrödinger equation describe the propagation of the wave through a nonlinear medium. The second-order derivative represents the dispersion, while the γ term represents the nonlinearity.

The mathematical terms due dispersion and nonlinearity are separate and decoupled in the NLSE. It is this fact that allows the use of the SSFM for solving the NLSE. By looking at NLSE, the operators \hat{D} and \hat{N} can be written to correspond to the dispersive (and absorptive) and nonlinear terms respectively (ignoring the Raman effect),

The NLSE, can be rewritten in the rather simple form

$$\frac{\partial \Psi}{\partial z} = (\hat{D} + \hat{N})\Psi \quad (5.21)$$

\hat{D} is a differential operator, taking dispersive effects in a linear medium into account, while \hat{N} includes the nonlinear contributions:

$$\hat{D} = -\frac{\alpha}{2} - \sum_{m=2} \frac{i^{m-1}}{2^{m-1}} \beta_m \frac{\partial^m}{\partial t^m} \quad (5.22)$$

$$\hat{N} = i\gamma \left[|\Psi(z,t)|^2 + \frac{2I}{\omega_0 \Psi(z,t)} \frac{\partial}{\partial t} (|\Psi(z,t)|^2 \Psi(z,t)) \right] \quad (5.23)$$

$$\Psi(jh, t) = \exp[h(\hat{D} + \hat{N})] \Psi((j-1)h, t) \quad (5.24)$$

is a solution to the differential equation at step $z = jh$ (j is an integer). Note that the \hat{N} operator multiplies the field solution *and* is a function of the solution $\Psi(z, t)$. The \hat{D} operator is a differential operator expressed in terms of time derivatives that operate on $\Psi(z, t)$. To reduce the computational time, the operation of \hat{D} is performed in the frequency domain; this transforms the derivatives in the time domain to a multiplication in the frequency domain. After taking the Fourier transform of \hat{D} the multiplicative operator in the frequency domain is obtained,

$$\hat{D}(i\omega) \equiv F\{\hat{D}\} = F\left\{-\frac{\alpha}{2} - \sum_{m=2} \frac{i^{m-1}}{2^{m-1}} \beta_m \frac{\partial^m}{\partial t^m}\right\} = -\frac{\alpha}{2} - \sum_{m=2} \beta_m \frac{i^{m-1}}{2^{m-1}} (i\omega)^m \quad (5.25)$$

The SSFM is an iterative process that determines the field solution for spatial steps of h . This is performed step-by-step for the entire length of the fiber. The procedure during one step is illustrated in Figure 5.1. A dielectric medium of length L is broken into $s_L = L/h$ steps of length h . The field propagation solution $\Psi(jh, t)$ per spatial step h at the step $jh (j = 1, 2, \dots, s_L)$ for the entire length of fiber using relation

$$\Psi(jh, t) \approx F^{-1} \{ \exp(h\hat{D}(i\omega)) F \{ \exp(h\hat{N}) \Psi((j-1)h, t) \} \} \quad (5.26)$$

where $\Psi((j-1)h, t)$ is the field solution from the previous step and F and F^{-1} denote the Fourier transform and the inverse Fourier transform respectively. The approximation

$$\exp[h(\hat{D} + \hat{N})] \approx \exp[h\hat{D}] \exp[h\hat{N}] \quad (5.27)$$

is used in rewriting Eq. (5.24) to Eq. (5.26). The operation of \hat{N} occurs in the middle of the step and is the first operator to act on $\Psi(jh, t)$. The effect of dispersion is determined in the frequency domain. The field solution is Fourier transformed, operated on by \hat{D} and then back transformed to give the solution $\Psi(jh, t)$ at step jh .

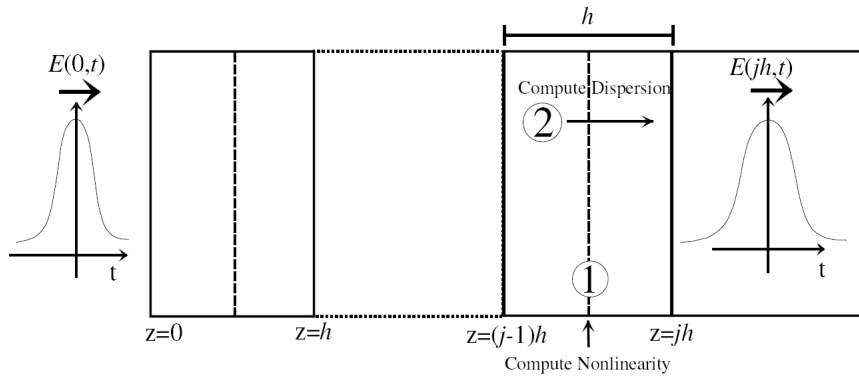


Figure 5.1 The SSFM for one iteration of step h starting at $z = (j-1)h$. The initial pulse $\Psi(0, t)$ enters the medium of length L . The length is broken into $s_L = L/h$ steps of length h .

The field solution at $z = jh$ is determined by:

1. Calculate the nonlinearity at step midpoint: $\exp(h\hat{N}(i\omega))\Psi((j-1)h, t)$
2. Calculate the dispersion over step in the frequency domain:

$$\{\exp(h\hat{D}(i\omega))F\{\exp(h\hat{N}(i\omega))\Psi((j-1)h, t)\}\}$$

Solution at

$$z = jh \Rightarrow \Psi(jh, t) \approx F^{-1}\{\exp(h\hat{D}(i\omega))F\{\exp(h\hat{N}(i\omega))\Psi((j-1)h, t)\}\}$$

3. Repeat iterations till $z = s_L h = L$, where L is the length of the fiber, for the final solution $\Psi(L, t)$.

Note that the form of field solution $\Psi(z, t)$ is in general complex so it contains both intensity and phase information. The computation speed of the SSFM is due to 1) calculating the dispersion in the frequency domain thus avoiding any numerical

derivatives, and 2) using the fast Fourier transforms to go between the frequency and time domains.

5.3 Density Matrix Calculation of Nonlinear Response Functions

Formally, the density matrix is defined using the outer product of the state of the system $|ket\rangle$ with its Hermitian conjugate $\langle bra|$

$$\hat{\rho}(t) = \sum_j P_j |\Psi_j(t)\rangle \langle \Psi_j(t)| \quad (5.28)$$

Eq.(5.28) describes a statistical ensemble (a mixed state) where the system has a probability P_j to be in the state $|\Psi_j\rangle$ with $\sum_j P_j = 1$. When $P_j = 1$ for one state and is zero, otherwise, the system is in a *pure state* (a state with maximum information) and can be described by a wave function [74]. Otherwise, we have a *mixed state* that may not be described by a single wave function. Adopting a basis set (φ_a) , we have

$$|\Psi_j(t)\rangle = \sum_a \alpha_{ja}(t) |\varphi_a\rangle \quad (5.29)$$

and the elements of the density matrix are given by

$$\rho_{ab}(t) = \sum_j P_j \langle \varphi_a | \Psi_j(t) \rangle \langle \Psi_j(t) | \varphi_b \rangle = \sum_j P_j \alpha_{ja} \alpha_{jb}^* \quad (5.30)$$

The diagonal element, ρ_{aa} represents the probability that the system is in the state $|\varphi_a\rangle$ (see Chapter 1, Section 1.3.3), i.e., the *population* of that state. The off-diagonal elements, ρ_{ab} , represent the phase relationship between $|\varphi_a\rangle$ and $|\varphi_b\rangle$ and are denoted as the *coherence* between these states.

The time evolution of the density matrix, $\hat{\rho}(t)$, can be calculated by solving the Liouville equation:

$$\frac{\partial \hat{\rho}(t)}{\partial t} = -\frac{i}{\hbar} [\hat{H}(r), \hat{\rho}(t)] - \hat{\gamma} \hat{\rho}(t) \quad (5.31)$$

where the square brackets represents the commutator. The Hamiltonian operator $\hat{H}(r)$ can be separated as $\hat{H}(r) = \hat{H}_0(r) + \hat{V}(r, t)$, where $\hat{H}_0(r)$ is the unperturbed Hamiltonian and $\hat{V}(r, t) = -\hat{\mu} \cdot E(r, t)$ is the interaction with the external electric field (r is the spatial coordinate of the sample), and $\hat{\mu}$ the coupling operator, $\hat{\gamma}$ is the relaxation superoperator [75, 76]

Chapter 6 Mechanisms of Holography Recording in Rubidium Vapor Close to Resonance

6.1 Introduction

Here we investigate the use of rubidium as holographic material, and discuss two principal mechanisms of holographic writing. The first is based on absorption grating writing. In [77] was investigated experimentally another grating formation mechanism based on Faraday rotation. It is promising for applications because it gives phase holograms with higher diffraction efficiency. There are developed the theory for both cases. The experimental part of this thesis in some points is closely related to the Ref.[77] and we will refer to it where appropriate.

The outline of this chapter of thesis follows. First, we describe the most important components of our experiment and characterized them. Second, we describe the computer model and results for intensity-dependent absorption and optical activity for uniform illumination. Next, experimental measurements of absorption and optical rotation are reported and compared with the theory. The experiments with absorption and phase gratings are described. The last sections are discussion and conclusions.

6.2 Experimental set-up

6.2.1 Tunable semiconductor laser

The StableWave/Vortex laser is an external-cavity diode laser (ECDL) based on the Littman-Metcalf design, it is operated in the wavelength range at 765–781 nm and maximum power is 50 mW. The customer-selected wavelength is set and stabilized at the factory using external optics; a diffraction grating, a mirror, and precision temperature control (see Figure 6.1). Fine wavelength tuning without

mode hops is achieved by rotating the mirror around a fixed rotation point using a piezo-electric actuator.

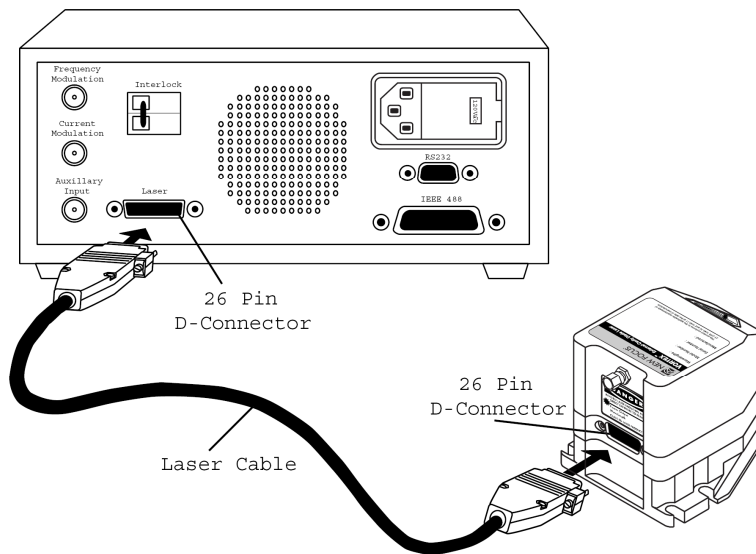


Figure 6.1 Laser System Details [78]

Laser output power is controlled by an ultra-low-noise current source. The controller contains the electronics for laser-current, laser-temperature, and piezo-voltage control, as well as digital-interface electronics. The temperature of the laser cavity, the laser current controls the optical output power and the piezo voltage controls the laser wavelength (frequency) can be adjusted through the front-panel controls, the computer interface, or the back-panel BNC connectors. The output wavelength is strongly dependent on the temperature of the laser cavity, which is actively stabilized using a thermoelectric cooler. The total piezo voltage is limited to a range of 0 to 117.5 V.

6.2.2 General Theory

In an ECDL, the optical feedback provided by an external frequency-selective element is coupled back into the diode cavity. This condition brings a number of important advantages. The diode can be forced to oscillate on a specific single mode (locking), reducing drastically the power distributed on the other modes. It can be tuned, varying the feedback frequency, over a wavelength range that is usually wider than that achievable by temperature and current tuning.

The StableWave/Vortex laser cavity is based on the Littman-Metcalf design [79-83], which uses a diffraction grating at grazing incidence to provide wavelength selectivity. The first diffracted order is sent to a mirror, which reflects it back into the diode. The external cavity is thus formed between the diode rear facet and the mirror, whose angle can be varied to change the wavelength of the feedback and tune the diode. The specular reflection or zero-order diffraction off the grating serves as the output beam of the laser.

The angle between the grating and the end mirror determines the lasing wavelength. Tuning is achieved by varying the angle using a piezoelectric actuator to rotate the end mirror. Continuous (mode-hop-free) tuning requires selecting an appropriate rotation point. Discontinuous tuning characterized by periodic “mode-hops” results from two competing wavelength-selection constraints: the mirror-grating angle and the laser-cavity length. The laser-cavity length, L , defines a discrete set of possible wavelengths or *modes*, λ_N , that can lase, given by the equation $L = N\lambda_N / 2$, ($N = \text{integer}$). The grating equation insists

that $\lambda = \Lambda(\sin \theta_i + \sin \theta_d)$, where Λ refers to the groove spacing of the grating while θ_i and θ_d refer to the incident and diffracted angles of the laser beam. Rotation of the end mirror causes parameters in both equations to change. An appropriately selected point of rotation synchronizes the two, such that the cavity length remains the same number of half-wavelengths long as the mirror is being rotated. Thus mode-hop free tuning is achieved. When this condition is not met, the lasing

wavelength will periodically hop from one mode to the next (e.g. from N to $N + 1$) as the laser is tuned.

The laser wavelength is affected by the current through the diode. Changing the diode current affects the refractive index of the diode lasers and therefore, the laser cavity length. The magnitude of the effect is diode dependent, but is typically $25 - 150 \text{ MHz} / \text{mA}$.

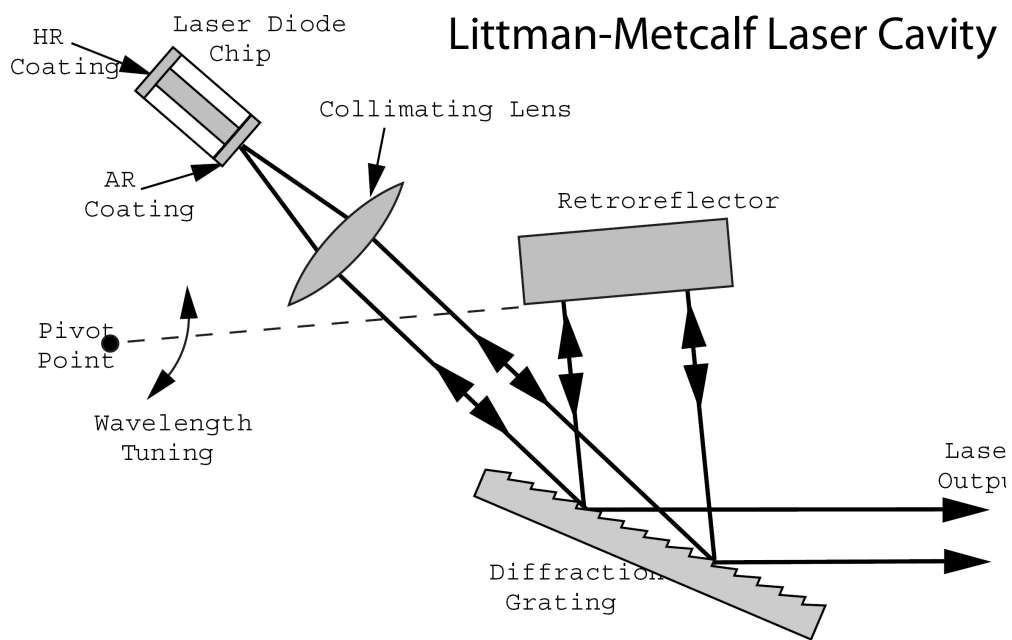


Figure 6.2 Scheme of a system in Littman configuration, taken from New Focus [78]

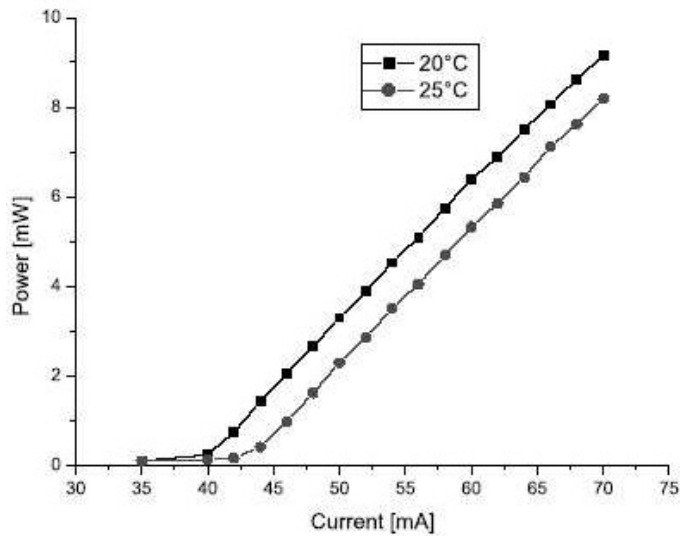


Figure 6.3 Output power vs injection current curve at two different temperatures

6.2.3 Acousto-optical modulator

Acousto-optical modulators are used for several purposes: as frequency shifters, modulators or fast shutters. The principle of operation is simply based on a crystal whose index of refraction changes sharply with density. When a high-power acoustic wave is sent to the crystal, it travels through it as a longitudinal sound wave creating regions of high and low density. This turns the crystal effectively into a diffraction grating. This is the effect which leads to the diffraction pattern that we observe when we send light through the crystal. The key difference being that since the diffraction grating itself is moving at sound velocity, the diffraction orders are also frequency shifted. The zeroth order is unaffected by the frequency of the acoustic wave, while the different orders of diffraction are frequency shifted, and their angular separation (understandably) varies as the frequency of the input acoustic wave.

The frequency difference produced by a standard AOM is $\Delta\Omega = 50 \div 150\text{MHz}$

6.2.4 Lock-in

In the experiment we used Lock-in amplifier, Model SR 510. The Lock-in technique is used to detect and measure very small ac signals. A Lock-in amplifier can make accurate measurements of small signals even when the signals are obscured by noise sources which may be a thousand times larger.

Essentially, a lock-in is a filter with an arbitrarily narrow bandwidth which is tuned to the frequency of the signal. Such a filter will reject most unwanted noise to allow the signal to be measured. A typical lock-in application may require a center frequency of 10 KHz and a bandwidth of 0.01 Hz. This 'filter' has a Q of 10^6 - well beyond the capabilities of passive electronic filters.

In addition to filtering, a lock-in also provides gain. For example, a 10 nanovolt signal can be amplified to produce a 10 V output--a gain of one billion.

A basic principle is next.

The received signal is amplified and digitized. It is divided into two separate channels, the signal is multiplied by the reference signal (with frequency ω_{ref}) and the 90° phase-shifted reference signal respectively. The reference signal is generated with the lock-in digital oscillator. An additional implemented phase displacement enables to compensate phase differences caused by the measuring equipment. After multiplication, the resulting signals are low-pass filtered and provide now information about the real part and the imaginary part of the analyzed signal relating to the phase position of the reference signal. Out of them the amplitude as well as the relative phase shift is calculated.

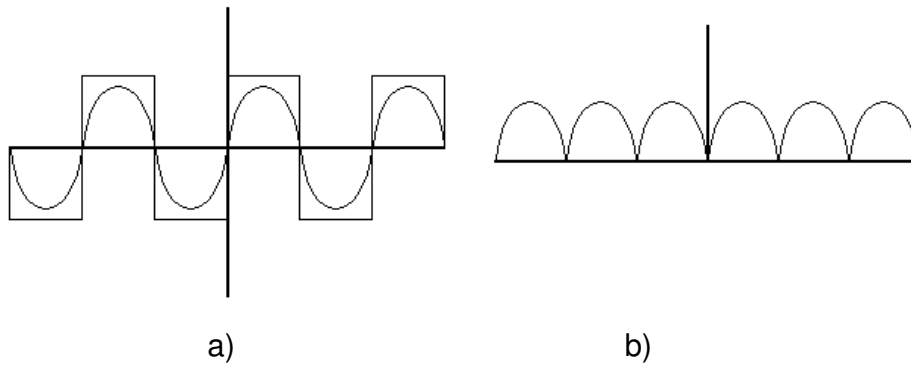


Figure 6.4: a) input (sinusoidal) and reference (square) signal, b) result of the multiplication of the input signal and reference, the signal (b) is integrated (averaged) with a large time constant

6.3 Scheme of the Experiment 1.

In the experiment 1 we used 50 mm long, 2.5 cm diameter rubidium cell. It was placed inside a solenoid, and protected from the geomagnetic field with two concentric cylindrical shells made from alloy with high magnetic permeability. The estimation of residual field based on small-field features in absorption curves, gives values $\sim 0.02G$ for residual longitudinal component. The electric heater used to control the temperature was made with twisted pair and placed outside of the first protective layer to reduce the influence of the magnetic field of a heater. The cell was locally cooled with weak air flow to prevent rubidium deposition on windows. The elliptical laser beam of tunable semiconductor laser ($< 50mW$, 780.24 nm wavelength, see section 6.2.2) was expanded with telescopic lens system to approximately $3 \times 5mm$ size. The quarter-wave plate and polarizer served for polarization control. Tunable semiconductor laser was connected to both a current and a temperature control device to adjust the wavelength of the laser. The laser beam passed through AOM1, then through a mirror M1. Approximately 10% of the beam was reflected off the front face of the mirror M1 to mirror M2, AOM2, and finally reflected off the mirror M3 and passed through the rubidium cell on to a photo-diode. This beam was the probe beam for the experiment. The other 90% of the beam passed through the AOM1 and passed through the rubidium cell in the

co-direction of the 10% beam. The 90% beam was the pump beam for the experiment. They are interact inside the rubidium cell, and a diffracted beam appear, which we are detecting in a photo-diode, which was connected to an oscilloscope, where the output signal could be monitored. (Fig. 6.5)

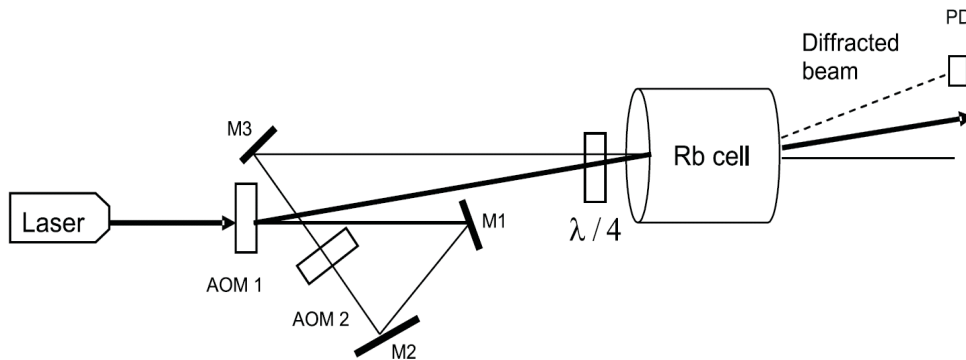


Figure 6.5 Experimental setup. AOM 1,2 -acousto-optical modulators; M1-M3 –mirrors; PD - photodetector. The angle between writing beams is exaggerated for better visibility. The second modulator produces the frequency-shifted beam slightly above the picture plane.

Two acousto-optical modulators (AOM), one fixed at $80MHz$ frequency, and another tuned between $65MHz$ and $95MHz$ were used to shift the frequency of a signal wave in $\pm 15MHz$ interval with respect to the reference. A reference beam, and weaker signal were crossing inside the cell at an angle $2.6 \pm 0.3mrad$. The intensity ratio 10:1 was kept frequency-independent by adjusting high frequency signal to signal beam modulator. Applying amplitude modulation to the AOM, we could switch the signal beam on and off with characteristic time $100 - 200ns$, determined by the beam width.

6.4 Scheme of the Experiment 2

For the experiment 2 we used 25mm long rubidium cell placed inside a solenoid. The measurements were made at room temperature (21°C). The magnetic shield made of high permeability metal was used to avoid geomagnetic influence. The rectangular wave voltage from the generator was applied to the solenoid; magnetic field was switched between B and $-B$ with a frequency $10\text{--}20\text{Hz}$. The scheme of experiment 2 is on Figure 6.6.

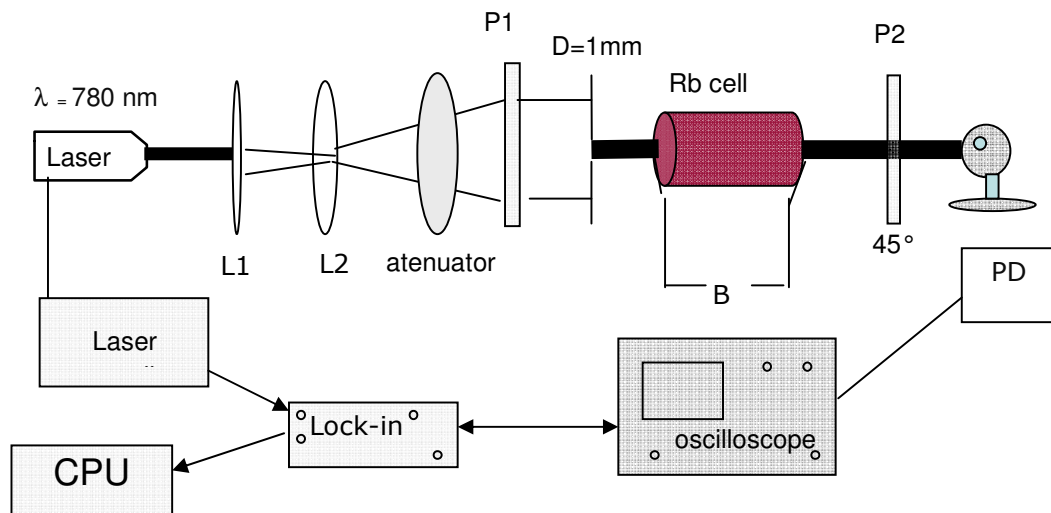


Figure 6.6 Experimental set-up 2. L1 and L2 a telescopic lenses, P1, P2 are polarizers, PD - photodetector with a small aperture, B - magnetic field

This relatively low frequency was taken to diminish the influence of the transition process on the results of measurement. The beam of tunable semiconductor laser with plane output polarization was expanded to approximately $5 \times 8\text{mm}$ size by a telescopic lens system. The 1mm diameter aperture in front of the cell was

producing a circular beam with close to uniform intensity distribution. The photodetector with a small aperture in the center of the beam was placed after the 45° tilted polarizer. The Lock-in amplifier was connected to the photodetector output. The laser frequency was scanned by steps across the line, and the Lock-in output was monitored by a computer. The Lock-in output signal is directly proportional to Faraday rotation magnitude. Absorption is also affected by the magnetic field, but from symmetry arguments it follows that the absorption in our geometry does not change, when the magnetic field changes the sign, thus no signals due to absorption are detected by the Lock-in. We checked this experimentally by measuring the Lock-in signal without the polarizer in front of the photodetector. The magnetic field induced circular dichroism is also present, but for small changes in polarization state it does not manifest itself for our setup. It can be measured by placing quarter-wave plate in front of the polarizer, and has the magnitude comparable to that one for optical rotation.

The results of experiment are presented in section 6.6.

6.5 The computer model for ^{87}Rb , description

The microscopic description of hologram formation starting from basic principles can be done for rubidium, but adequate theory is complex because of the big number of sublevels involved (Fig.6.7, also see chapter 1 of this thesis). At resonance, complicated polarization behavior emerges, and geomagnetic field can radically change the observed polarization properties and diffraction efficiency. The strong dependence on the time of transit is also observed. In particular, the measured light absorption for $F_g = 1$ in $D2$ ^{87}Rb transition is affected by a beam diameter (see Figure 6.8). There is little hope that tractable analytical solution can account for all these factors. The theory for resonant case, as far as we know, was not developed in detail.

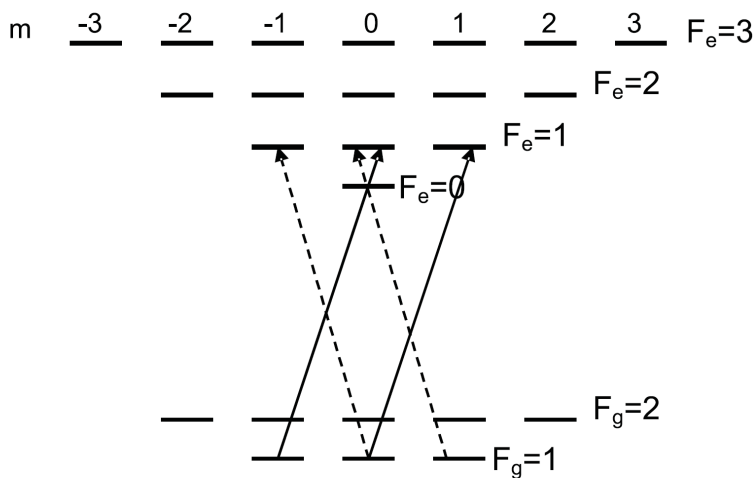


Fig. 6.7. The sublevels structure for ^{87}Rb D2 line. Numbers -3...3 are momentum projections on quantization on z-axis, m_F . Energy differences between levels are not to scale. As an example, the transitions induced by right (solid arrows) and left circular polarizations (dashed arrows) between $F_g = 1$ and $F_e = 1$ levels are shown.

We study a realistic computer model based on density matrix formalism. The number of participating sublevels for our experimental conditions is up to 15, which means solving up to 225 coupled linear differential equations for matrix elements. Additionally, integration with respect to detuning is needed to account for Doppler broadening. The temporal evolution of the matrix is calculated, which permits to include important effects of transit. The task is implemented in acceptable time (minutes to hours) with a special code written in C.

The full solution gives a highly detailed description, including sublevel population dynamics, and relative importance of different F-levels for particular process. Though the model is quite involved, good agreement with the experiment makes it a useful guide. In some cases, simplified approximations can be derived.

For reasons of computation complexity we investigate only one of two naturally present isotopes, ^{87}Rb which have smaller number of sublevels. This isotope produces more efficient gratings for the conditions of earlier experimental work [77]. The structure of transitions for the isotope is depicted in Fig.6.7 (also see Chapter 1). The ground level is split in two hyperfine components with $F_g = 1$ and $F_g = 2$ full momentum, separated by 6.83GHz . These levels in presence of magnetic field are further subdivided in 3 and 5 Zeeman components respectively with $m_F = -F, \dots, F$. The excited manifold consists of four hyperfine levels with $F_e = 0, 1, 2, 3$.

These levels also have Zeeman sublevels according to their F number. The hyperfine splitting between upper levels are 72MHz , 157MHz and 267MHz (Section 1.5 and 1.6). As the characteristic Doppler broadening is 0.5GHz , the transitions within upper manifold are not resolved, and the experimentally observed absorption spectrum has two lines with $\approx 7\text{GHz}$ separation. Detailed review of spectroscopic data for ^{87}Rb can be found in the online reference [15].

To simplify the problem, we normally assume, that the light of given frequency interacts only with the closest F-level of the upper manifold of an atom with a definite Doppler shift. This assumption breaks for $F_g = 1$ line at the high end of experimentally investigated intensities $5 - 30\text{mW}/\text{cm}^2$, where the light of given frequency can interact simultaneously with two close levels $F_e = 0$ and $F_e = 1$. The situation manifests itself in one upper level model when the width of characteristic spectral features becomes comparable to $F_e = 0$ and $F_e = 1$ frequency difference 72.2MHz . For even higher intensities, all three upper levels of permitted transition are necessary. Though our software can handle the complete task, the solution substantially slows down. Thus we consider independent interaction with all F_e levels, with the exception of the transition $F_g = 1, F_e = 0, 1$ which is treated separately. For the ground manifold, both $F_g = 1$, and $F_g = 2$ sublevels have to be

taken into account, because excitation with light combined with the spontaneous emission from upper transition level induces population transfer between them. These approximations prove to be adequate for not very high intensities, which are typical for holographic writing.

We take the master equation for atomic density matrix ρ in presence of spontaneous emission in a form [83, 84]:

$$\frac{\partial \rho}{\partial t} = (i/\hbar)[\rho, H] + \sum_{q=-1,0,1} C_q \rho C_q^+ - \frac{1}{2}(C_q^+ C_q \rho + \rho C_q^+ C_q) \quad (6.4)$$

Here H is the Hamiltonian of the isolated atom, and C_q, C_q^+ are lowering and raising operators for the multilevel atom. The z-axis for quantization is chosen along the wave propagation direction, and parallel to the magnetic field. All operators ρ, H, C_q, C_q^+ are $N \times N$ matrices, with N a total sublevel number. The Hamiltonian is taken in dipole approximation, it has diagonal elements equal to state energies, and off-diagonal elements are proportional to left- and right-circularly polarized components of the electric field of the wave. These elements couple states with $F_e - F_g = 0, \pm 1$, and $m_{F_e} - m_{F_g} = \pm 1$, and they are proportional to dipole moments for a given transition.

The terms under the sum in the right-hand side describe spontaneous emission.

Operators C_q, C_q^+ , are proportional to the atomic dipole operator:

$$C_q^+ |F_g, m_{F_g}\rangle \geq \Gamma^{1/2} (1, F_g, q, m_{F_g}; F_e, m_{F_e} = m_{F_g} + q) |F_e, m_{F_e} = m_{F_g} + q\rangle, \quad (6.5)$$

$$C_q^+ |F_e, m_{F_e}\rangle \geq 0 \quad (6.6)$$

$$C_q = (C_q^+)^*, \quad (6.7)$$

with decay rate Γ , and Clebsch-Gordan coefficients for coupling ground and excited states sublevels.

The standard rotating wave approximation is used to eliminate time-dependent expressions in the Hamiltonian. The dipole moments for transitions are calculated according to the expressions of Ref. [15].

The Eq. (6.4) is solved numerically. It has the form

$$\frac{\partial \rho}{\partial t} = \Lambda(\rho), \quad (6.8)$$

Where $\Lambda(\rho)$ is linear, time independent operator acting on elements of the matrix ρ (it is represented by $N^2 \times N^2$ matrix, which is applied to N^2 -dimensional vector ρ , and cannot be reduced to a multiplication of ρ as $N \times N$ matrix by another $N \times N$ matrix.) The formal solution is given by:

$$\rho(t + \Delta t) = \exp(\Lambda \Delta t)(\rho(t)), \quad (6.9)$$

with an operator exponent. The numerical solution proceeds as calculation of the operator exponent with the Taylor series, and consequent application of it to $\rho(0), \rho(\Delta t), \dots$ etc. Since Λ is time-independent, the operator exponent for a given set of parameters is calculated only once. This method of solution works well up to $N \approx 18 - 20$, but the calculation time grows rapidly with N , because matrix exponent calculation time scales as N^6 , and there rest of the algorithm implementation scales as N^4 . We also have implemented another solution algorithm more efficient for big N . It is described below.

The initial condition is equal population distribution among N_g ground sublevels $\rho_{ii} = 1/N_g$, for $1 \leq i \leq N_g$ and all other density matrix elements are zero.

The time-dependent complex polarization of a medium for right/left circular polarization is obtained with a trace of dipole operator $P(t) = Tr(C_q \rho)$, $q = \pm 1$. The real and imaginary parts of polarization after dividing by field amplitude give

absorption coefficient and phase shift per unit length for right and left-polarized circular components. The result is averaged over time, necessary according to Maxwell distribution for the atom to arrive to the center of circular beam with radius l_0 :

$$P_a = \int_0^\infty P(t) \frac{\tau^2}{t^3} \exp(-\tau^2 / t^2) dt \quad (6.10)$$

and characteristic time

$$\tau = l_0 \sqrt{\frac{M}{2k_B T}} \quad (6.11)$$

with M atomic mass, and $k_B T$ Boltzmann constant and temperature product.

One more averaging, over different Doppler-shifted groups of atoms is performed to obtain absorption and refraction values measured in the experiment. We are interested in values close to the center of the absorption line, thus to the first approximation we assume here, that all velocity groups of atoms have equal concentrations. By doing this, we do not consider effects, which are produced at the line edges, though such effects can be important for higher temperatures.

6.6 The computer model, comparison of the experimental results with theory for ^{87}Rb

From a macroscopic point of view, the changes in light intensity and polarization state affect medium absorption coefficient and refractive index. If the vapor is illuminated with two coherent beams, the medium parameters vary in space

according to local changes in polarization or/and intensity. This produces a holographic grating, which can be detected by diffraction of beams. The information on local illumination is recorded in the atomic medium either in the form of sublevel populations, which are given by diagonal elements of density matrix, or in the form of quantum coherences, given by the matrix off-diagonal elements. Long-living coherences between lower levels can be induced by light of single frequency if both circular polarizations are present, in particular, for linear polarization.

First, we discuss the case of strictly circular polarization of incident beams, for which coherences between lower levels are absent. In this case, for the center of the line the grating is of absorption type. Thus, to estimate diffraction it is sufficient to calculate absorption as a function of light intensity. These dependences (Fig.6.8) are qualitatively different for $F_g = 2$ and $F_g = 1$ transition lines. For the transition with $F_g = 2$, the absorption for big intensities I behaves approximately as $(1 + I/I_{sat})^{-1/2}$, (I_{sat} is the saturation intensity close to $1 - 3mW/cm^2$), and it is relatively independent on the probing beam diameter (time of transit). Such behavior follows from simple two-level model [85]. It is explained by noting, that the transition from $F_e = 3$ to $F_g = 1$ is forbidden in dipole approximation, thus the atom with the excited $F_g = 2$ to $F_e = 3$ transition after some illumination time arrives to the isolated state with $m_{F_g} = \pm 2, m_{F_e} = \pm 3$, for right(left) circular polarization, and the

atom behaves essentially as having only two levels.

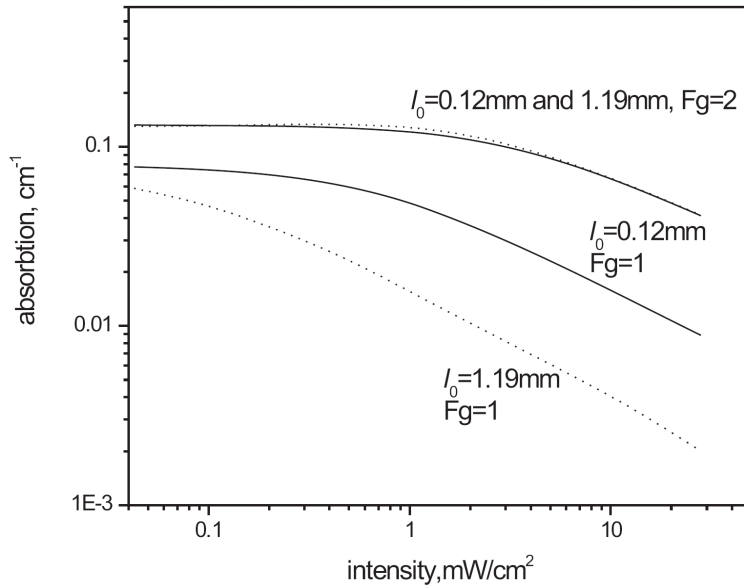


Fig. 6.8 Absorption calculation for circularly polarized light as function of intensity for $F_g = 1$ and $F_g = 2$ lines in the center of circular beam with uniform intensity distribution and radius $l_0 = 0.12\text{mm}$ (solid) and $l_0 = 1.19\text{mm}$ (dots). The calculation is made for natural Rb at temperature 30°C using data of Ref.[15].

For the transition with $F_g = 1$, making beam diameter bigger noticeably reduces the absorption, and the characteristic saturation intensity is much smaller, than for the $F_g = 2$ transition. The absorption diminishes with intensity faster than $I^{-1/2}$. This occurs because the light-induced transitions from $F_g = 1$ to $F_e = 2$ transfer the population to the "unseen" level $F_g = 2$ as a result of spontaneous emission. The isolated from $F_g = 2$ level lambda-transition $F_g = 1$ to $F_e = 0$ under circular polarization accumulates atoms in a state, which is also non-absorbing for this particular circular polarization. For transition $F_g = 1$ to $F_e = 1$, the combination of

above mentioned factors works -the population is partly transferred to $m_F = \pm 1$ state, and partly to $F_g = 2$ states. Thus, the absorption seen for $F_g = 1$ line is a result of transient process, and critically depends on the atoms which enter the beam from outside (the collisions inside a beam can be neglected because of low concentration of atoms). The time of $F_g = 1$ depopulation for small intensity becomes bigger, than the transit time, thus the absorption for small intensity tends to a constant value, which does not depend on beam diameter.

The different characters of saturation produce marked differences in diffraction efficiency for absorption gratings in $F_g = 2$ and $F_g = 1$ lines. In the $F_g = 2$ case, the measured dependence of transmission on light intensity gives good estimation for diffraction efficiency. At the $F_g = 1$ transition, the width of beam becomes important: close to the interference pattern center the atoms becomes "transparent", they do not respond to local changes in illumination and the diffraction efficiency are quite poor there.

The transition from $F_g = 1$ becomes much more efficient for holography, if quantum coherence effects, which arise for non-circular polarizations, are included, and weak magnetic field is applied.

With a linearly polarized light, which is a superposition of right and left circular polarizations, the dark state is formed [86]. For zero detuning of both fields, the population of the upper level becomes zero, and wavefunctions for lower levels have fixed phase difference. The coherent state is destroyed with small frequency detunings induced by magnetic field. Because of this, sharp spectral features appear. The magnetic field splits Zeeman sublevels, this produces differences in propagation speeds for right and left-polarized components, and the polarization plane rotates (nonlinear Faraday rotation [87]). The rotation mechanism is illustrated in Fig.6.9 for $F_g = 1$, $F_e = 0$ transition.

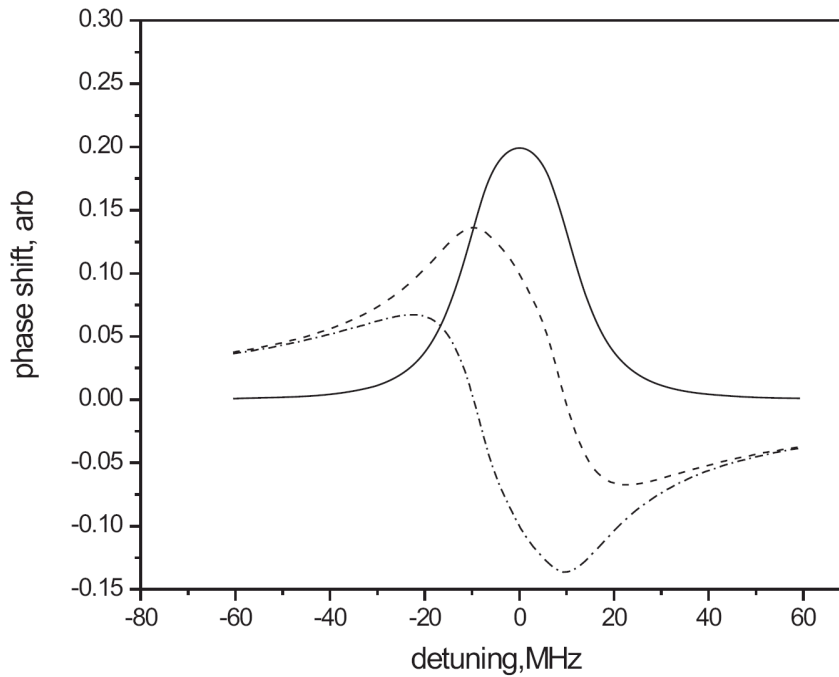


Figure 6.9 Faraday rotation for $F_g = 1$, $F_e = 0$ transition. The numeric example shows that for nonzero magnetic field refractive indexes for left (dash) and right circular polarizations (dash-dot) have different dependences on detuning from transition frequency. The difference (solid line) does not disappear if integrated with respect to detuning, thus this mechanism is important for Doppler broadened line. Light intensity $2.13 mW/cm^2$, magnetic field $0.12 G$, beam radius $l_0 = 1.19 mm$.

The calculated rotation angle as a function of magnetic field for different light intensities is presented in Figure 6.10. The behavior is dominated here by two lambda-systems formed in $F_e = 0$ and $F_e = 1$ transitions. For big intensities, the simultaneous interaction of light with both $F_e = 0$ and $F_e = 1$ levels produces diminishing of the rotation signal in comparison with independent level approximation. The difference between two calculation methods is around 1% for $0.2 mW/cm^2$ intensity, $\sim 10\%$ for $2 mW/cm^2$ intensity, and grows to significant 30%

for $20mW/cm^2$.

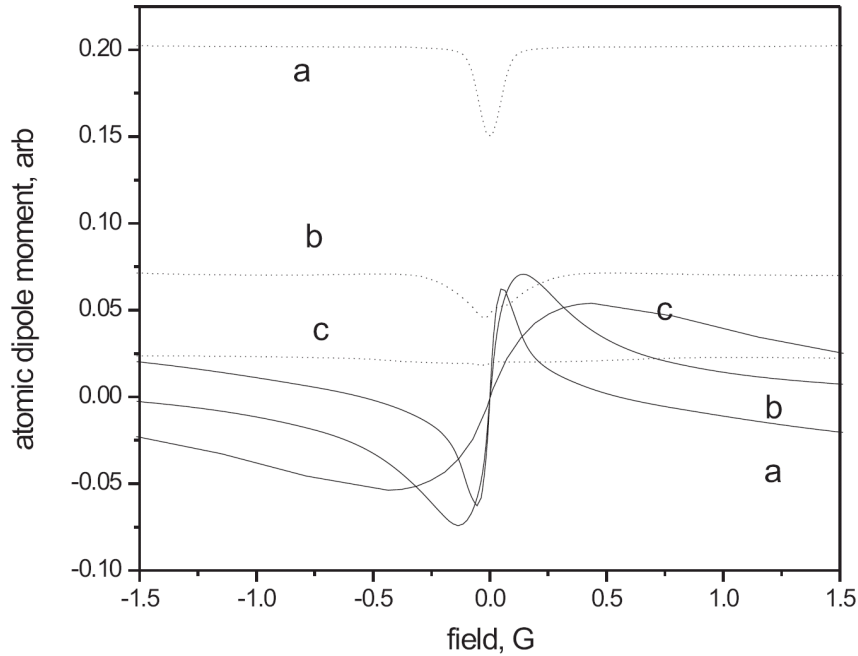


Figure 6.10 Real and imaginary parts of calculated dipole moment divided by field amplitude, which are proportional to optical activity (solid) and absorption (dots) vs magnetic field for different light intensities in $F_g = 1$ line. Intensities are: a) $0.216mW/cm^2$, b) $2.13mW/cm^2$, c) $19.2mW/cm^2$, the beam radius is $l_0 = 1.19mm$.

The independent levels model does not give the experimentally observed drop in maximal possible rotation angle for higher intensities; it gives, that the maximal rotation angle is approximately the same for 20 and $2mW/cm^2$ instead.

For $F_g = 2$ line, the most important transition is to $F_e = 3$, which is isolated from $F_g = 1$. The character of rotation for $F_g = 2$ line is different, than for $F_g = 1$. The maximal rotation angle grows here with intensity in the entire investigated intensity interval (Figure 6.11).

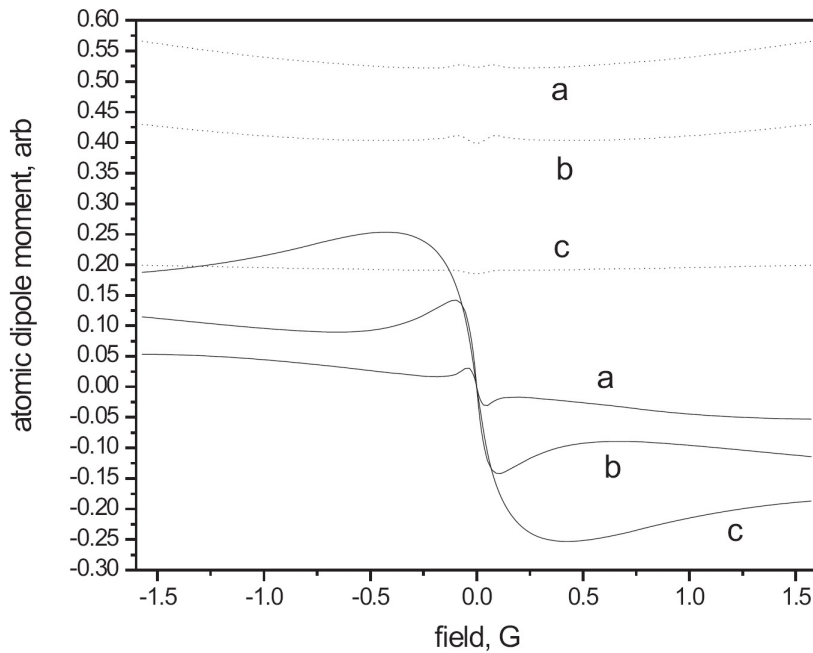


Figure 6.11 The same, as in Figure 6.10, but for $F_g = 2$ line.

The polarization rotation is basically the change in the refractive index. Because of the nature of coherent state, the absorption of atom in this state is reduced (light induced transparency). For zero magnetic field the rotation is zero, but for small magnetic fields and polarization close to a linear one, enhanced Kerr nonlinearity can be expected [7]. The growth in the intensity makes the rotation to absorption ratio bigger, which produces more pronounced phase hologram. It is also interesting to look at the absorption for linear polarization as a function of magnetic field B . Here, the characteristic behavior is also different for $F_g = 1$ and $F_g = 2$ transitions. For $F_g = 1$, coherence effects produce narrow spike in transmission at a magnetic field close to zero. At $F_g = 2$, the spike is much wider, and it has fine structure for small B .

6.7 Direct multi-level density matrix calculation of nonlinear optical rotation spectra for up to 36 levels, in ^{85}Rb

The established method of theoretical description of rubidium transition (see in Section 6.3) is the master equation for atomic density matrix [83, 84, 88], but for big number of sublevels the calculations become very time-consuming. Since the steady state is not attained for open transitions during the time of transit, for realistic calculations it is highly desirable to take into account the whole temporal evolution of atomic parameters.

Instead of solving for full evolution it is possible to introduce an effective repopulation for lower levels and to take an effective steady state. This simplifies the solution, but the repopulation parameters are not obtained directly, and have to be fixed according to experiment [88]. We use the direct numerical method, which produces rapid enough solution of complete dynamics for master equation for multi-level rubidium atom. Such solution does not contain free parameters. The calculation principle is similar to the split-step algorithm (see chapter 5) widely used for modeling the nonlinear propagation in media with Kerr-type nonlinearity, optical fibers in particular [89].

We take the same equations (6.4)

The combination

$$P = \sum_{q=-1,0,1} C_q^+ C_q \quad (6.12)$$

is a projector operator, its matrix has only diagonal elements $P_{kk} = P_k$.

The number of independent unknown real parameters in ρ is $N^2 - 1$, (N is the number of sublevels). For ^{87}Rb D_2 transition (780.24nm), $N = 24$, and it is necessary to solve a system of 575 coupled differential equations. For ^{85}Rb , there

are 36 sublevels, with 1295 equations. One characteristic time of this system is the lifetime Γ^{-1} . There is also a characteristic time of inverse Doppler broadening (comparable to the inverse detuning and to the inverse frequency difference between upper levels), which is 10-100 times smaller, and the time of flight of atom through the beam, which is 10-100 times bigger. Thus, the equations, apart from a big number of variables, have quite different time scales, and conventional algorithms for ODE solution, such as Runge-Kutta, are slow and can become unstable. Additionally, averaging over Doppler-shifted groups of atoms is needed, and the system has to be solved hundreds of times for comparison with the experiment.

For solution, we note that formally the Eq.(6.4) is equivalent to

$$\frac{\partial \rho}{\partial t} = (\mathbf{A} + \mathbf{B}) \rho, \quad (6.13)$$

where \mathbf{A} , \mathbf{B} are superoperators corresponding to Hamiltonian and relaxation parts respectively. They are expressed by $N^2 \times N^2$ matrices which act on the elements of ρ treated as N^2 vector. The formal solution of Eq.(6.13) is given by operator exponent:

$$\rho(t + \Delta t) = \exp((\mathbf{A} + \mathbf{B}) \Delta t) \rho(t) \quad (6.14)$$

If each of two superoperators is treated separately, fast algorithms of calculation exist for both of them. We can more easily calculate $\exp(\mathbf{A} \Delta t)$ and $\exp(\mathbf{B} \Delta t)$, than $\exp((\mathbf{A} + \mathbf{B}) \Delta t)$.

For rotating wave approximation, when the Hamiltonian is time-independent, and there is no spontaneous emission, the Hamiltonian part of evolution is given by

$$\rho(t + \Delta t) = U(\Delta t)\rho(t)U^{-1}(\Delta t) \quad (6.15)$$

with the unitary matrix $U(\Delta t) = \exp(-i\frac{H}{\hbar}\Delta t)$

The relaxation part of evolution with zero Hamiltonian is calculated with:

$$\rho(t + \Delta t) = \exp(-P\Delta t/2)\rho(t)\exp(-P\Delta t/2) + \sum_{q=-1,0,1} C_q Q(t + \Delta t) C_q^+ \quad (6.16)$$

and elements of Q matrix are:

$$Q_{ik}(t + \Delta t) = 2\rho_{ik}(t)(1 - \exp(-(P_i + P_k)\Delta t/2))(P_i + P_k)^{-1} \quad (6.17)$$

if $P_i + P_k \neq 0$, and $Q_{ik} = 0$ if $P_i + P_k = 0$. The derivation of Eq.(6.16) is next:

We start with the equation

$$\partial_t \rho = -\frac{1}{2}(P\rho + \rho P) + \sum_{q=-1,0,1} C_q \rho C_q^+$$

Using this, and relations for raising and lowering operators $C_q C_s = C_q^+ C_s^+ = 0$ and

$P C_q = C_q^+ P = 0$ the second derivative of ρ is:

$$\partial_t^2 \rho = \frac{1}{4}(P^2 \rho + 2P\rho P + \rho P^2) - \frac{1}{2} \sum_{q=-1,0,1} C_q (P\rho + \rho P) C_q^+$$

Consequent calculation of derivatives and application of Taylor series

$$\rho(t + \Delta t) = \rho(t) + \partial_t \rho(t)(\Delta t) + \frac{\partial_t^2 \rho(t)}{2!} (\Delta t)^2 \dots$$

gives, after collecting the terms, the Eq.(6.16).

Of course, the two operator exponents do not commute, and though the two solutions given by Eqs.(6.15,6.16) are exact, their combination is not. Nevertheless, if the time Δt is small enough, we can obtain close approximation to the exact solution by applying one matrix exponent after another.

As for the nonlinear propagation split-step, better exactitude is obtained if relaxation evolution is calculated at the middle of time interval between two calculations of Hamiltonian part. It follows from the equation for linear operators:

$$\exp((\mathbf{A}+\mathbf{B}) 2\Delta t) = \exp(\mathbf{A} \Delta t) \exp(\mathbf{B} 2\Delta t) \exp(\mathbf{A} \Delta t) + \mathcal{O}((\Delta t)^3), \quad (6.18)$$

which is related to Baker-Campbell-Hausdorff formula. If we approximate the exponent of a sum by a simpler expression

$$\exp((\mathbf{A}+\mathbf{B}) 2\Delta t) = \exp(\mathbf{A} 2\Delta t) \exp(\mathbf{B} 2\Delta t) + \mathcal{O}((\Delta t)^2) \quad (6.19)$$

the accuracy is worse.

Since the Hamiltonian is time-independent in rotating wave approximation, the matrix exponents U, U^{-1} are calculated only once with Taylor series, and applied consequently. The overall computation time is proportional to N^3 .

From physical arguments, if we are interested in evolution over periods of time much bigger than the relaxation time, the step Δt can be safely taken to resolve only the relaxation time Γ^{-1} . This conjecture was checked for the problem of interest by comparing the solution with the exact one and by comparing solutions with different Δt . Practically, we were keeping Δt at approximately $0.1 \Gamma^{-1}$.

We have implemented the split-step algorithm in C programming language. The calculation of superoperator exponent with high exactitude for limited number of sublevels was made earlier (see section 6.5), and we used it for testing the program mathematics.

The Hamiltonian and general data on transition were taken from the online reference [90]. Our previous calculations (section 6.5) were made in low field approximation for Zeeman effect, for which the F-level splitting is linear with magnetic field. We have found, that this approximation is not sufficient for fields bigger than approximately 1G, and the correction is more pronounced for ^{85}Rb . Thus, we used more exact Hamiltonian, which includes the interaction with the magnetic field in a form [89]

$$H_B = \frac{\mu_B}{\hbar} (g_J J_z + g_I I_z) B \quad (6.17)$$

with Bohr magneton μ_B , z - projections of total electron and nuclear angular moment J_z and I_z , and corresponding Landé factors g_J, g_I (see section 1.6)

For calculations we supposed that the transitions from $F_g = 1$ and $F_g = 2$ for ^{87}Rb and from $F_g = 2$ and $F_g = 3$ for ^{85}Rb can be treated separately in Hamiltonian because of relatively big frequency differences between the ground levels. Of course, it is necessary to take into account both levels for relaxation part of Eq (6.4). To check the validity of the approximation, for ^{85}Rb we performed partial calculations taking into account the ground level separation as well. The algorithm was managing the frequency separation of $\Omega = 3.0\text{GHz}$ without a major difficulty, but the time step has to be reduced at least to 1/20 of relaxation time to eliminate small spurious subharmonic resonances around $\Omega/3,4,5$ etc.

The difference in the results with independent ground levels approximation was comparable to rounding errors because of finite integration intervals, and we estimate them as < 0.03 of the maximal signal value. The calculation errors can be reduced by making the calculation longer (reducing time step, taking bigger intervals for time of flight and taking closer spaced points for spectra).

First we obtained dynamics of density matrix in function of detuning across upper levels. The dipole moment evolution for left and-right circularly polarized components is obtained; it is averaged according to the arrival time to the center of

the beam with Maxwell velocity. The last step is a convolution of a spectrum as function of detuning with Gaussian curve, which gives the theoretical spectral shape.

6.8 Experiment, absorption and rotation measurements

In the first experiment we measured the absorption for circularly polarized light as function of intensity at nominally zero magnetic fields. The circular diaphragm was placed in front of the cell in the central part of Gaussian beam. The intensity distribution across the diaphragm was close to uniform, with variations typically smaller, than 10%. The light intensity after the cell was measured at the center of a beam by a photodetector with 0.5mm diameter aperture. The temperature $30^{\circ}C$ was chosen to ensure that the absorption is not very high, and the intensity does not vary much along the cell.

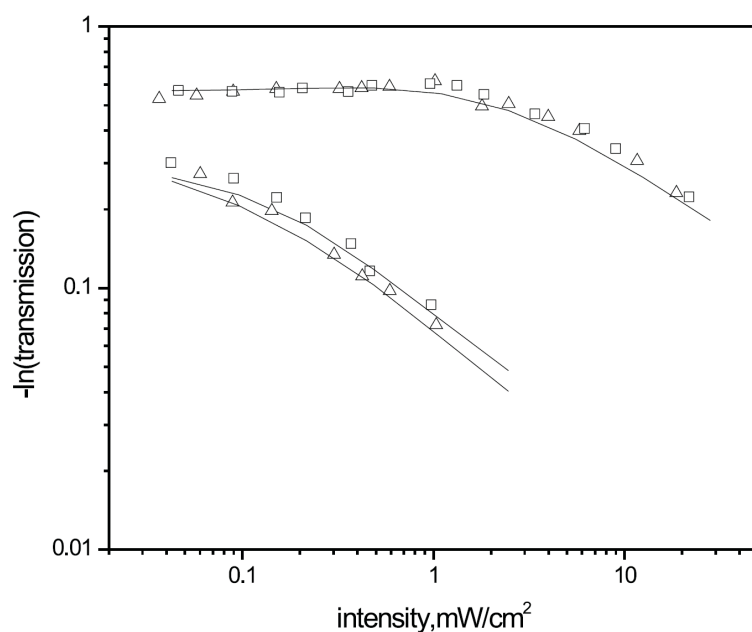


Figure 6.12 Transmission logarithm for 50mm long cell at $30^{\circ}C$ for circularly polarized beam with radius $l_0 = 1.19mm$ (triangles) and $l_0 = 0.78mm$ (squares). Upper curve - $F_g = 2$ line, lower - $F_g = 1$. Solid lines are theory for corresponding beam radius (also see Fig.6.8). For $F_g = 2$ transition, the theory gives very close curves, and only $l_0 = 1.19mm$ one is shown. To fit the data we used the vapor density which is approximately 10% lower, than the value found according to Ref.[15] for this temperature.

The results are presented in Figure 6.12. It is seen, that the computer model gives quite accurate description of absorption dependence on intensity for both $F_g = 1$, and $F_g = 2$ transitions. Note, that the only fitting parameter used here is the vapor density, common for both lines the intensity scale is absolute, and the true beam diameter was used in the calculation. The fitting vapor density value is about 10% smaller, than the one taken from Ref.[15] and used in Fig.6.8 ($1.5 \cdot 10^{10} cm^{-3}$). For $F_g = 1$, the difference in absorption between apertures with 0.78mm and 1.19mm radius is clearly seen, and generally corresponds to the theory, as well as absolute absorption values. We did not perform experiments with much smaller apertures, because diffraction effects are pronounced in this case.

The nonlinear Faraday rotation was measured using 45° rotated polarizer with a technique described in Ref.[77]. Note, that the raw data $\nu(B) = [I_p(B) - I_p(0)] / I_p(0)$ (where $I_p(B)$ is the detector signal as function of magnetic field) cannot be used as the direct measure of Faraday rotation because of noticeable influence of magnetic field induced absorption (Figs.6.10 and 6.11). In particular, the obtained curve is not antisymmetric with respect to magnetic field ($\nu(-B) \neq -\nu(B)$), as it must be for pure Faraday rotation. It is easy to see, that the resulting curve in the approximation of small signal is the sum of a term proportional to the absorption curve discussed earlier, and a term proportional to the Faraday rotation angle. For 45° rotated polarizer, the two curves enter with

equal coefficients. Thus, we have compared the experimental curves in Figs.6.13 and 6.14 with the combination of theoretically calculated absorption and rotation. The theoretical curves are shown with dots; all are taken for the same vapor density.

It is seen, that the theory gives generally adequate description of complicated polarization behavior, including good predictions for relative rotation magnitudes in two different lines. The signs of rotation for small magnetic fields in two lines are opposite, as predicted by the theory.

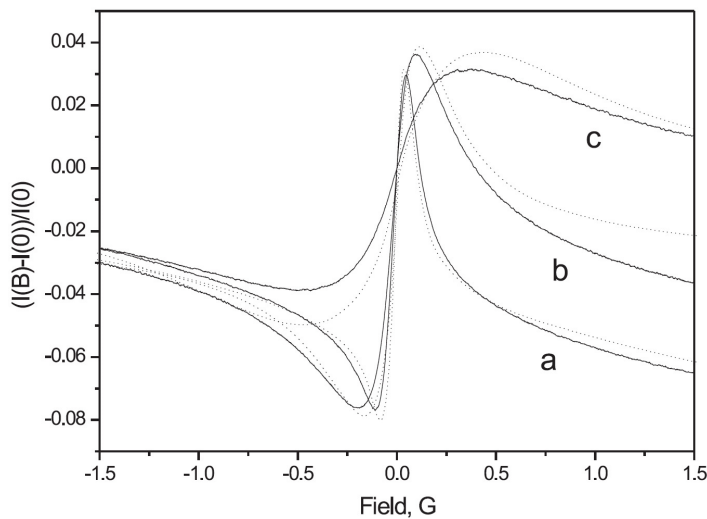


Figure 6.13 Photodetector signal after 45° turned polarizer as function of magnetic field for linear input polarization and different light intensities in $F_g = 1$ F line (solid). Intensity values and beam radius are the same, as those used for calculation in Fig.6.10. Temperature $30^\circ C$. Dashed lines are theoretical curves.

We measured light absorption dependence on the magnetic field for linearly polarized light as well. These curves also correspond quite well to the theory. The narrow spike, obtained in $F_g = 1$ line for small intensity is a good indicator of zero

magnetic field condition. For $F_g = 2$ line, the magnetic-field induced transmission spike is much wider, than for $F_g = 1$, and it has additional narrow feature around zero magnetic field.

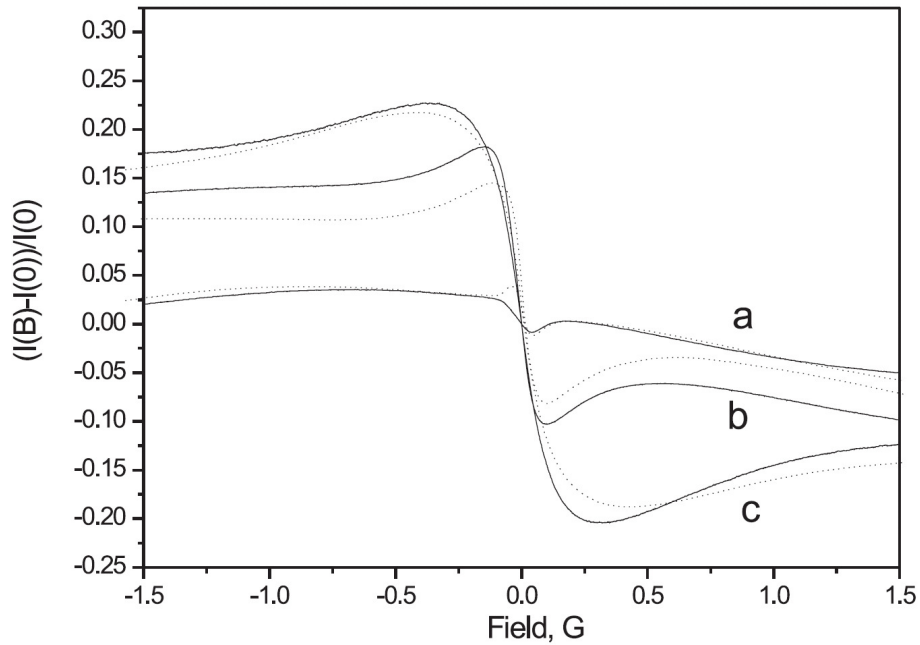


Figure 6.14 The same, as in Fig.6.7, but for $F_g = 2$ line

The small field feature in $F_g = 2$ line changes its form, when the frequency is scanned inside the line, thus some minor effects exist there, which are not taken into account by our theoretical analysis. The general character of the spike is reasonably well reproduced by a theory, though the agreement is somewhat worse here, than for $F_g = 1$.

6.9 Experiment, hologram writing

In our experiment the Bragg regime is realized if the angle between writing beams is bigger than approximately 5 mrad . In two-wave mixing experiments dynamic hologram is often detected by closing the signal beam and monitoring the diffraction of a reference wave in the direction of signal. For rubidium, the writing/erasing time can be less than 100 ns ; this makes such method quite complicated technically. Because of this, for measurements we crossed a strong reference beam and a weak signal beam at sufficiently small angle to obtain a non-Bragg (conjugated) diffraction order, produced by the diffraction of a strong beam on the grating written by it with a signal. The basic configuration here is a three-wave mixing. Small angle also helps to keep the interacting beams with good overlap. Similar setup was used in Ref.[77].

The experiment is depicted in Fig.6.5. For efficient hologram writing the temperature has to be high enough, and this produces strong absorption. Raising the temperature even more results in diminishing of the diffraction signal because absorption dominates the output intensity. There is the optimal writing temperature, which depends on beam parameters, and it is different for $F_g = 1$ and $F_g = 2$ transitions. The simplest method for hologram writing in Rb is to use circular polarization and amplitude grating at $F_g = 2$ line. This can be done at zero magnetic field, and the magnetic field influence is not significant. If the total absorption is not very big because of high temperature, the signal is maximal close to the center of the line. The diffraction efficiency reasonably corresponds to the estimation made with known dependence of absorption on light intensity. The maximal efficiency obtained for $T = 91^\circ\text{C}$ is $\sim 1\%$, consistent with characteristic values for amplitude holograms. Note that gratings with efficiencies somewhat higher than those shown in figures can be written with equal beam intensities. In Figs.6.15 and 6.16 we show diffraction efficiency dependences on frequency detuning for two light intensities. For circular polarization and small intensity (Fig.6.15), the cut-off frequency $\nu = 8.5 \pm 0.5\text{ MHz}$ (as taken by a two times drop in

diffraction efficiency) gives characteristic writing time $\tau_R = (2\pi\nu)^{-1} \approx 20ns$. This time is comparable with the upper level lifetime ($25ns$), and becomes somewhat smaller for bigger intensity. When the signal beam is switched on and off, as described earlier, no transient processes are seen in diffraction at times $> 100ns$, which we can resolve directly.

The diffraction efficiency η for the $F_g = 2$ transition can be improved by using linear polarization and weak magnetic field. The dependences of η on magnetic field at zero detuning are shown in the inserts.

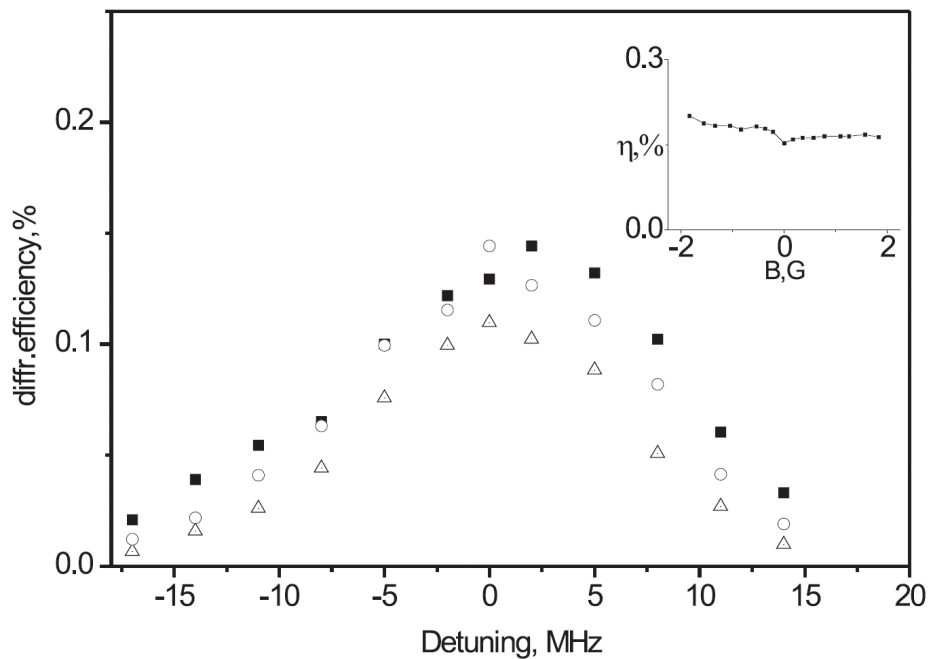


Figure 6.15 Diffraction efficiency at the center of $F_g = 2$ line for average light intensity

$I = 7.5mW/cm^2$ vs detuning between writing beams; squares -circular polarization and zero magnetic field, triangles -plane polarization and zero magnetic field, circles – plane polarization and magnetic field $B = 0.65G$ Insert -dependence of diffraction intensity on magnetic field for plane polarization, $T = 91^\circ C$.

It is seen, that for small intensity, magnetic field application does not produce big change, but for higher intensities the influence is well pronounced. At the magnetic field, which gives the maximal signal, the spike around zero detuning appears, its width gives characteristic time comparable to the flight of time across the fringe (Fig.6.16).

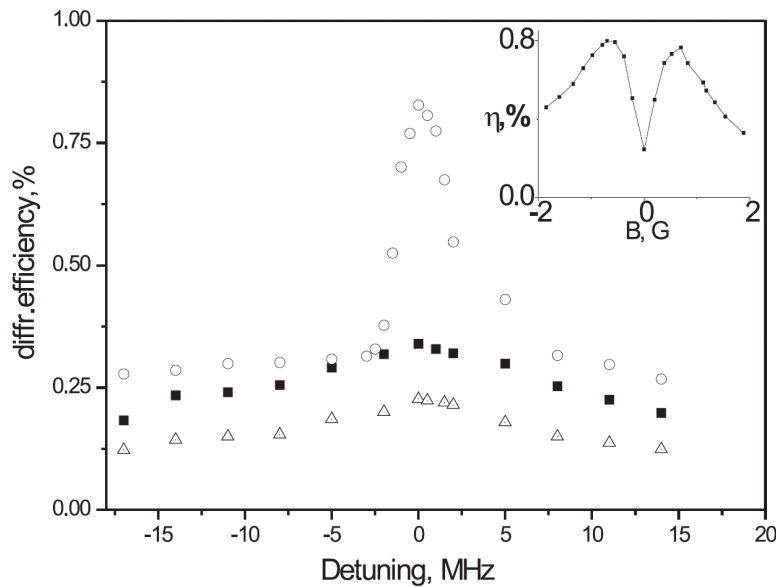


Figure 6.16 The same, as in Fig.6.15, but for light intensity $I = 67 mW / cm^2$. Dependence of diffraction efficiency on detuning for plane polarization is taken for $B = 0.6 G$ which gives the maximum in field dependence (insert).

The transient processes are seen at sub-microsecond scale after opening/closing the signal beam, and the transients can have a shape of exponential relaxation with more than one characteristic time, or strongly damped oscillation, depending on magnetic field. The relaxation time corresponds to characteristic frequency detuning in the central spike.

For $F_g = 1$ transition, the circular polarization writing is not efficient. For plane polarization, different from the situation with $F_g = 2$, the maximum in diffraction efficiency is obtained for intensities $10 - 20 \text{ mW/cm}^2$, and diminishes if intensity is bigger (Fig. 6.17). This is related to the drop in rotation for big intensities, discussed in the previous section and in the theoretical part. Efficient writing is obtained for nonzero field (Fig. 6.18, insert), the signal as a function of detuning between writing beams strongly diminishes for $1 - 2 \text{ MHz}$ detuning.

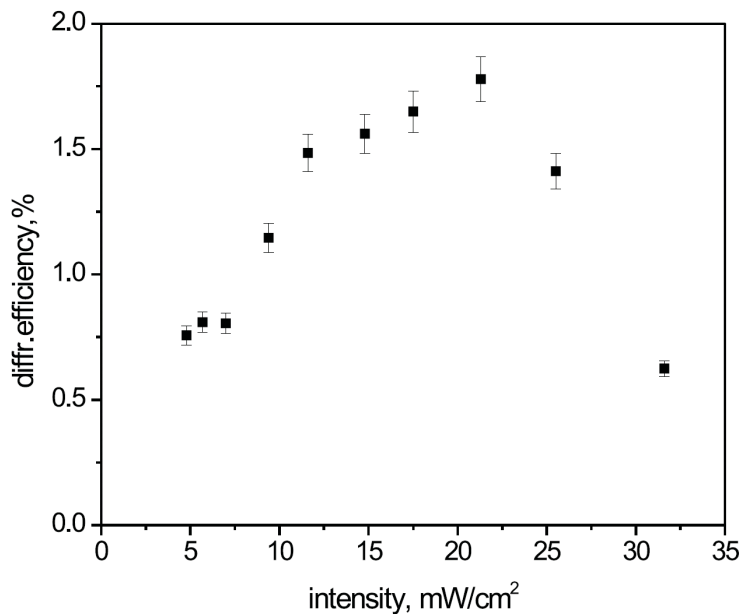


Figure 6.17 Dependence of diffraction efficiency for plane polarization on light intensity for $F_g = 1$ transition at zero frequency detuning between beams. The magnetic field for each measurement was taken to produce maximal diffraction, the temperature $T = 113^\circ \text{C}$.

Making intensity smaller does not change the character of this curve. The transients are seen after opening and closing the beam, similar to those observed for $F_g = 2$. The temperature, for which the diffraction is efficient, is higher here than

for $F_g = 2$, because both absorption and optical rotation per atom are smaller, and higher vapor densities are needed. For mechanisms with polarization rotation we observe usual for dynamic holography trade-off between diffraction efficiency and writing time.

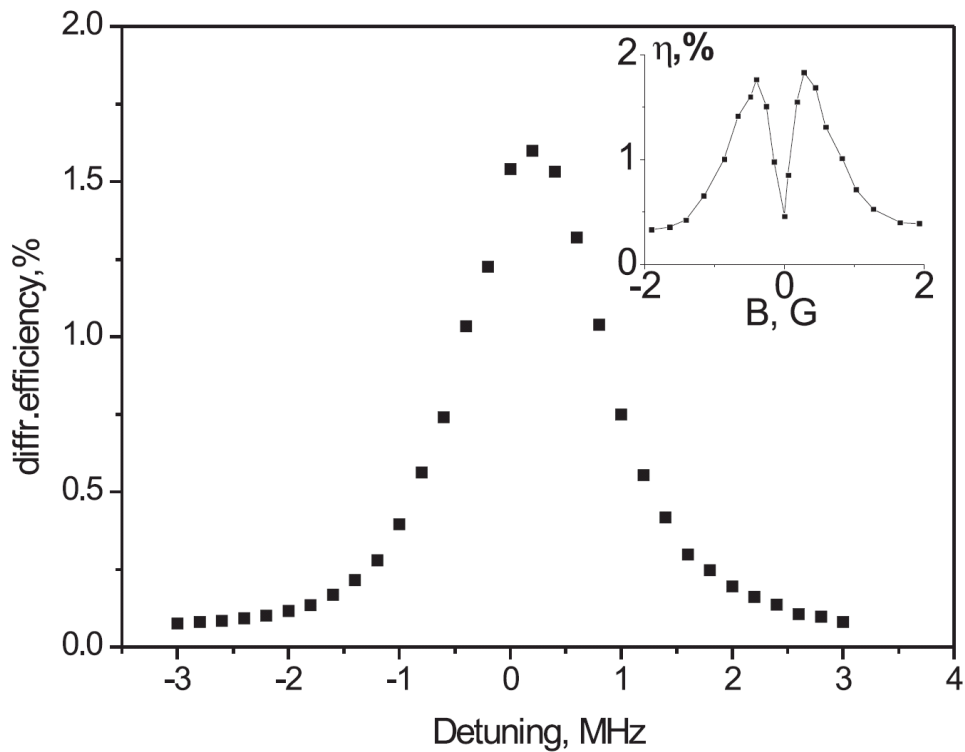


Figure 6.18 Dependence of diffraction efficiency for plane polarization on frequency detuning between writing beams for $F_g = 1$ transition for magnetic field $0.28G$, and its dependence on magnetic field for zero detuning (insert). Light intensity is $I = 22mW/cm^2$, the temperature $T = 113^\circ C$.

6.10 Experiment 2. Results

The results of experiment 2 are presented in Figure 6.19. It is seen, that the calculation of Section 6.9 gives quite satisfactory description of complicated

spectrum behavior for all lines. For the open transitions the rotation signs are different for small and big magnetic fields. For big enough magnetic field, the lineshape can be strongly distorted from a nearly Gaussian form. In $^{87}\text{Rb } F_g = 1$ transition, the change of sign inside the line is possible. This occurs because the rotation directions from $F_e = 0,1$ and $F_e = 2$ are opposite, and close to zero overall rotation corresponds to a situation when the sum is close to zero.

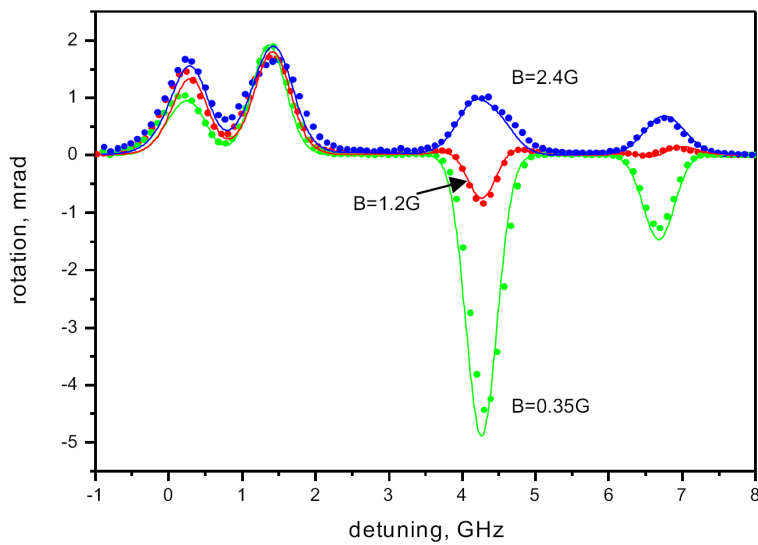


Figure 6.19 Theory (lines) and experiment (points) for light intensity $I = 1.1 \text{ mW/cm}^2$, beam diameter 1 mm , temperature 21° C , the vapor density is common for all magnetic field values.

The calculated spectra and their comparison with the experiment are presented in Figure 6.19. It is seen, that the calculation gives quite satisfactory description of complicated spectrum behavior for all lines.

6.11 Discussion and conclusions

The experiments we performed were aimed mostly to establish the general validity of the proposed theory, thus the systematic errors could in some cases be as big as 10%. In particular, we did not use antireflecting coating for the rubidium cell, the nonuniformity in illumination across the aperture was around 10%, and we did not measure small absorptions in $F_g = 1$ transition with good precision. To avoid vapor density recalculations, we performed all rotation and absorption measurements for the same temperature $30^\circ C$, and we could not satisfy the condition of small absorption in all intensity range. The theory does not take into account systematically simultaneous interaction of light with adjacent F-levels, and finite Doppler width of line. For bigger intensities these two factors become more important. In particular, the influence of resonant self-rotation of elliptically polarized light cannot be neglected (we do not treat elliptical polarizations here).

However, for moderate intensities practically interesting for holography, the theory adequately describes the behavior of observed absorption and optical rotation, and it can be used as a guide for experimental investigation as well as for comparison with simplified theoretical approximations.

For holographic writing in ^{87}Rb close to resonance it is possible to employ absorption gratings for $F_g = 2$ line. Though the diffraction efficiency in this case is limited by $\sim 1\%$, the sensitivity is high, writing time can be as small as 20 ns, and there is no need for strict polarization and magnetic field control. The absorption grating for $F_g = 1$ transition is inefficient, because of the reasons explained in the theoretical part.

To obtain more efficient grating with phase component at resonance wavelength it is necessary to overcome absorption, thus the light intensity grows. Here, the magnetic field and polarization control are essential. The $F_g = 1$ transition is easily saturated, but much of the saturation comes from "useless" population transfer to

$F_g = 2$ level. With higher temperatures, the gratings with bigger diffraction efficiency, than those for the amplitude grating in $F_g = 2$ can be written. Generally, more efficient gratings require bigger writing time, and this can become a problem for smaller fringe spacing, when the time of flight across a fringe diminishes.

Holographic CW writing with two beams of nearly equal frequencies is experimentally the simplest, but it seems probable, that more favorable conditions can be obtained with additional illumination at another frequency, and/or by using nonstationary mechanisms. The rich level structure of rubidium provides many possibilities for manipulation.

In conclusion, we demonstrate that the density matrix formalism with big number of sublevels taken into account gives generally adequate description of processes important for holographic grating formation in rubidium vapor at moderate intensities. The analysis clarifies different factors involved, in particular the role of time of transit (beam diameter and fringe spacing). Some situations, such as absorption grating at $F_g = 2$ permit simple analytical approximations, but it seems that no simple model can account for complicated polarization behavior, which gives efficient phase gratings for strongly saturated lines.

The new results of the thesis are:

- development of split-step type algorithm for calculation of density matrix evolution, and experimental confirmation of its effectiveness for predicting the nonlinear behavior of Faraday rotation in rubidium vapor close to resonance.
- calculations of nonlinear absorption and refraction for some typical geometries of hologram writing, and their comparison with the experiment.
- clarifying the writing mechanisms for absorption gratings.

- Experimental determination of diffraction efficiencies and writing times for amplitude and phase gratings in some particular cases.

In particular, it was shown that:

- The proposed split-step solution algorithm permits to calculate with good accuracy the observed nonlinear spectra

- The holographic writing in rubidium is fast and efficient, and can be successfully used for adaptive optical detection of ultrasound.

List of Tables

Table 1.1 Atomic data for ^{87}Rb and ^{85}Rb

Table 1.2 Hyperfine constants A and B (in MHz) for the lowest three fine structure states in the two naturally-occurring Rb isotopes

Table 1.3 Density of Rubidium gas as a function of temperature

Table 4.1 Table of maximum diffraction efficiency for various hologram types

List of Figures

Figure 1.1 There are two commonly-occurring isotopes of Rubidium found in nature, ^{85}Rb and ^{87}Rb . Both have only one valence electron and can be approximated as one-electron atoms. The major difference between the isotopes is in the nuclear spin I .

Figure 1.2 The Lorentzian line shape profile for resonance absorption

Figure 1.3 Basic arrangement for ordinary laser absorption spectroscopy.

Figure 1.4 Maxwell-Boltzmann velocity distributions. The density of atoms vs. their velocity component in one direction for room temperature rubidium atoms.

Figure 1.5 Idealized three-level Λ system

Figure 1.6 The basic energy-level structure of a one electron atom(at the left). Bound states have negative energy and are quantized, with different allowed amounts of angular momentum for each energy level. To first approximation, all of the different angular momentum states have the same energy for a given energy number n . Fine structure (at the left en zoom) Taking the spin of the electron into account leads to a small splitting of the levels with orbital angular momentum. There are two angular momentum to consider, orbital and spin. The new notation is $^{2S+1}L_J$, where S is the electron spin ($1/2$ for one electron), L is the orbital angular momentum ($S, P, D, \text{etc.}$), and $J = L + S$ is the total angular momentum.

Hyperfine structure (at the right zoom) – Adding the spin of the nucleus further splits the levels. Here we have a close up of the $2p$ levels, split into $^2P_{1/2}$ and $^2P_{3/2}$ by the fine-structure correction. These fine-structure levels are split according to the total angular momentum $F = I + J$. This example illustrates the splitting for ^{87}Rb , which has $I = 3/2$. The $^2S_{1/2}$ level also gets split, in the same way as $^2P_{1/2}$.

Figure 1.7 Hyperfine structure— Adding the spin of the nucleus further splits the levels. Here we have a close up of the 2p levels, split into $^2P_{1/2}$ and $^2P_{3/2}$ by the fine-structure correction. These fine-structure levels are split according to the total angular momentum $F = I + J$. This example illustrates the splitting for ^{87}Rb , which has $I = 3/2$. The $^2S_{1/2}$ level also gets split, in the same way as $^2P_{1/2}$.

Figure 1.8. Energy levels for ^{85}Rb and ^{87}Rb (not to scale). Note that the hyperfine splittings are about an order of magnitude larger in the ground $^2S_{1/2}$ levels compared to the excited $^2P_{3/2}$ levels

Figure 2.1 Schematic diagram of the interaction of a two-level system with a radiation field

Figure 2.2 The Faraday and Voigt effects. In the Faraday effect light, after passing through a linear polarizer, enters a medium subjected to a longitudinal magnetic field \mathbf{B}_{\parallel} ($\mathbf{B}_{\perp} = 0$). Left- and right-circularly polarized components of the light (equal in amplitude for linearly polarized light) acquire different phase shifts, leading to optical rotation. A difference in absorption between the two components induces ellipticity in the output light. The intensity of the transmitted light with a particular polarization is detected depending on the orientation of the analyzer relative to the polarizer. Analyzer orientation varies with the type of experiment being performed. In forward scattering experiments, the analyzer is crossed with the input polarizer, so that only light of the orthogonal polarization is detected. In the “balanced polarimeter” arrangement, a polarizing beam splitter oriented at $\pi/4$ to the input polarizer is used as an analyzer. In this case, the normalized differential signal between the two channels of the analyzer depends on the rotation of light polarization while being insensitive to induced ellipticity. The Voigt effect is similar except that instead of a longitudinal magnetic field, a transverse field \mathbf{B}_{\perp} ($\mathbf{B}_{\parallel} = 0$) is applied. Here optical rotation and induced ellipticity are due to differential absorption and phase shifts of orthogonal linearly polarized components of the input light

Figure 2.3 An $F = 1 \rightarrow F' = 0$ atomic transition. In the presence of a longitudinal magnetic field, the Zeeman sublevels of the ground state are shifted in energy by $g\mu_B M$. This leads to a difference in resonance frequencies for left- (σ^+) and right- (σ^-) circularly polarized light.

Figure 2.4 The dependence of the refractive index on light frequency detuning Δ in the absence (n) and in the presence (n_{\pm}) of a magnetic field. Shown is the case of $g\mu_B = \hbar\Gamma$ and a Lorentzian model for line broadening (Fig.1.2) The lower curve shows the difference of refractive indices for the two circular polarization components. The spectral dependence of this difference gives the characteristic spectral shape of the linear magneto-optical rotation (the Malou-Lorentz effect).

Figure 2.5 Plot of the absorption $n_0 k$ and refractive index change $n_0 - 1$ for a gas near an atomic resonance. Note the index change is proportional to the first derivative of the absorption.

Figure 3.1. A schematic diagram of two-wave mixing in photorefractive materials

Figure 4.1 a) Recording of hologram; b) Reconstruction of hologram

Figure 4.2 Diffraction efficiency as a function of the optical path variation in units of the wavelength for a thick phase hologram viewed in transmission.

Figure 5.1 The SSFM for one iteration of step h starting at $z = (j-1)h$. The initial pulse $\Psi(0, t)$ enters the medium of length L . The length is broken into $s_L = L/h$ steps of length h .

Figure 6.1 Laser System Details

Figure 6.2 Scheme of a system in Littman configuration, taken from New Focus

Figure 6.3 Output power vs injection current curve at two different temperatures

Figure 6.4: a) input(sinusoidal) and reference(square) signal, b) result of the multiplication of the input signal and reference.

Figure 6.5 Experimental setup. AOM 1,2 -acousto-optical modulators; M1-M3 – mirrors; PD -photodetector. The angle between writing beams is exaggerated for better visibility. The second modulator produces the frequency-shifted beam slightly above the picture plane.

Figure 6.6 Experimental set-up 2. L1 and L2 a telescopic lens, P1, P2 are polarizer's, PD - photodetector with a small aperture, B - magnetic field

Fig. 6.7 The sublevel structure for ^{87}Rb D2 line. Numbers -3...3 are momentum projections on quantization on z-axis, m_F . Energy differences between levels are not to scale. As an example, the transitions induced by right (solid arrows) and left circular polarizations (dashed arrows) between $F_g = 1$ and $F_e = 1$ levels are shown.

Fig. 6.8 Absorption calculation for circularly polarized light as function of intensity for $F_g = 1$ and $F_g = 2$ lines in the center of circular beam with uniform intensity distribution and radius $l_0 = 0.12\text{mm}$ (solid) and $l_0 = 1.19\text{mm}$ (dots). The calculation is made for natural Rb at temperature 30°C using data of Ref.[15].

Figure 6.9 Faraday rotation for $F_g = 1$, $F_e = 0$ transition. The numeric example shows that for nonzero magnetic field refractive indexes for left (dash) and right circular polarizations (dash-dot) have different dependences on detuning from transition frequency. The difference (solid line) does not disappear if integrated with respect to detuning, thus this mechanism is important for Doppler broadened line. Light intensity $2.13\text{mW}/\text{cm}^2$, magnetic field 0.12G , beam radius $l_0 = 1.19\text{mm}$.

Figure 6.10 Real and imaginary parts of calculated dipole moment divided by field amplitude, which are proportional to optical activity (solid) and absorption (dots) vs magnetic field for different light intensities in $F_g = 1$ line. Intensities are:

a) $0.216\text{mW}/\text{cm}^2$, b) $2.13\text{mW}/\text{cm}^2$, c) $19.2\text{mW}/\text{cm}^2$, the beam radius is $l_0 = 1.19\text{mm}$.

Figure 6.11 The same, as in Figure 6.10, but for $F_g = 2$ line.

Figure 6.12 Transmission logarithm for 50mm long cell at $30^{\circ}C$ for circularly polarized beam with radius $l_0 = 1.19mm$ (triangles) and $l_0 = 0.78mm$ (squares). Upper curve - $F_g = 2$ line, lower - $F_g = 1$. Solid lines are theory for corresponding beam radius (also see Fig.6.8). For $F_g = 2$ transition, the theory gives very close curves, and only $l_0 = 1.19mm$ one is shown. To fit the data we used the vapor density which is approximately 10% lower, than the value found according to Ref.[15] for the same temperature.

Figure 6.13 Photodetector signal after 45° turned polarizer as function of magnetic field for linear input polarization and different light intensities in $F_g = 1$ F line (solid). Intensity values and beam radius are the same, as those used for calculation in Fig.6.10. Temperature $30^{\circ}C$. Dashed lines are theoretical curves.

Figure 6.14 The same, as in Fig.6.7, but for $F_g = 2$ line

Figure 6.15 Diffraction efficiency at the center of $F_g = 2$ line for average light intensity $I = 7.5mW/cm^2$ vs detuning between writing beams; squares -circular polarization and zero magnetic field, triangles -plane polarization and zero magnetic field, circles -plane polarization and magnetic field $B = 0.65G$ Insert - dependence of diffraction intensity on magnetic field for plane polarization, $T = 91^{\circ}C$.

Figure 6.16 The same, as in Fig.6.15, but for light intensity $I = 67mW/cm^2$. Dependence of diffraction efficiency on detuning for plane polarization is taken for $B = 0.6G$ which gives the maximum in field dependence (insert).

Figure 6.17 Dependence of diffraction efficiency for plane polarization on light intensity for $F_g = 1$ transition at zero frequency detuning between beams. The magnetic field for each measurement was taken to produce maximal diffraction, the temperature $T = 113^{\circ}C$.

Figure 6.18 Dependence of diffraction efficiency for plane polarization on frequency detuning between writing beams for $F_g = 1$ transition for magnetic field $0.28G$, and its dependence on magnetic field for zero detuning (insert). Light intensity is $I = 22mW/cm^2$, the temperature $T = 113^\circ C$.

Figure 6.19 Theory (lines) and experiment (points) for light intensity $I = 1.1mW/cm^2$, beam diameter $1mm$, temperature $21^\circ C$, the vapor density is common for all magnetic field values.

References

- [1] S Cauchi, A Vorozcovs, M Weel, S Beattie, et al., *Absorption Spectroscopy of Trapped Rubidium Atoms*, Canadian J. of Phys., **82**, 905-915, (2004).
- [2] Lee H S, Park S E, Park J D and Cho H, *Zeeman effect in the saturation spectroscopy of the ^{87}Rb D2 line*, J. Opt. Soc. Am. B, **11**, 558-5634, (1995)
- [3] Dmitry Budker, Valeriy Yashchuk, and Max Zolotarev, *Nonlinear Magneto-optic Effects with Ultranarrow Widths*, Phys. Rev. Lett. **81** 5788-5791, (1998);

- [4] K. B. MacAdam, A. Steinbach and C. Wieman, *A narrow-band tunable diode laser system with grating feedback, and a saturated absorption spectrometer for Cs and Rb*, Am. J. Phys. **60**, 1098-1111, (1992)
- [5] X.-W. Xia, D. Hsiung, P.S. Bhatia, M.S.Shahriar, T.T.Grove, P.R.Hemmer "Polarization selective motional holeburning for high efficiency, degenerate optical phase conjugation in rubidium," Opt.Comm., **191**, 347-351, (2001).
- [6] D. Budker, W. Gawlik, D.F. Kimball, S.M.Rochester, W.Yashchuk, A.Weis "Resonant nonlinear magneto-optical effects in atoms", Rev.Mod.Phys. **74**,1153-1201 (2002).
- [7] A.B.Matsko, I.Novikova, G.R.Welch, M.S.Zubairy "Enhancement of Kerr nonlinearity by multiphoton coherence", Opt.Lett., **28**, 96-98(2003)
- [8] J.A.Andersen, M.E.J.Friese, A.G.Truscott, Z.Ficek, P.D.Drummond, N.R.Heckenberg, H.Rubinsztein-Dunlop "Light guiding light: Nonlinear refraction in rubidium vapor," Phys.Rev. A, **63**, 023820 (2001).
- [9] C.F. McCormick, D.R.Solli, R.Y.Chiao, J.M.Hickman "Nonlinear absorption and refraction in near-detuned rubidium vapor", JOSA B, **20**, 2480-2483 (2003)
- [10] Korneev, N.; Benavides, *Mechanisms of holographic recording in rubidium vapor close to resonance*, O. JOSA B 2008, 25, 1899–1906.
- [11] Nikolai Korneev and Olena Benavides, *Direct multi-level density matrix calculation of nonlinear optical rotation spectra in rubidium vapour* Journal of Modern Optics, Vol. ??, No. ?, Month??, 1–5, 2009
- [12] Congress National de Physics, *Density Matrix Calculation of Nonlinear Absorption and Polarization Rotation in Rubidium Vapor*, Zacatecas, de 20-24 de October 2008
- [13] The 12th Topical Meeting on "Photorefractive Materials, Effects, and Devices, Control of Light and Matter", *Rubidium vapor as a material for dynamic holography: calculation of material properties*, in Bad Honnef (Germany), June 11-14, 2009.

- [14] H.J.Metcalf and P.van der Straten, *Laser Cooling and trapping*, Springer-Verlag, (1999)
- [15] D.A. Steck, <http://steck.us/alkalidata/rubidium87numbers.pdf>
- [16] *Saturated Absorption Spectroscopy, experiment SAS, University of Florida-Department of Physics PHY4803L-Advanced Physics Laboratory*, September 16, (2008)
- [17] B. E. A. Saleh, M. C. Teich: *Fundamentals of Photonics* (Wiley, New York (1991)
- [18] Y. R. Shen: *The Principles of Nonlinear Optics* (Wiley, New York (1984)
- [19] C. F. Klingshirn: *Semiconductor Optics* (Springer, Berlin, Heidelberg (1997)
- [20] E. M. Vogel, M. J. Weber, D. M. Krol: *Nonlinear optical phenomena in glass*, Phys. Chem. Glasses **32**, 231– 250 (1991) and cited papers E. M. Vogel: *Glasses as nonlinear photonic materials*, J. Am. Ceram. Soc. **72**, 719–724 (1989).
- [21] I. Kang, T. D. Krauss, F. W. Wise, B. G. Aitken, N. F. Borrelli: *Femtosecond measurement of enhanced optical nonlinearities of sulfide glasses and heavy-metal-doped oxide glasses*, J. Opt. Soc. Am. B **12**, 2053–2059 (1995)
- [22] Wolfgang Demtröder *Laser spectroscopy: Basic concepts and instrumentation*, Volume 1, page 222 , (1996)
- [23] R.Y.Chiao, E.Garmire, and C.Townes, Phys. Rev. Lett. **13**, 479 (1964)
- [24] S.A.Akhmanov, A.P.Sikhorukov, and R.V.Khokhlov, Usp. Fiz. Nauk **93**, 19 (1967)
- [25] W.Happer, Rev.Mod.Phys. **44**, 169(1972)
- [26] M.Arditi, and T.R.Carver, Phys.Rev.**124**,800(1961)
- [27] W.Happer, and B.S.Mathur, Phys.Rev.**163**, 12(1967)
- [28] B.S.Mathur, H.Tang, and W.Happer,Phys.Rev.**171**,11 (1968)

- [29] C.Cohen-Tannoudji and J.Dupont-Roc, Phys. Rev.A **5**, 968 (1972)
- [30] P.D.Maker, and R.W.Terhune, Phys.Rev. **137** A801(1965)
- [31] G.G.Adonts, D.G.Acopyan, and K.V.Arutunyan, J.Phys.B: At. Mol. Phys. **19**, 4113 (1986)
- [32] M.Fleischhauer, A.B.Matsko, and M.O.Scully, Phys.Rev. A **62**, 013808 (2000)
- [33] W.V.Davis, A.L.Gaeta, and R.W.Boyd, Opt.Lett. **17**, 1304 (1992)
- [34] Y.R.Chiao, J.Bowie, J.Boyce, D.Budker, J.C.Garrison, M.W.Mitchell, V.V.Yashchuk, T.K.Gustafson, and D.S.Hsiung, *Technical Digest of Conference on Lasers and Electro-Optics, Quantum Electronics and Laser Science*, **259** (1999)
- [35] D.Budker, Y.R.Chiao, D.S.Hsiung, S.M.Rochester, and V.V.Yashchuk, *Technical Digest of Conference on Lasers and Electro-Optics, Quantum Electronics and Laser Science*, **252** (2000)
- [36] I.Novikova, A.B.Matsko, V.A.Sautenkov, V.L.Velichansky, G.R.Welch, and M.O.Scully, Opt.Lett. **25**, 1651 (2000)
- [37] S.M.Rochester, D.S.Hsiung, D.Budker, Y.R.Chiao, D.F. Kimball, and V.V.Yashchuk, Phys. Rev. A **63**, 043814 (2001)
- [38] I.Novikova, A.B.Matsko, V.L.Velichansky, M.O.Scully and G.R.Welch, Phys. Rev. A **63**, 063802 (2001)
- [39] Budker, D.J.Orlando, V. Yashchuk, Am.J.Phys. **67**, 584(1999)
- [40] V.S.Letokhov, V.P.Chebotaev, *Nonlinear Laser Spectroscopy Springer Series in Optical Sciences*, Springer Verlag, Berlin, (1977)
- [41] Novikov, V. N., O. P. Sushkov, and I. B. Khriplovich, Opt. Spectrosk. **43**, 621 [Opt. Spectrosc. **43**, 370 (1977)]
- [42] Roberts, G. J., P. E. G. Baird, M. W. S. M. Brimicombe, P. G. H. Sandars, D. R. Selby, and D. N. Stacey, J. Phys. B **13**, 1389, (1980)
- [43] Khriplovich, *Parity Nonconservation in Atomic Phenomena* (Gordon and Breach, Philadelphia), (1991)
- [44] Papageorgiou, N., A. Weis, V. A. Sautenkov, D. Bloch, and M.

- Ducloy, Appl. Phys. B: Lasers Opt. **B59**, 123, (1994)
- [45] N.B.Delone, V.P.Krainov: *Fundamentals of Nonlinear Optics of Atomic Gasses*, by John Wiley and Sons, Inc. (1988)
- [46] Bonch-Bruevich, A., and V. Khodovoi, Usp. Fiz. Nauk **93**, 71, 1967 [Sov. Phys. Usp. **10**, 637 (1968)]
- [47] Bakhramov, S. A., A. T. Berdikulov, A. M. Kokharov, and V. V. Tikhonenko, Phys. Lett. A **141**, (1989)
- [48] Davis, W. V., A. L. Gaeta, and R. W. Boyd, Opt. Lett. **17**, 1304, (1992).
- [49] Govind P. Agrawal. *Nonlinear fiber optics*, Third Edition, page 18. Academia Press, San Diego (2001)
- [50] Advanced physics laboratory “*Interferometric measurement of resonant absorption and refractive index in rubidium*”
- [51] M.P.Petrov, S.I.Stepanov, A.V.Khomenko, *Photorefractive Crystals in Coherent Optical Systems*, Springer Series in Optical Sciences **59**, (Springer Verlag, Berlin, 1991).
- [52] V.L.Vinetskii, N.V.Kukhtarev, S.G.Odulov, and M.S.Soskin, “*Dynamic self-diffraction of coherent light beams*”, Sov. Phys.-Usp., vol. **22**, pp 742-756, (1979)
- [53] N.V.Kukhtarev, V.B. Markov, S.G.Odulov, M.S.Soskin and V.L.Vinetskii, “*Holographic storage in electro-optic crystals. Beam coupling and light amplification*,” Ferroelectrics, vol. **22**, pp 961-964, (1979)
- [54] P.Yeh *Two-wave mixing in nonlinear media*, IEEE Journ. of Quantum Electr., pp. 484-519, (1989)
- [55] A.Yariv and P. Yeh, *Optical Waves in Crystals*, New York: Wiley, (1984)
- [56] J.P.Huignard and A. Marrakchi, “ *Coherent signal beam amplification in two-wave mixing experiment with photorefractive BSO crystals*, Opt.Comm., vol. **38**, p. 249, (1981)
- [57] M. B. Klein and R. N. Schwartz, “*Photorefractive effect in BaTiO₃*:

- Microscopio origins,*” *J. Opt. Soc. Am. B* **3**, p. 293, (1986)
- [58] T. J. Hall, R. Jaura, L. M. Connors, and P. D. Foote, “*The photorefractive effect - a review,*” *Prog. Quant. Electr.* **10**, p. 77, (1985)
- [59] H. Kogelnik, “*Coupled-wave theory of thick hologram gratings,*” *Bell Syst. Tech. J.* **48**, 2909–2947 119692.
- [60] A. Yariv, *Quantum Electronics*, (John Wiley & Sons, New York, 1989)
- [61] N. Bloembergen, “*Conservation Laws in Nonlinear Optics,*” *J. Opt. Soc. Am.* **70**, 1429-1436 (1980)
- [62] J. F. Reintjes, *Nonlinear Optical Parametric Processes in Liquids and Gases*, (Academic Press, Orlando, 1984)
- [63] H. Kogelnik: *Coupled wave theory for thick hologram gratings*, AT&T Tech. J. **48**, 2909–2947 (1969)
- [64] R. Hioki, T. Suzuki: *Reconstruction of wavefronts in all directions*, *Jpn. J. Appl. Phys.* **4**, 816 (1965)
- [65] T. H. Jeong, P. Rudolf, A. Lockett: *360° holography*, *J. Opt. Soc. Am.* **56**, 1263 (1966)
- [66] L. H. Lin: *Edge-illuminated hologram*, *J. Opt. Soc. Am.* **60**, 714 (1970)
- [67] P. Hariharan: *Optical holography*, 2 edn. (Cambridge Univ. Press, Cambridge 1996)
- [68] R.Karplus, J.Schwinger: *Phys. Rev.* **73**, 1020(1948)
- [69] N.G.Basov, A.M.Prokhorov : *Uspekhi Fiz. Nauk* **57**, 485 (1955)
- [70] C. Cohen-Tannoudji, J. Dupont-Roc, G. Grynberg *Atom-Photon Interactions* John Wiley & Sons, Inc., New York, pp. 355-360, (1992)
- [71] T.R. Taha and M.J. Ablowitz. *J. Comput. Phys.* **55**:203 (1984)
- [72] R.H. Hardin and F.D. Tappert. *SIAM Rev. Chronicle* **15**:423 (1973)
- [73] R.A. Fisher and W.K. Bischel. *Appl. Phys. Lett.* **23**:661 (1973); *J. Appl. Phys.* **46**:4921 (1975).
- [74] Bruna I. Grimberg, Vadim V. Lozovoy, Shaul Mukamel and Marcos Dantus, *J. Phys. Chem. A*, Vol. **106**, No. 5, (2000)
- [75] Zwanzig, R. *Lect. Theo. Phys.*, **3**, 106, (1961)

- [76] Mukamel, S. *Phys. Reports*, **93**, 1, (1982)
- [77] N.Korneev, J.Soto "The nonlinear Faraday rotation-based dynamic holography in rubidium vapor," *Opt.Comm.*, **245**, 437-442 (2005).
- [78] New Focus, www.newfocus.com
- [79] M. G. Littman and H. J. Metcalf, "*Spectrally narrow pulsed dye laser without beam expander*," *Applied Optics*, vol. **17**, pages 2224–2227, (1978)
- [80] M. G. Littman, "*Single-mode operation of grazing-incidence pulsed dye laser*," *Optics Letters*, vol. **3**, pages 138–140, (1978)
- [81] M. G. Littman, "*Single-mode pulsed tunable dye laser*," *Applied Optics*, vol. **23**, pages 4465–4468, (1984)
- [82] K. Liu and M. G. Littman, "*Novel geometry for single mode scanning of tunable lasers*," *Optics Letters*, vol. **6**, pages 117–118, (1981)
- [83] G.S.Agrawal, *Quantum Statistical Theories of Spontaneous Emission and Their Relation to Other Approaches*, Springer tracts in modern physics **70**, (Springer Verlag, Berlin, 1974)
- [84] K. Mølmer, Y.Castin, J.Dalibard, "*Monte Carlo wave-function method in quantum optics*", *JOSA B*, **10**, 524-538 (1993)
- [85] V. S. Letokhov, V.P.Chebotayev *Nonlinear Laser Spectroscopy*, Springer Optical Sciences Series, Vol. **4**, (Springer Verlag, Berlin, 1977).
- [86] E. Arimondo, "*Coherent population trapping in laser spectroscopy*," in *Progress in Optics*, Vol. **35**, E. Wolf, ed., (Elsevier Science, Amsterdam, 1996).
- [87] W.H.Louisell, *Quantum Statistical Properties of Radiation* (Wiley, N.Y., (1973)
- [88] S.M. Rochester, D. S. Hsiung, D. Budker, R. Y. Chiao, D.F. Kimball, and V.V. Yashchuk, *Self-rotation of resonant elliptically polarized light in collision-free rubidium vapor*, *Phys. Rev. A* **63**, 043814 (2001)
- [89] G.P.Agrawal *Nonlinear Fiber Optics* (Optics and Photonics, 3-rd ed., Ac. Press, San Diego, 2001.
- [90] D.A.Steck *Rubidium 85 D Line Data* at <http://steck.us/alkalidata>

Resumen En Extenso

Los medios holográficos dinámicos, en particular los materiales fotorrefractivos, han sido propuestos para varias aplicaciones, incluyendo interferometría holográfica de tiempo real, conjugación de fase, procesamiento de imágenes, filtros, memoria etc.

El tiempo de respuesta de tales hologramas dinámicos varía desde segundos hasta nanosegundos según el tipo del material sensible a la luz (cristales, gas, tintes, etcétera). Un área activa de investigación es la búsqueda de nuevos medios fotorrefractivos que tengan la mejor respuesta de tiempo y sensibilidad.

Los átomos de metales alcalinos proveen el prototipo más simple para estudios espectroscópicos de alta resolución de la estructura de nivel de energía atómica y probabilidades de transición bajo la influencia de campos magnéticos y eléctricos aplicados. Incluso aunque los espectros de ^{85}Rb y ^{87}Rb han sido estudiados, hubo muy pocas investigaciones de la aplicación del vapor de rubidio para la holografía de tiempo real (holografía dinámica). El vapor de rubidio como material holográfico tiene algunas propiedades excepcionales.

Las propiedades no lineales del vapor de rubidio combinan con la espectroscopia compleja de este medio y aparecen efectos interesantes. En esta tesis veremos la teoría compleja de la espectroscopia de rubidio y los efectos magneto-ópticos que surgen con la aplicación del campo electro-magnético, en particular la rotación del plano de polarización.

Cuando un haz de laser linealmente polarizado interactúa en resonancia con un átomo en la presencia de un campo magnético externo, los diferentes componentes de polarización del campo incidente se acoplan a transiciones diferentes entre los subniveles Zeeman. Como resultado, la absorción y la dispersión de los diferentes componentes de polarización pueden ser diferentes,

dando lugar a efectos tales como el dicroísmo y la birrefringencia que resultan en cambios de la polarización (σ_+ and σ_-) de la luz transmitida.

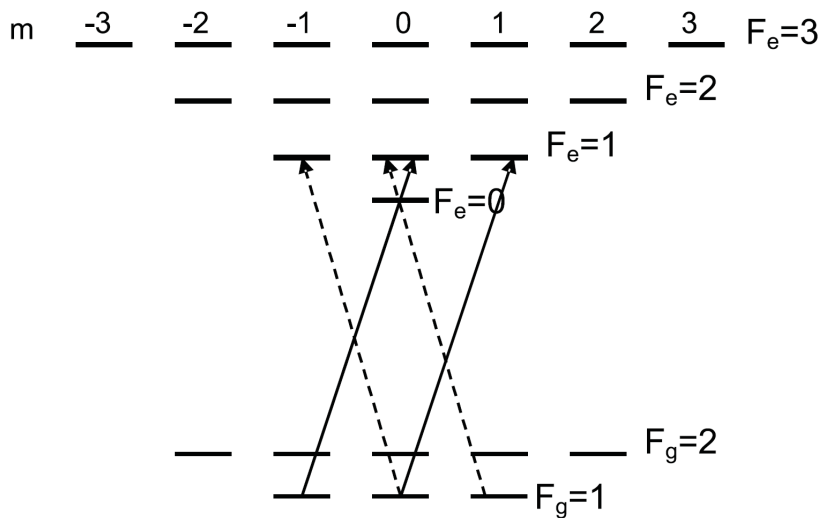
En este trabajo describimos los principios básicos de los efectos fotorrefractivos, que pueden aplicarse para explicar los procesos que ocurren en el vapor de rubidio en la presencia del campo electromagnético.

También investigamos la refracción no lineal y la absorción relacionada con la escritura holográfica en el vapor de rubidio en resonancia con la transición D2 en el isótopo ^{87}Rb . Se utiliza el modelo numérico basado en el formalismo de la matriz de densidad dependiente del tiempo. La teoría describe adecuadamente la rotación óptica no lineal y la absorción de la luz en el rango de intensidades de $0.1 - 30 \text{ mW/cm}^2$. Se han investigado experimentalmente las configuraciones básicas para la obtención de rejillas de amplitud y de fase para frecuencias próximas de haces de escritura y también se ha estimado el tiempo de grabado.

En este trabajo también se discuten los dos principales mecanismos de grabado de hologramas. El primero está basado en la escritura de rejilla de absorción y el otro es el mecanismo de formación de rejilla basado en la rotación del Faraday. Estos mecanismos son muy útiles para aplicaciones porque dan hologramas de fase con la eficacia de difracción más alta. Aquí también desarrollamos la teoría para ambos casos.

La descripción microscópica de la formación del holograma, puede hacerse desde principios básicos, pero la teoría adecuada es compleja debido al gran número de subniveles implicados (ver al Grafica 1, también el capítulo 1 de esta tesis).

En la resonancia surge el complicado comportamiento de polarización y el campo magnético puede cambiar radicalmente las propiedades de polarización observadas y la eficacia de la difracción. La fuerte dependencia en el tiempo de tránsito también es observada.



Grafica 1 La estructura de subniveles para la línea D2 de ^{87}Rb . Los números -3... 3 son proyecciones del momento en el eje z de cuantificación, m_F . La diferencia de energía entre niveles no está a escala. Como un ejemplo se muestran las transiciones inducidas de las polarización circular derecha (flechas sólidas) e izquierda (flechas punteadas) entre los niveles $F_g = 1$ y $F_e = 1$.

En particular, la absorción medida para $F_g = 1$ en la transición D2 del ^{87}Rb es afectada por el diámetro del rayo (ver a la Grafica 2). La teoría para el caso resonante, por lo que sabemos, no fue desarrollada detalladamente. Estudiamos un modelo numérico realista basado en el formalismo de la matriz de densidad. El número de subniveles participantes para nuestras condiciones experimentales es hasta 15, lo que significa solucionar hasta 225 ecuaciones diferenciales lineales para los elementos de la matriz. Además, la integración con respecto a la desintonía es necesaria para explicar el ensanchamiento Doppler. Calculamos la evolución temporal de la matriz, que permite incluir efectos importantes del tránsito.

La solución completa da una descripción muy detallada, incluyendo la dinámica de la población de los subniveles y la importancia relativa de diferentes F-niveles para el proceso particular. Aunque el modelo es bastante complicado, la buena concordancia con el experimento lo hace muy útil. En algunos casos se pueden derivar aproximaciones simplificadas.

Por motivos de la complejidad del cálculo al principio investigamos sólo uno de los isótopos presentes naturalmente, el ^{87}Rb que tiene el número más pequeño de subniveles. Este isótopo produce la rejilla más eficiente para las condiciones de nuestro trabajo experimental. La estructura de transiciones para el isótopo es representada en la Gráfica 1 (también ver el Capítulo 1). El nivel básico se divide en dos componentes hiperfinos con $F_g = 1$ y $F_g = 2$ de momento total, separado por 6.83GHz . En seguida estos dos niveles en la presencia del campo magnético se subdividen en 3 y 5 componentes de Zeeman respectivamente con $m_F = -F, \dots, F$. El conjunto de niveles excitados consiste en cuatro niveles hiperfinos con $F_e = 0, 1, 2, 3$.

Estos niveles también tienen subniveles Zeeman según su número F. La división hiperfina entre niveles superiores es 72MHz , 157MHz y 267MHz (ver la Sección 1.5 y 1.6). Cuando el ensanchamiento Doppler es de 0.5GHz , las transiciones dentro del conjunto de niveles superior no son resueltas y el espectro de absorción observado experimentalmente tiene dos líneas con $\approx 7\text{GHz}$ de separación.

Para simplificar el problema, asumimos que la luz de la frecuencia dada sólo interactúa con el nivel F más cercano del conjunto superior de un átomo con un desplazamiento Doppler definido. Esta suposición se rompe para la línea $F_g = 1$ al final superior de las intensidades investigadas experimentalmente, $5 - 30\text{mW/cm}^2$ donde la luz de la frecuencia dada puede interactuar simultáneamente con dos niveles cercanos $F_e = 0$ y $F_e = 1$.

La situación se manifiesta en un modelo de nivel superior cuando la anchura de rasgos espectrales característicos se hace comparable con la diferencia de frecuencia de 72.2MHz entre $F_e = 0$ y $F_e = 1$. Para intensidades aún más altas, son necesarios todos los tres niveles superiores de la transición permitida. Aunque nuestro software pueda manejar la tarea completa, la solución es considerablemente lenta. Así consideramos la interacción independiente con todos los niveles F_e , a excepción de la transición $F_g = 1, F_e = 0,1$ que es tratada por separado. Para el conjunto de niveles base, ambos subniveles $F_g = 1$, y $F_g = 2$ tienen que ser considerados, porque la excitación con la luz combinada con la emisión espontánea del nivel de transición superior induce la transferencia de la población entre ellos. Estas aproximaciones resultan ser adecuadas para intensidades no muy altas, que son típicas para la escritura holográfica.

Para la solución, tomamos la ecuación maestra para la matriz de densidad atómica ρ en la presencia de la emisión espontánea en la forma:

$$\frac{\partial \rho}{\partial t} = (i/\hbar)[\rho, H] + \sum_{q=-1,0,1} C_q \rho C_q^+ - \frac{1}{2}(C_q^+ C_q \rho + \rho C_q^+ C_q) \quad (1)$$

Donde el H es el hamiltoniano del átomo aislado, C_q, C_q^+ son los operadores de descenso y ascenso para el átomo multinivel. Se elige el eje z para la cuantificación a lo largo de la dirección de propagación de onda y paralelo al campo magnético. Todos los operadores ρ, H, C_q, C_q^+ son matrices $N \times N$ para un número de subniveles N . El hamiltoniano es tomado en la aproximación de dipolo, con los elementos diagonales iguales a las energías de los estados y los elementos no diagonales son proporcionales a los componentes circulares izquierdo y derecho de las polarizaciones del campo eléctrico de la onda. Estos elementos conectan estados con $F_e - F_g = 0, \pm 1$ y $m_{F_e} - m_{F_g} = \pm 1$ y son proporcionales a momentos de dipolo para una transición dada.

Los términos bajo la suma en el lado derecho describen la emisión espontánea.

Los operadores C_q, C_q^+ son proporcionales al operador de dipolo atómico:

$$C_q^+ |F_g, m_{F_g} \geq \Gamma^{1/2} (1, F_g, q, m_{F_g}; F_e, m_{F_e} = m_{F_g} + q) |F_e, m_{F_e} = m_{F_g} + q \rangle,$$

$$C_q^+ |F_e, m_{F_e} \geq 0$$

$$C_q = (C_q^+)^*,$$

con rango de decaimiento Γ , y coeficientes Clebsch-Gordan para acoplar los subniveles básicos excitados.

La aproximación de onda rotante estándar es usada para eliminar expresiones dependientes del tiempo en el hamiltoniano.

La Eq. (1) es resuelta numéricamente, tiene la forma

$$\frac{\partial \rho}{\partial t} = \Lambda(\rho),$$

Donde $\Lambda(\rho)$ es el operador lineal no dependiente del tiempo que actúa sobre los elementos de la matriz ρ (es representado por la matriz $N^2 \times N^2$, que se aplica al vector N^2 dimensional ρ , y no puede ser reducido a una multiplicación de ρ como matriz $N \times N$ por otra matriz $N \times N$). La solución formal es dada por:

$$\rho(t + \Delta t) = \exp(\Lambda \Delta t)(\rho(t)),$$

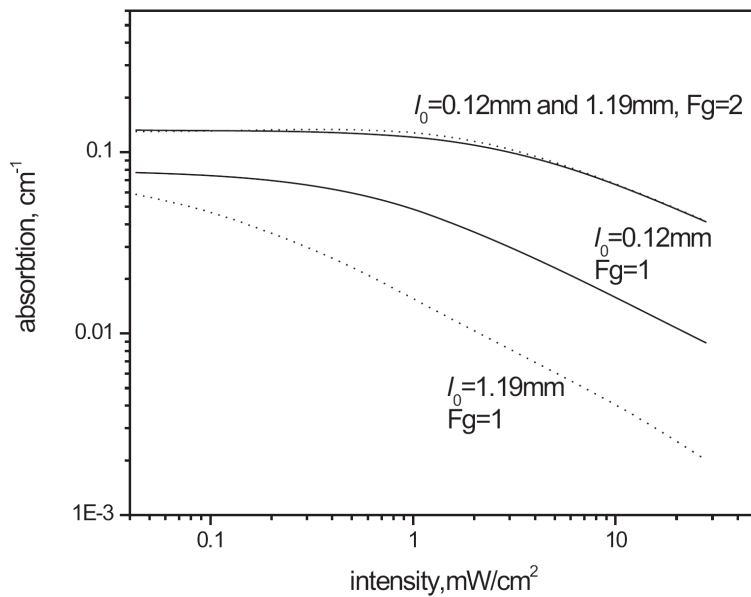
con un operador exponente. La solución numérica procede del cálculo del operador exponente con la serie de Taylor, y su aplicación consiguiente a $\rho(0), \rho(\Delta t) \dots$ etc. Como Λ es independiente del tiempo, el exponente de operador para un juego dado de parámetros sólo se calcula una vez. Este método de solución trabaja bien hasta $N \approx 18 - 20$, pero el tiempo de cálculo crece

rápida­mente con N , porque las escalas de tiempo de cálculo de exponente de la matriz crece como N^6 , y el resto del algoritmo de implementación como N^4 . También hemos puesto en práctica otro algoritmo de solución eficiente para N más grande. Lo describiremos adelante.

Desde un punto de vista macroscópico, los cambios de intensidad de la luz y del estado de la polarización afectan el coeficiente de absorción del medio y el índice refractivo. Si el vapor es iluminado con dos haces coherentes, los parámetros del medio varían en el espacio según los cambios locales de polarización y/o de intensidad. Esto produce una rejilla holográfica, que puede ser detectada por la difracción de haces.

La información sobre la iluminación local es registrada en el medio atómico ya sea en la forma de poblaciones de subniveles, que son los elementos diagonales de la matriz de densidad, o en la forma de coherencias cuánticas, dadas por los elementos no diagonales de la matriz. Pueden inducirse coherencias duraderas entre niveles inferiores mediante luz con una sola frecuencia si ambas polarizaciones circulares están presentes, en particular para la polarización lineal.

Primero, consideramos el caso de la estricta polarización circular del haz incidente, para el cual las coherencias entre niveles inferiores son ausentes. En este caso, para el centro de la línea la rejilla es del tipo de absorción. Así, para estimar la difracción es suficiente calcular la absorción como una función de la intensidad de la luz. Estas dependencias (Grafica 2) son cualitativamente diferentes para las líneas de transición $F_g = 2$ y $F_g = 1$.



Grafica 2 Cálculo de la absorción de la luz circularmente polarizada como función de la intensidad para $F_g = 1$ y $F_g = 2$ líneas en el centro del haz circular con la distribución uniforme de la intensidad y el radio $l_0 = 0.12mm$ (sólido) y $l_0 = 1.19mm$ (puntos). El cálculo se hace para el Rb natural con la temperatura $30^\circ C$

Para la transición de la línea $F_g = 2$, la absorción para intensidades grandes I se comporta aproximadamente como $(1 + I/I_{sat})^{-1/2}$, (I_{sat} es la intensidad de saturación cerca de $1-3mW/cm^2$), y es relativamente independiente en el diámetro de haz incidente (tiempo del tránsito). Tal comportamiento viene del modelo simple del átomo de dos niveles. Notamos que la transición de $F_e = 3$ a $F_g = 1$ está prohibida en la aproximación de dipolo, así el átomo con la transición excitada de $F_g = 2$ a $F_e = 3$ tras algún tiempo de iluminación llega al estado aislado con $m_{F_g} = \pm 2, m_{F_e} = \pm 3$ para la polarización circular derecha (izquierda), y el átomo se comporta esencialmente como si tuviera sólo dos niveles.

Para la transición con $F_g = 1$, incrementando el diámetro del haz se reduce perceptiblemente la absorción, y la intensidad de saturación característica es mucho más pequeña que para la transición $F_g = 2$. La absorción disminuye con la intensidad más rápido que $I^{-1/2}$. Esto ocurre porque las transiciones inducidas por la luz de $F_g = 1$ a $F_e = 2$ transfieren la población al nivel "invisible" $F_g = 2$ a consecuencia de la emisión espontánea. La transición lambda $F_g = 1$ a $F_e = 0$ aislada del nivel $F_g = 2$ para la polarización circular acumula átomos en un estado, que también es no absorbente para esta polarización circular particular.

Para la transición de $F_g = 1$ a $F_e = 1$, la combinación de los factores arriba mencionados funciona -la población es parcialmente transferida al estado $m_F = \pm 1$, y parcialmente a los estados $F_g = 2$. Así, la absorción vista para la línea $F_g = 1$ es resultado de un proceso transitorio y depende críticamente de los átomos que entran al haz desde fuera (las colisiones dentro de un haz pueden ser despreciados debido a la concentración baja de átomos). El tiempo de la despoblación $F_g = 1$ para pequeñas intensidades se hace más grande, que el tiempo de tránsito, así que la absorción para las pequeñas intensidades tiende a un valor constante, que no depende del diámetro del haz.

Los diferentes caracteres de la saturación producen marcadas diferencias en la eficacia de difracción para la rejilla de la absorción en las líneas $F_g = 2$ y $F_g = 1$. En el caso $F_g = 2$, la dependencia medida de la transmisión en la intensidad da la luz da una buena estimación para la eficacia de difracción. En la transición $F_g = 1$, la anchura del haz se hace importante: cerca del centro del patrón de la interferencia los átomos se hacen "transparentes", ellos no responden a cambios locales de la iluminación y la eficacia de difracción es completamente pobre allí.

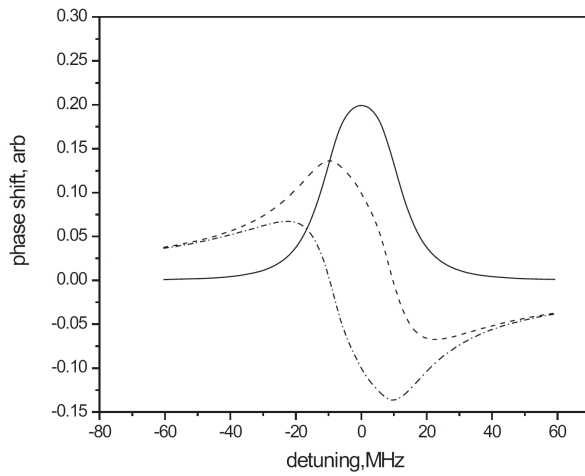
La transición de $F_g = 1$ se hace mucho más eficiente para la holografía, si se incluyen los efectos de la coherencia cuántica, que se aparece para polarizaciones no circulares, y es aplicado un campo magnético débil.

Con una luz linealmente polarizada, que es una superposición de polarizaciones circulares izquierdas y derechas, se forma el llamado estado oscuro.

Para la desintonía cero de ambos campos, la población del nivel superior se hace cero, y la función de onda para niveles inferiores tiene diferencia de fase fija. El estado coherente se destruye con pequeñas desintonías de frecuencia inducidas por el campo magnético. A causa de esto, aparecen rasgos espectrales agudos. El campo magnético separa los subniveles Zeeman, esto produce diferencias en las velocidades de propagación para componentes polarizados del modo izquierdo y derecho, y el plano de polarización gira (rotación Faraday no lineal).

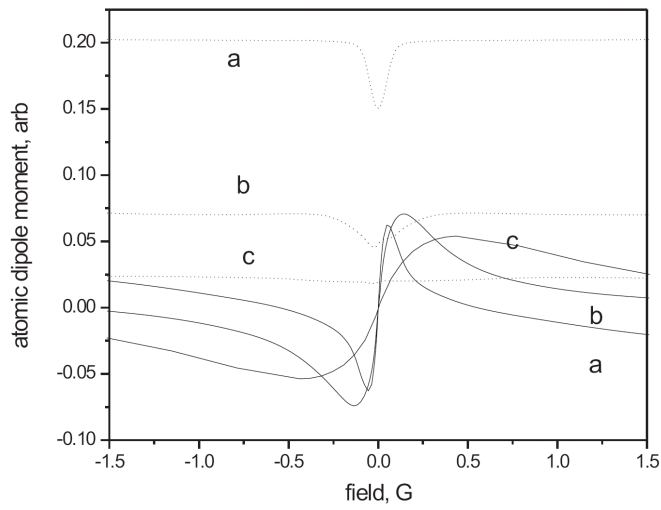
El mecanismo de rotación es ilustrado en la Grafica 3 para la transición $F_g = 1, F_e = 0$. El ángulo de rotación calculado como una función del campo magnético para diferentes intensidades de luz se presenta en la Grafica 4. El comportamiento es dominado aquí por dos lambda-sistemas formados en las transiciones $F_e = 0$ y $F_e = 1$. Para intensidades grandes, la interacción simultánea de la luz con ambos niveles $F_e = 0$ y $F_e = 1$ produce la disminución de la señal de rotación en comparación con la aproximación de los niveles independientes. La diferencia entre dos métodos de cálculo está alrededor de 1% para la intensidad $0.2mW/cm^2$, ~10% para la intensidad $2mW/cm^2$, y crece hasta un significativo 30% para $20mW/cm^2$.

El modelo de niveles independiente no nos da la caída experimentalmente observada en máximo posible ángulo de rotación para intensidades más altas; esto da, que el ángulo de rotación máximo es aproximadamente el mismo para 20 y $2mW/cm^2$.

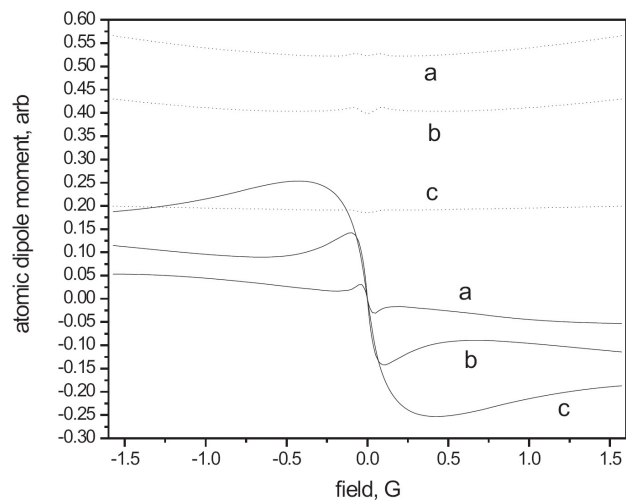


Grafica 3 Rotación de Faraday para $F_g = 1$, $F_e = 0$ transiciones. El ejemplo numérico demuestra que para el campo magnético diferente de cero los índices refractivos de la polarización circular izquierda (rociada) y derecha (rociada-punto) tienen diferentes dependencias de la desintonía de frecuencia de la transición. La diferencia (línea sólida) no desaparece si está integrada con respecto a la desintonía, así que este mecanismo es importante para la línea ensanchada Doppler. Intensidad de luz $2.13 mW / cm^2$, campo magnético $0.12 G$, radio del haz $l_0 = 1.19 mm$.

Para la línea $F_g = 2$, la transición más importante es a $F_e = 3$, que está separada de $F_g = 1$. El carácter de la rotación para la línea $F_g = 2$ es diferente, que para $F_g = 1$. El ángulo de rotación máximo crece aquí intensidad en todo el intervalo de intensidad investigado (la Grafica 5).



Grafica 4 Las partes reales e imaginarias del momento de dipolo calculado dividido por la amplitud del campo, que son proporcionales a la actividad óptica (sólida) y a la absorción (puntos) contra el campo magnético para las diversas intensidades del luz adentro de la línea $F_g = 1$. Las intensidades son: a) $0.216mW/cm^2$, b) $2.13mW/cm^2$, c) $19.2mW/cm^2$, el radio del haz es $l_0 = 1.19mm$.



Grafica 5 Lo mismo que en la Grafica 4, pero para la línea $F_g = 2$.

La rotación de polarización es básicamente el cambio del índice refractivo. A causa de la naturaleza del estado coherente, la absorción de átomo en este estado es reducida (transparencia inducida por la luz). Para el campo magnético nulo la rotación es el cero, pero para campos magnéticos pequeños y polarización casi lineal, se espera el apareamiento reforzado de la no linealidad de Kerr.

El crecimiento de la intensidad hace más grande la relación de la rotación a la absorción, que produce el holograma de fase más pronunciado. También es interesante observar la absorción para la polarización lineal como una función del campo magnético B . Aquí, el comportamiento característico también es diferente para las transiciones $F_g = 1$ y $F_g = 2$. Para $F_g = 1$, los efectos de coherencia producen un punto estrecho en la transmisión en un campo magnético cerca del cero. En $F_g = 2$, el punto es mucho más amplio, y tiene una estructura fina para un B pequeño.

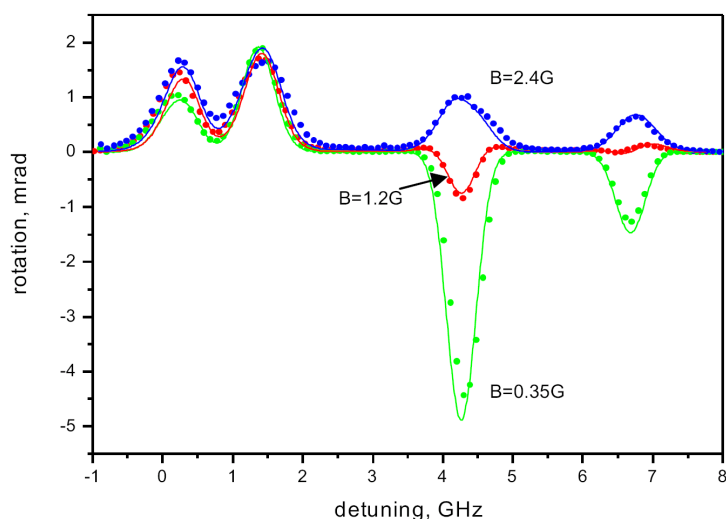
Como ya hemos mencionado, el método establecido de la descripción teórica es la ecuación maestra para la matriz de densidad atómica, pero para un número de subniveles grande los cálculos consumen mucho tiempo. Ya que el estado estable no es alcanzado para transiciones abiertas durante el tiempo de tránsito, para cálculos realistas es muy deseable tener en la cuenta la evolución temporal entera de parámetros atómicos.

En vez de solucionar para la evolución completa es posible introducir una repoblación eficaz para niveles inferiores y tomar un estado estacionario eficaz. Esto simplifica la solución, pero los parámetros de repoblación no se obtienen directamente, y tienen que ser fijados según el experimento. Nosotros usamos el método numérico directo, que produce la solución bastante rápida de la dinámica completa para la ecuación maestra para el átomo de rubidio multiniveles. Tal solución no contiene parámetros libres. El principio de cálculo es similar al algoritmo de división por paso (ver el capítulo 5) extensamente usado para modelar la propagación no lineal en medios con la no linealidad de Kerr, en particular en fibras ópticas.

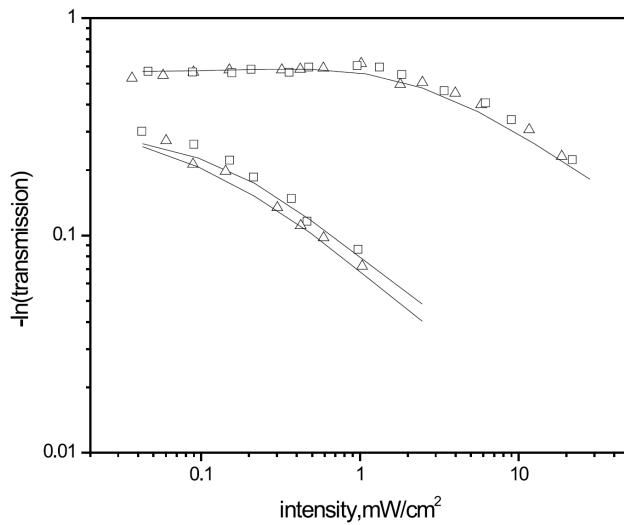
Tomamos la misma ecuación (1) y la solucionamos para los ambos isótopos de Rb usando el método de división por pasos, luego comparamos el resultado de la teoría con el experimento.

Los espectros calculados y su comparación con el experimento son presentados en la grafica 6. Se ve que, el cálculo da una descripción muy satisfactoria del complicado comportamiento del espectro para todas las líneas.

En otro experimento medimos la absorción para la luz polarizada circular como la función de la intensidad en el campo magnético nominalmente cero. Los resultados son presentados en la grafica 7. Es visto, que el modelo de cómputo da la descripción completamente exacta de la dependencia de absorción en la intensidad para ambas transiciones $F_g = 1$, y $F_g = 2$.

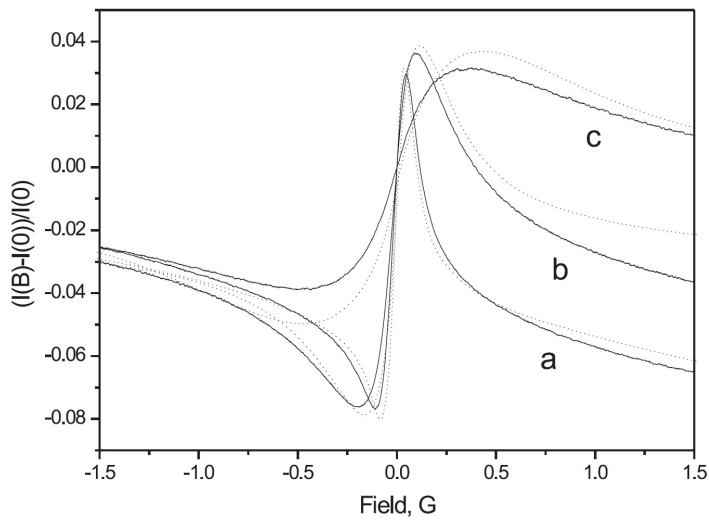


Grafica 6 La teoría (líneas) y experimento (puntos) para la intensidad de la luz $I = 1.1 \text{ mW/cm}^2$, diámetro del haz de 1 mm , temperatura 21° C , la densidad de vapor es común para todos los valores de campo magnético.

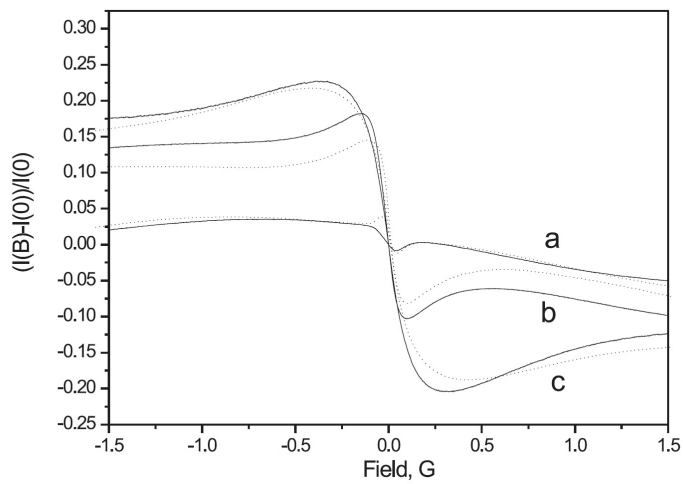


Grafica 7 Transmisión logarítmica utilizando la celda de 50mm con la temperatura $30^{\circ}C$ para el haz circularmente polarizado con el radio $l_0 = 1.19mm$ (triángulos) y $l_0 = 0.78mm$ (cuadrados). Curva superior - $F_g = 2$ línea, baja - $F_g = 1$. Las líneas solidas son teóricos para el radio correspondiente del haz (también vea Grafica 2). Para la transición $F_g = 2$, la teoría da curvas muy cercanas, y solamente se demuestra para radio $l_0 = 1.19mm$. Para los datos de la grafica utilizamos la densidad del vapor que está aproximadamente 10% más bajo, que el valor dado en la referencia [15].

Así, hemos comparado las curvas experimentales en las Graficas 8 y 9 con la combinación teóricamente calculada de absorción y rotación. Es visto, que la teoría da la descripción generalmente adecuada del complicado comportamiento de polarización, incluyendo buenas predicciones para magnitudes de rotación relativas en dos líneas diferentes. Los signos de la rotación para pequeños campos magnéticos en dos líneas son opuestos, como predice la teoría. También medimos la dependencia de absorción de la luz en el campo magnético para el haz linealmente polarizado. Estas curvas también encajan perfectamente con la teoría.



Grafica 8 Señal del fotodetector después de polarizador 45° como la función del campo magnético para la polarización lineal de la entrada y diversas intensidades de luz en línea $F_g = 1$ (sólido). Los valores de la intensidad y el radio del haz son iguales, como los usados para el cálculo en Grafica 4. Temperatura $30^\circ C$. Las líneas punteadas son curvas teóricas.



Grafica 9 Lo mismo que en la Grafica 8, pero para la línea $F_g = 2$.

Experimento, grabado de holograma.

En experimentos de mezcla de dos ondas el holograma dinámico a menudo se detecta cerrando el haz de señal y monitoreando la difracción de una onda de referencia en dirección de la señal. Para el rubidio, el tiempo de escritura/borrado puede ser menos que $100ns$; esto hace tal método bastante complicado técnicamente.

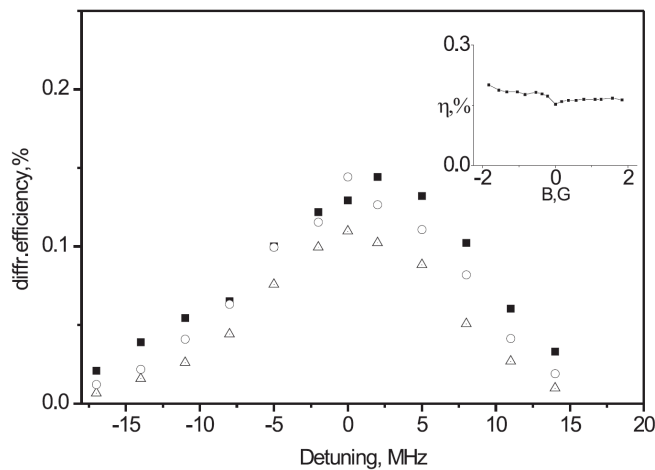
A causa de esto, para realizar mediciones cruzamos un haz de referencia fuerte y un haz de señal débil en un ángulo suficientemente pequeño para obtener un orden de difracción no-Bragg (conjugado), producido por la difracción de un haz fuerte en la rejilla escrita por él con un haz señal. La configuración básica aquí es una mezcla de tres ondas. El ángulo pequeño también ayuda a que los rayos se propagan con un buen traslape.

El experimento es representado en el grafico 6.5 (ver Capitulo 6). Para un grabado eficiente de holograma la temperatura tiene que ser bastante alta, y esto produce fuerte absorción. Elevando aún más la temperatura causa la disminución de la señal de difracción porque la absorción domina la intensidad de salida. Hay una temperatura de gravado óptima, que depende de parámetros del haz, y es diferente para las transiciones $F_g = 1$ y $F_g = 2$. El método más simple para la escritura de holograma en Rb es usar la polarización circular y la rejilla de amplitud en la línea $F_g = 2$. Esto puede hacerse en el campo magnético nulo, y la influencia de campo magnético no es significativa. Si la absorción total no es muy grande debido a la temperatura alta, la señal es máxima cerca del centro de la línea.

La eficiencia de difracción corresponde razonablemente a la estimación hecha con la conocida dependencia de la absorción en la intensidad del haz. La eficacia máxima obtenida para $T = 91^\circ C$ es $\sim 1\%$, consistente con valores característicos para hologramas de amplitud. En las gráficas 10 y 11 mostramos las dependencias de eficacia de difracción por la frecuencia de desintonía para dos intensidades del haz. Para la polarización circular e intensidad pequeña (la grafica

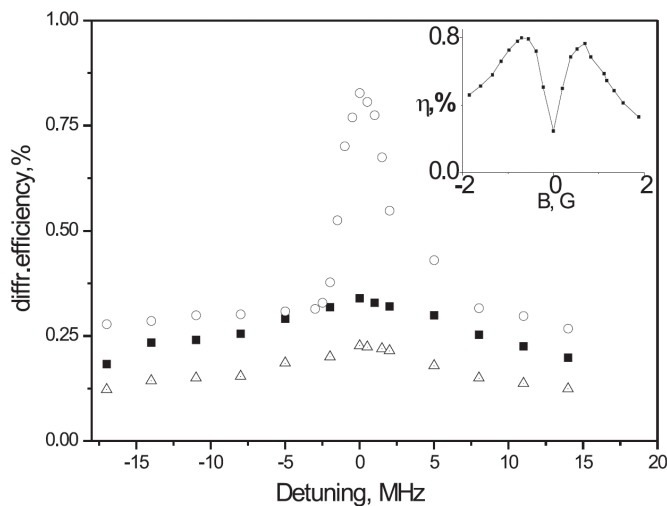
10), la frecuencia de límite $\nu = 8.5 \pm 0.5 \text{ MHz}$ (como es tomado por una caída de dos veces en la eficiencia de difracción) da el tiempo de grabado característico $\tau_R = (2\pi\nu)^{-1} \approx 20 \text{ nm}$. Este tiempo es comparable con la vida de nivel superior (25 ns), y se hace algo más pequeño para la intensidad más grande. Cuando el haz de señal es encendido y apagado, no se observan procesos transitorios en la difracción en los tiempos $> 100 \text{ ns}$, que podemos resolver directamente.

La eficacia de difracción η para la transición $F_g = 2$ puede ser mejorada usando la polarización lineal y un campo magnético débil. Las dependencias de η en el campo magnético con la desintonía cero son mostradas en los gráficos insertados.



Gráfica 10 La Eficacia de la difracción en el centro de línea $F_g = 2$ para la intensidad promedio del haz vs la desintonía entre haces de grabado; cuadros - polarización circular y campo magnético cero, triángulos - polarización plana y campo magnético cero, círculos - polarización plana y el campo magnético $B = 0.65 \text{ G}$ - la grafica insertada muestra la dependencia de intensidad de la difracción en el campo magnético para la polarización plana, $T = 91^\circ \text{ C}$.

Se ve, que para una intensidad pequeña, la aplicación de campo magnético no produce un cambio grande, pero para intensidades más altas la influencia es bien pronunciada. En el campo magnético, que da la señal máxima, aparece el punto alrededor de la desintonía cero, su anchura da el tiempo característico comparable al vuelo de tiempo a través de la franja (la Grafica 11).



Grafica 11. Como en la grafica 10, pero para la intensidad del haz $I = 67mW/cm^2$. La dependencia de la eficacia de difracción con desintonía para la polarización plana es tomada para $B = 0.6G$ que da el máximo en el campo de dependencia (grafica insertada).

Los experimentos que realizamos fueron hechos sobre todo para establecer la validez general de la teoría propuesta, así los errores sistemáticos podrían en algunos casos ser tan grandes como 10%. En particular, no usamos la capa anti-reflectante para la celda de rubidio, la no uniformidad en la iluminación a través de la abertura estaba alrededor 10%, y no medimos pequeñas absorciones en la transición $F_g = 1$ con buena precisión.

Para evitar recálculos de la densidad de vapor, realizamos todas las mediciones de absorción y rotación para la misma temperatura $30^{\circ}C$, y no podíamos satisfacer la condición de la pequeña absorción en todo el rango de intensidad. La teoría no toma en cuenta la interacción sistemática simultánea de la luz con niveles F adyacentes, y el ensanchamiento finito Doppler de la línea.

Para intensidades más grandes estos dos factores se hacen más importantes. En particular, la influencia de la auto-rotación resonante de la luz elípticamente polarizada no puede ser despreciada (no tratamos polarizaciones elípticas aquí).

Sin embargo, para intensidades moderadas prácticamente interesantes para la holografía, la teoría describe adecuadamente el comportamiento de absorción observada y rotación óptica, y puede ser usado como guía para la investigación experimental así como para la comparación con aproximaciones teóricas simplificadas.

Para la escritura holográfica en ^{87}Rb cerca de la resonancia es posible emplear rejillas de absorción para la línea $F_g = 2$. En este caso, aunque la eficiencia de difracción está limitada por $\sim 1\%$, la sensibilidad es alta, el tiempo de escritura puede ser tan corto como 20ns , y no hay ninguna necesidad de polarización estricta y control de campo magnético. La rejilla de absorción para la transición $F_g = 1$ es ineficaz, por las razones expuestas en la parte teórica.

Para obtener la rejilla más eficiente con el componente de fase en la longitud de onda de resonancia es necesario eliminar la absorción, así la intensidad de la luz crece. Aquí, el campo magnético y el control de polarización son esenciales. La transición $F_g = 1$ es fácilmente saturada, pero la mayor parte de la saturación viene de la transferencia "inútil" de población al nivel $F_g = 2$. Con temperaturas más altas, pueden grabarse las rejillas con la eficacia de difracción más grande, que aquellas para la rejilla de la amplitud en $F_g = 2$.

Generalmente, rejillas más eficientes requieren un tiempo de escritura más grande, y esto puede hacerse un problema para el espaciado de franja más pequeño, cuando el tiempo de vuelo a través de una franja disminuye.

La escritura holográfica CW con dos rayos de frecuencias casi iguales es experimentalmente más simple, pero parece probable, que las condiciones más favorables pueden ser obtenidas con la iluminación adicional en otra frecuencia, y/o usando mecanismos no estacionarios. La compleja estructura de niveles del rubidio proporciona muchas posibilidades a la manipulación.

Para concluir, demostramos que el formalismo de la matriz de la densidad, con el gran número de subniveles involucrados, da la adecuada descripción general de importantes procesos para la formación de la rejilla holográfica en el vapor de rubidio en intensidades moderadas. El análisis clarifica diferentes factores implicados, en particular el papel de tiempo de tránsito (diámetro del haz y espaciado de franja). Algunas situaciones, como la rejilla de absorción en $F_g = 2$ permite aproximaciones analíticas simples, pero parece que ningún modelo simple puede explicar el comportamiento de polarización complicado, que da la rejilla de fase eficiente para líneas fuertemente saturadas.

Resultados novedosos de tesis son:

- desarrollo del algoritmo de división por paso para el cálculo de la evolución de la matriz de densidad, y confirmación experimental de su eficacia para predecir el comportamiento no lineal de la rotación de Faraday en el vapor del rubidio cerca de la resonancia
- cálculos de absorción y refracción no lineales para algunos tipos de geometrías del grabado de la holograma, y su comparación con el experimento.

- aclaración de los mecanismos del grabado holográfico para las rejillas de la absorción
- Determinación experimental de las eficacias de difracción y de los tiempos del grabado para las rejillas de la amplitud y de la fase para los algunos casos particulares

Particularmente, fue demostrado que:

- Propuesto método de algoritmo de división por paso permite calcular los espectros observados no lineares con buena exactitud
- El grabado de holograma en el vapor de rubidio es rápida y eficiente, y puede ser utilizado para la adaptiva detección óptica de ultrasonido

